Theory of free-electron-laser heating and current drive in magnetized plasmas

Bruce I. Cohen, Ronald H. Cohen, William McCay Nevins, and Thomas D. Rognlien

Lawrence Livermore National Laboratory, University of California, Livermore, California 94551

The introduction of a powerful new microwave source, the free-electron laser, provides new opportunities for novel heating and current-drive schemes to be used in toroidal fusion devices. This high-power, pulsed source has a number of technical advantages for these applications, and its use is predicted to lead to improved current-drive efficiencies and opacities in reactor-grade fusion plasmas in specific cases. The Microwave Tokamak Experiment at the Lawrence Livermore National Laboratory will provide a test for some of these new heating and current-drive schemes. Although the motivation for much of this research has derived from the application of a free-electron laser to the heating of a tokamak plasma at a frequency near the electron cyclotron frequency, the underlying physics, i.e., the highly nonlinear interaction of an intense, pulsed, coherent electromagnetic wave with an electron in a magnetized plasma including relativistic effects, is of general interest. Other relevant applications include ionospheric modification by radio-frequency waves, high-energy electron accelerators, and the propagation of intense, pulsed electromagnetic waves in space and astrophysical plasmas. This review reports recent theoretical progress in the analysis and computer simulation of the absorption and current drive produced by intense pulses, and of the possible complications that may arise, e.g., parametric instabilities, nonlinear self-focusing, trapped-particle sideband instability, and instabilities of the heated plasma.

CONTENTS

I. INTRODUCTION

A. Motivation and scope

This theoretical review addresses the physics of intense microwave heating and current drive in toroidal magnetic confinement fusion devices. The important features of the physics reviewed here derive from the characteristics of a new technology, i.e., the free-electron laser, that is being brought to bear on heating and current drive in tokamaks. In addition to the application of a free-electron laser (FEL) to tokamak heating and current drive, the physics studies reported here are of significant fundamental interest and influence a number of other applications, including ionospheric modification experiments, high-energy electron accelerators, and the interaction of intense, coherent wave pulses in space and astrophysical plasmas. Because the wave-particle interactions of interest here are highly nonlinear, there is considerable novelty in the phenomena and opportunities arise for significantly improving the efficiency of driving current or plasma heating in a tokamak.

The application of principal interest in this review is provided by magnetic-confinement fusion in toroidal devices. The plasmas in toroidal fusion devices must be heated to bring them to thermonuclear temperatures. In addition, the good energy confinement and stability of tokamaks depend on a toroidal plasma current which provides both a twist of the magnetic field lines as they wrap around the torus and some magnetic self-pinching of the plasma. Figure 1 presents a schematic of a typical tokamak. As the plasma heats, Coulomb collisions between charged particles become less frequent (Spitzer, 1967). This renders Ohmic heating, wherein energy in magnetic windings surrounding the torus can be inductively coupled to the plasma and then dissipated in the plasma through Coulomb collisions (Chen, 1974; Wesson, 1987), much less effective at the high temperatures required in a thermonuclear plasma. Furthermore, Ohmic heating and current drive depend on the presence of a toroidal induction electric field, which in turn depends on an ever-increasing magnetic flux produced by the Ohmic coils as dictated by Faraday's law. Because the magnetic flux produced by the coils is necessarily limited, the pulse-length of an Ohmically driven tokamak is finite. Thus, the desire for steady-state tokamak operation pro-

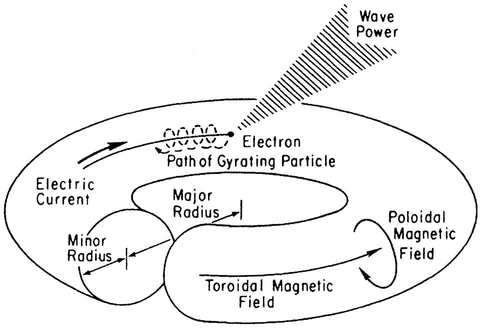

FIG. 1. Schematic of waves injected into a tokamak (Fisch, 1987). The tokamak has a toroidal magnetic field component encircling the torus hole and a poloidal component encircling the minor cross section.

vides additional motivation for noninductive heating and current-drive mechanisms (Fisch, 1987).

The emphasis of this review will be on recent progress in the theory of the interaction of an intense, pulsed, coherent electromagnetic wave with a plasma in an applied magnetic field at frequencies near the electron cyclotron frequency. Relativistic effects are shown to play a fundamental role here, and the wave-plasma interaction departs significantly from linear or quasilinear in nature. We shall review the basic underlying Hamiltonian theory of a charged particle in a strong wave field including relativistic effects, and present the conditions for trapping of an electron in the wave and for resonance overlap leading to stochastic electron motion. We present the results of calculations of the nonlinear opacity and current-drive efficiency as well. We shall also consider the nonlinear mixing of two strong waves to produce a third wave which heats and drives current in the plasma. We shall review some of the calculations addressing the stability of the intense coherent waves as well as the stability of the heated plasma. We shall also comment on current experiments that may test some of the theoretical issues presented here. The calculations reported here have been based on a combination of analytical theory, numerical integration of orbit equations, and particle simulations in which the particle orbits and Maxwell's equations are solved self-consistently. The review will be reasonably self-contained. However, for the sake of brevity, we shall refer to recent publications of closely related subject matter where it is appropriate.

B. Free-electron laser

Free-electron lasers offer the possibility of high-power, coherent radiation sources over a wide range of frequencies and with good efficiencies (Colson and Sessler, 1985; Roberson and Sprangle, 1989). An FEL relies on the following mechanism. A linear accelerator is used to produce a high-energy electron beam. The relativistic electron beam is propagated through a transverse periodic magnetic structure called a wiggler (see Fig. 2). The magnetic structure induces transverse oscillations of the electrons, which cause them to radiate. In the moving reference frame of the beam, the wiggler magnetic field Lorentz transforms into a backward propagating transverse electromagnetic wave with wave number and frequency given by

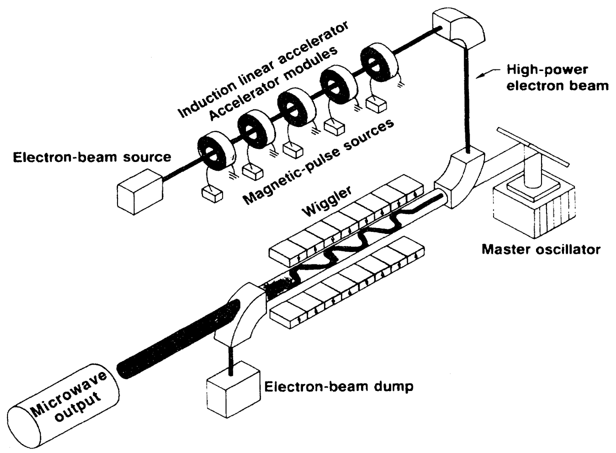

FIG. 2. Schematic of components for a high-power free-electron laser.

$$\begin{bmatrix} k_1 c \\ i\omega_1 \end{bmatrix} = \begin{bmatrix} \gamma & i\beta_z\gamma \\ -i\beta_z\gamma & \gamma \end{bmatrix} \begin{bmatrix} k_w c \\ 0 \end{bmatrix} = \begin{bmatrix} \gamma k_w c \\ -i\beta_z\gamma k_w c \end{bmatrix}, \tag{1.1}$$

where $\beta_z = v_b / c$ is the relative beam velocity, $\gamma = (1-\beta\cdot\beta)^{-1/2}$ is the relativistic mass factor, and $k_w = 2\pi/\lambda_w$ is the wiggler wave number.

The backscatter of the wiggler-produced transverse wave by an infinitesimal, longitudinal, periodic bunching of the electron beam with wave number $2k_1$ produces a forward-propagating, scattered transverse wave with wave number $-k_1$. The physical mechanism for the scattering is that the density perturbation of the electron beam couples with the transverse velocity perturbation of the beam in the wiggler field to produce a nonlinear current density that acts as an antenna for the scattered transverse wave. The transverse velocity and magnetic perturbations of the scattered wave then beat with the transverse magnetic and velocity perturbations, respectively, of the wiggler wave to produce a ponderomotive, longitudinally oriented Lorentz force to reinforce the bunching of the electron beam; and the scattering exponentiates (Kroll *et al.*, 1981). This scattering mechanism corresponds to stimulated Compton or Raman scattering (Drake *et al.*; 1974 Kroll *et al.*, 1981). The Raman limit pertains to situations wherein space-charge effects and the self-consistent longitudinal electric field are important in the bunching of the electron beam, i.e., the bunching satisfies the dispersion relation for an electron plasma oscillation. The exponentiation of the stimulated scattering depends nonlinearly on the wiggler field strength.

After Lorentz transforming the frequency–wave-number four-vector back to the laboratory reference frame, one obtains the wave number and frequency of the output radiation:

$$\begin{bmatrix} k_2c \\ i\omega_2 \end{bmatrix} = \begin{bmatrix} \gamma & -i\beta_z\gamma \\ i\beta_z\gamma & \gamma \end{bmatrix} \begin{bmatrix} -k_1 \\ i\omega_1 \end{bmatrix} \approx \begin{bmatrix} -2\gamma_z^2 k_w c \\ -i2\gamma_z^2 k_w c \end{bmatrix} \tag{1.2}$$

for $\gamma_z = (1-\beta_z^2)^{-1/2}$, $\beta_z \approx 1$, and an infinitesimal wiggler field strength. With the finite amplitude of the wiggler wave taken into account, the wavelength of the output radiation is expressed in terms of the total γ and given by (Kroll *et al.*, 1981)

$$\lambda_2 = \frac{\lambda_w}{2\gamma^2}(1+a_w^2) \, , \tag{1.3}$$

where $a_w = (eB_w/m_e c)/\sqrt{2}\, k_w c$ is a measure of the wiggler strength. From Eq. (1.3), we conclude that the frequency of the output radiation can be controlled by adjusting the wiggler wavelength or the electron beam energy. The dependence of λ_2 on a_w^2 has been exploited to improve the efficiency of the conversion of electron beam energy into coherent radiation. This is achieved by matching the decrease in γ as the electron beam slows down, due to its energy loss to radiation, with the appropriate decrease in a_w^2 to maintain the resonance condition given by Eq. (1.3). This is called tapering the wiggler.

High-power FEL operation and improved efficiency with tapering have been successfully demonstrated at the Lawrence Livermore National Laboratory using the Experimental Test Accelerator (ETA) to provide a 4.5 MeV, 10 kA electron beam and a wiggler with peak field of 3.7 kG (Orzechowski *et al.*, 1985, 1986). The taper of the wiggler was controlled by decreasing the current in the wiggler coils and resulted in improving the output power efficiency from 6% without taper to 35% with taper. In these experiments, the FEL was operated as a single-pass amplifier using a pulsed magnetron as the input master oscillator with radiation at the frequency $f = 34.6$ GHz and 100 kW of microwave power. Of the 100 kW injected, it was inferred that approximately 5 kW ended up in the TE_{10} mode that was exponentially amplified by the FEL. The peak output radiation with tapering approached 1 GW. Both the observed output power and the efficiency with and without tapering agreed well with computer simulations (Orzechowski *et al.*, 1986). The pulse length of the FEL was set by the electron accelerator, whose pulse length was 30 ns.

A key component in the FEL is the electron accelerator, because high-power operation demands high brightness and good emittance properties. The induction linac used at Livermore is well-suited for driving the FEL. The Livermore FEL has been upgraded for the Microwave Tokamak Experiment (MTX) to operate with a 7–10 MeV electron beam and produce radiation at 1 or 2 mm wavelength depending on whether the Intense Microwave Prototype (IMP) or Electron Laser Facility (ELF) wigglers are used (Thomassen, 1986). So far the MTX FEL has produced powers in excess of 200 MW in 8–10 ns pulses with an untapered wiggler and up to 400 MW with a preliminary attempt at tapering (Stallard *et al.*, 1990). The performance of the FEL was limited by energy variations in the electron beam. Preliminary experiments with a tapered wiggler resulted in substantially higher powers. The goal of MTX is to inject 8 GW in 30–50 ns pulses into the Alcator C tokamak, which was moved from the Massachusetts Institute of Technology to Livermore for this purpose (Thomassen, 1986). With a repetition rate of 5 kHz, reasonably high average powers (1.2–2 MW) will be injected (Jong *et al.*, 1989). The FEL output frequencies for the two wigglers, 140 GHz and 250 GHz, match the electron cyclotron frequency for 5 and 9 T toroidal magnetic fields on axis, respectively.

High-powered electron cyclotron heating (ECH) using a pulsed FEL as in the MTX has a number of technical advantages. Because of the pulsed nature of the FEL, breakdown problems in the waveguides are more easily avoided. The FEL is coupled quasi-optically with the tokamak using an overmoded waveguide with no dielectric window; the window is a fragile component in gyrotron systems. Furthermore, the FEL is a broadband amplifier and is tunable in frequency; and feedback control is possible. In general, ECH is compatible with small access ports, and its propagation into the plasma is well defined. Good penetration into the plasma and single-pass absorption can be achieved, and strong edge perturbations due to ECH are not expected. Finally, the high peak and average power of FEL-driven ECH affords unique opportunities to improve electron cyclotron heating and current-drive efficiencies, and to control MHD activity and disruptions by altering the current profile. These applications will be the focus of the rest of this review.

C. Basic physics

The main focus of this paper is the resonant interaction of electrons with a coherent electromagnetic wave in a strong magnetic field. In this section we present an elementary derivation of the relativistic cyclotron resonance condition. We also describe the types of electromagnetic waves that are considered here for ECH. We conclude with some general remarks about the influence of toroidal geometry on the electron orbits and ECH current drive.

The relativistic Newton-Lorentz equation is

$$\frac{d}{dt}\mathbf{p} = q\left[\mathbf{E} + \frac{\mathbf{v}\times\mathbf{B}}{c}\right] , \tag{1.4}$$

where $\mathbf{p} = \gamma m \mathbf{v}$ is the momentum, $\gamma = (1+p^2/m^2c^2)^{1/2}$,

m is the rest mass, q is the charge, $\mathbf{v}$ is the velocity, and $\mathbf{E}$ and $\mathbf{B}$ are the electric and magnetic fields. The particle position evolves according to

$$\frac{d\mathbf{x}}{dt}=\mathbf{v}\ . \tag{1.5}$$

In a uniform, time-independent magnetic field $\mathbf{B}=B_0\hat{\mathbf{z}}$ with no electric field, the charged particles execute cyclotron gyration at constant energy in the plane perpendicular to $\mathbf{B}$ with constant orbital frequency given by (if we neglect radiation by the particle, which is weak unless the particles are significantly relativistic)

$$\mathbf{\Omega}=\frac{q\mathbf{B}_0}{\gamma mc} \tag{1.6a}$$

and Larmor radius

$$\rho=\frac{v_\perp}{\Omega}\ . \tag{1.6b}$$

The particle energy can be expressed as

$$\gamma mc^2=\left[1+2\frac{p_\theta\Omega_0}{mc^2}+\frac{p_z^2}{m^2c^2}\right]^{1/2} mc^2\ , \tag{1.7}$$

where $p_\theta=p_\perp^2/2m\Omega_0$ is the relativistic magnetic moment or perpendicular action (in appropriate units), $\Omega_0=qB_0/mc$, and $p_\perp=\gamma mv_\perp$.

Consider the perturbations in the electron orbits produced by a plane wave with an electric field of infinitesimal amplitude

$$\mathbf{E}(x,t)=\tfrac{1}{2}\mathbf{E}\exp(-i\omega t+ik_zz+ik_\perp x)+\text{c.c.} \tag{1.8}$$

The electric field seen by the electron along its lowest-order, unperturbed orbit is obtained by substituting the expressions for the electron trajectory in the absence of the perturbing electric field, $z=z_0+v_z(t-t_0)$ and $x=X+\rho\sin(\Omega t+\theta_0)$, in Eq. (1.8), where z_0, t_0, and θ_0 are determined by the initial conditions and X is the guiding center position. After using the Bessel function identity,

$$\exp(iu\sin v)=\sum_{n=-\infty}^{\infty} J_n(u)\exp(inv)\ ,$$

Eq. (1.8) becomes

$$\mathbf{E}(\mathbf{x},t)=\frac{1}{2}\mathbf{E}'\sum_{n=-\infty}^{\infty} J_n(k_\perp\rho)\exp(-i\omega t+in\Omega +ik_zv_zt)+\text{c.c.}\ , \tag{1.9}$$

where nonessential, time-independent phase factors have been absorbed in $\mathbf{E}'$. An electron will experience a large acceleration due to this electric field if the time-dependent phase factor remains nearly constant along the zero-order orbit. The constancy of the phase factor defines the resonance condition, $\omega-n\Omega-k_zv_z=0$, which is given in terms of the momentum components by

$$\gamma-\frac{n\Omega_0}{\omega}-N_\parallel u_\parallel=0\ , \tag{1.10}$$

where $u_\parallel=p_\parallel/mc$, $u_\perp=p_\perp/mc$, $\gamma^2=1+u_\perp^2+u_\parallel^2$, and $N_\parallel=k_\parallel c/\omega$ is the parallel index of refraction. The parallel direction is along z. The resonance curves are ellipses in momenta space for $|N_\parallel|<1$ (Fig. 3).

A number of important insights can be gained directly from the inspection of the resonance condition Eq. (1.10) and Fig. 3. We see that the wave characteristics enter in an important way through the frequency and the parallel index of refraction. Because of the energy dependence entering through γ and the dependence on parallel momentum in the Doppler shift, an initially resonant electron can be nonlinearly detuned from resonance by exchanging energy and momentum with the wave so that γ and/or $u_\parallel$ are changed. Of course, the electron may be detuned from resonance by other means, for example, collisions. There is a special circumstance in which the electron can maintain resonance while it exchanges energy with the wave. This occurs for $N_\parallel\approx 1$. This condition is a generalization of the cyclotron auto-resonance-maser (CARM) condition $N=1$ for parallel-propagating waves (Davydovskii, 1962; Roberts and Buchsbaum, 1964; Kuo and Schmidt, 1985). Another interesting phenomenon that can be illustrated in Fig. 3 involves the competition of neighboring cyclotron resonances for electrons with comparable energies but oppositely directed momenta. Electrons of comparable energy lie on circles with nearly identical radii centered about the origin of momentum space. These circles can intersect the resonance curves of neighboring harmonics l and $l+1$ at locations where the values of $p_\parallel$ have opposite signs. This has been referred to as harmonic overlap (Smith *et al.*, 1987) and has important implications for ECH current drive. The two oppositely oriented groups of electrons that resonantly interact with the wave will contribute oppositely to the current driven parallel to the magnetic field, and a partial cancellation of the contributions to the current will occur.

Next we present an elementary view of electron cyclotron waves. Comprehensive treatments of this subject have been given in numerous textbooks and journal articles, e.g., Budden (1961), Stix (1962), Ott *et al.* (1980), Bornatici *et al.* (1983), and Batchelor *et al.* (1984). For purposes of this review, it will suffice to give a few simple results pertaining to the linear dispersion of the normal

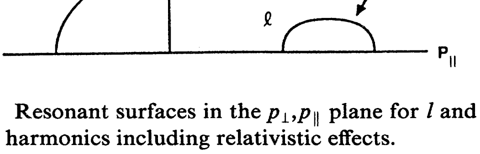

FIG. 3. Resonant surfaces in the $p_\perp,p_\parallel$ plane for l and $l+1$ cyclotron harmonics including relativistic effects.

modes. Relativistic effects are important for the resonant interaction with electrons and absorption, but are not generally important for propagation. Thus, we can consider the linear dispersion relation given by Stix (1962) for a general angle of propagation with respect to a straight, uniform magnetic field in a cold, homogeneous plasma,

$$\tan^2\theta=\frac{-P(N^2-R)(N^2-L)}{(SN^2-RL)(N^2-P)}\ , \tag{1.11}$$

where θ is the angle between the wave vector $\mathbf{k}$ and the applied magnetic field $\mathbf{B}_0$, $N^2=k^2c^2/\omega^2$, ω is the mode frequency,

$$P=1-\sum_s \omega_{ps}^2/\omega^2\ ,$$

$$R=1-\sum_s(\omega_{ps}^2/\omega^2)[\omega/(\omega+\Omega_s)]\ ,$$

$$L=1-\sum_s(\omega_{ps}^2/\omega^2)[\omega/(\omega-\Omega_s)]\ ,$$

$$\Omega_s=q_sB_0/m_sc\ , \quad \text{and} \quad S=(R+L)/2\ .$$

Electron cyclotron waves are elliptically polarized in general. For exactly parallel propagation with respect to $\mathbf{B}_0$, the normal modes are either right circularly polarized (R, rotates with the electrons) or left circularly polarized (L, rotates with the ions) and

$$N^2=\frac{k_\parallel^2c^2}{\omega^2}=R \text{ or } L\ , \quad \theta=0\ . \tag{1.12}$$

For waves propagating exactly perpendicular to the magnetic field, there are two linearly polarized normal modes: the ordinary (O) wave has its electric field parallel to $\mathbf{B}_0$ and

$$N^2=\frac{k_\perp^2c^2}{\omega^2}=P=1-\sum_s\frac{\omega_{ps}^2}{\omega^2}\ , \quad \theta=\pi/2\ , \tag{1.13}$$

while the extraordinary (X) mode has its electric field perpendicular to $\mathbf{B}_0$ and

$$N^2=\frac{k_\perp^2c^2}{\omega^2}=\frac{RL}{S}=\frac{(\omega^2-\omega_1^2)(\omega^2-\omega_2^2)}{\omega^2(\omega^2-\omega_{\rm uh}^2)}\ , \tag{1.14}$$

where $\omega_{1,2}=\frac{1}{2}\Omega_e[\mp 1+(1+4\omega_{pe}^2/\Omega_e^2)^{1/2}]$ and $\omega_{\rm uh}^2=\omega_{pe}^2+\Omega_e^2$.

The ordinary wave propagates for $\omega>\omega_{pe}$ and has a cutoff at $\omega=\omega_{pe}$. The extraordinary wave generally has a faster phase velocity, cuts off at $\omega=\omega_2$, becomes evanescent for $\omega<\omega_2$, and is resonant at the upper hybrid frequency $\omega=\omega_{\rm uh}$. As the wave vector tilts more in the direction of the background magnetic field, the O mode becomes left circularly polarized; and the X mode becomes right circularly polarized and maintains a faster phase velocity than the O mode. As a consequence of the cutoffs, the electron cyclotron resonance at the fundamental is accessible by O and X modes launched from the inside (i.e., the high-magnetic-field side) of the torus, while the resonance is only accessible from the outside (i.e., the low-magnetic-field side) using the O mode. The second harmonic resonance is accessible to both O and X modes launched from either the inside or outside of the torus.

Studies of the hot-plasma propagation and absorption of electron cyclotron waves have been presented by Ott *et al.* (1980), Bornatici *et al.* (1983), Batchelor *et al.* (1984), Timofeev (1989), and others cited in these papers. In general, finite-temperature effects force the cutoffs and resonances to occur at locations corresponding to higher values of the magnetic field for the same value of the wave frequency.

To complete this section on basic physics, we discuss a few simple properties of magnetic confinement in toroidal devices. A detailed presentation of tokamak physics is found in the excellent monograph by Wesson (1987). Because of the gyration of charged particles in a strong magnetic field, a magnetic field retards the expansion of plasma across the lines of force. However, streaming motion can occur along the field lines. By wrapping the field lines around a torus, a configuration of field lines that close on themselves can be established, which improves the confinement. However, in order to insure stability, the field lines must twist in the poloidal plane (the minor cross section) so that the field lines spend some of the time on the inside or high-field side of the magnetic axis. This renders a stabilizing force on the plasma when it tries to expand away from the torus into an increasing magnetic field on the inside of the device. Magnetohydrodynamic stability in both stellarators and tokamaks derives in part from the twist of the magnetic field.

As the particles follow the magnetic field around the torus, the magnetic field strength increases toward the inside of the torus because it is proportional to the inverse of the major radius. However, the spatial variation of the magnetic field is very weak on the scale of the Larmor radius; in consequence, the magnetic moment is an adiabatic invariant. The invariance of the magnetic moment, which is proportional to $p_\perp^2/B$, and energy conservation in the absence of collisions lead to a retarding force on a charged particle directed along the magnetic field line and opposite to the direction of increasing field strength. Particles with insufficient parallel kinetic energy are turned around, i.e., these particles are mirror-trapped on the outside of the torus, while particles with sufficient parallel kinetic energy can circulate all the way around the torus. The toroidal current carried by a trapped particle averages to zero over the orbital period, but a circulating particle can carry current. Thus, trapped particles can degrade the efficiency of a number of current-drive schemes and must be taken into account when devising strategies for efficient current drive (Fisch, 1987). The basic physics concepts of this section will be elaborated in the detailed calculations and applications in the subsequent sections.

D. Outline of succeeding sections

The plan of the rest of the paper is as follows. In Sec. II we present the relativistic Hamiltonian and a calculation of the particle dynamics including considerations of wave-particle trapping and stochasticity. A discussion of several nonlinear electron cyclotron heating and current-drive mechanisms is given in the second half of this section. The heating mechanisms considered are intense, pulsed ECH as envisioned in the MTX, including the effects of rising buckets, stochastic heating, and beat waves.

Current-drive applications with intense ECH are described in detail in Sec. III. The concept of pulsed current drive is reviewed first. The degradation in ECH current drive produced by magnetically trapped particles is briefly discussed next. The section is concluded with a comparison of current-drive efficiencies for various nonlinear mechanisms.

The stability of an intense electron cyclotron wave in a plasma is surveyed in Sec. IV. Intense electron cyclotron waves can nonlinearly couple to other waves in the plasma leading to parametric instabilities that compete as energy sinks with the intended heating or current-drive applications. We next review an instability in which the wave-trapped electrons induce the growth of sidebands of the incident wave. We also summarize the calculation of a virulent nonlinear self-focusing instability of an intense coherent O mode. We conclude the section with some remarks concerning the possible instability of a strongly heated plasma.

In Sec. V, we present the results of numerical simulations of intense, pulsed electron cyclotron heating and current drive. We begin the section with a brief discussion of the particle-orbit codes and the self-consistent particle simulations used to study the nonlinear phenomena. Numerical results are then reviewed that address nonlinear ECH, stochastic heating and current drive, rising buckets, beat-wave current drive, and parametric instability. In Sec. VI we present a discussion of two experiments that may provide tests of some of the theories reviewed here. Conclusions and comments on future research directions are given in Sec. VII.

II. WAVE-PARTICLE INTERACTION

A. Relativistic Hamiltonian and particle dynamics

There have been a number of analytical treatments of relativistic electron dynamics in a monochromatic electromagnetic wave in a strong magnetic field, for example, Kitsenko *et al.* (1975), Bolis and Spyrou (1986), Zvonkov and Timofeev (1986), Nevins *et al.* (1987), Zaslavskii *et al.* (1987), Villalon and Burke (1987), Davidson (1987), Davidson *et al.* (1989), Suvorov and Tokman (1988), Taylor *et al.* (1988), Menyuk *et al.* (1987 and 1988), Karimabadi and Angelopoulos (1989), Karimabadi *et al.* (1990), Cohen and Cohen (1988a, 1988b), Kotel'nikov and Stupakov (1990 and 1991), Farina and Pozzoli (1988), and references therein. In this section, we present a concise derivation of the nonlinear, relativistic electron dynamics following the presentation of Karimabadi *et al.* (1990). The nonlinear dynamics are deduced from a relativistic Hamiltonian which is expanded perturbatively in the applied wave amplitude. Fixed points and the oscillation frequencies of wave-trapped electrons are calculated for fundamental O and second-harmonic X modes. A wave-amplitude threshold for the onset of stochasticity is presented based on the condition for the overlap of neighboring cyclotron resonances.

The relativistic Hamiltonian for a plane wave of general polarization in a strong magnetic field expressed in terms of canonical variables is (Karimabadi *et al.*, 1990)

$$H=\sqrt{(c\mathbf{P}-q\,\mathbf{A})^2+m^2c^4}+q\Phi=\gamma mc^2+q\Phi\ , \tag{2.1}$$

where

$$\begin{aligned}\mathbf{A}&=\mathbf{A}_{em}+xB_0\hat{\mathbf{e}}_y\\ &=A_1\frac{k_\parallel}{k}\sin\psi\hat{\mathbf{e}}_x+A_2\cos\psi\hat{\mathbf{e}}_y-A_1\frac{k_\perp}{k}\sin\psi\hat{\mathbf{e}}_z+xB_0\hat{\mathbf{e}}_y\ ,\end{aligned} \tag{2.2a}$$

$$\Phi=\Phi_0\sin\psi\ ,\quad \psi=k_\perp x+k_\parallel z-\omega t\ , \tag{2.2b}$$

$\mathbf{P}$ is the canonical momentum, $\mathbf{A}$ is the vector potential, and Φ is the electrostatic potential. A canonical transformation is introduced to remove the explicit time dependence. The generating function is

$$S=P'_\theta\left[\theta-\frac{\omega t}{l}\right]\ , \tag{2.3a}$$

from which follows

$$P_\theta=P'_\theta=\frac{\partial S}{\partial\theta}\ ,\quad \theta'=\theta-\frac{\omega t}{l}=\frac{\partial S}{\partial P'_\theta}\ , \tag{2.3b}$$

and the transformed Hamiltonian is

$$H'=\gamma mc^2-\frac{\omega}{l}P_\theta+q\Phi_0\sin\psi=H+\frac{\partial S}{\partial t}\ . \tag{2.3c}$$

The Hamiltonian H' is now independent of time and a constant of the motion. We next expand the Hamiltonian to first order in the perturbing wave fields and evaluate the ψ phase factor at zero order using $x=X+\rho\cos\theta$, where X is the guiding center position and is a constant of the motion, and $\rho=P_\perp^{(0)}/m\Omega_0=(2P_\theta^{(0)}/m\Omega_0)^{1/2}$. After introducing the Bessel function expansion used in Sec. I and the identities $2J'_l(k_\perp\rho)=J_{l-1}(k_\perp\rho)-J_{l+1}(k_\perp\rho)$ and $J_l(-x)=(-1)^lJ_l(x)$, we obtain

$$H'=H_0+\varepsilon H_1\ ,\quad H_0=\gamma mc^2-\frac{\omega}{l}P_\theta\ ,$$

$$H_1=\sum_{n=-\infty}^{\infty}Z_n\sin[k_\parallel z+n\theta'-(1-n/l)\omega t]\ , \tag{2.4}$$

where

$$Z_n=\frac{mc^2}{\gamma_0}\left[\varepsilon_1\left(\frac{q}{|q|}\frac{p_\parallel}{mc}\sin\alpha-\frac{q}{|q|}\frac{\Omega}{k_\perp c}n\cos\alpha\right]J_n(k_\perp\rho)\right.$$
$$\left.+\varepsilon_2\frac{p_\perp}{mc}J_n'(k_\perp\rho)+\varepsilon_3\frac{q}{|q|}\gamma_0J_n(k_\perp\rho)\right]\ , \qquad (2.5)$$

where $k_\perp=k\sin\alpha$, $k_\parallel=k\cos\alpha$, $\varepsilon_{1,2}=|q|A_{1,2}/mc^2$ and $\varepsilon_3=|q|\Phi_0/mc^2$. The validity of the linear expansion of the Hamiltonian requires that $|\varepsilon_i|\ll 1$, and $|\mathbf{P}^{(1)}|\ll|\mathbf{P}^{(0)}|$ to justify the use of the zero-order Larmor radius in the argument of the Bessel functions and $dz^{(0)}/dt=p_\parallel^{(0)}/\gamma m$ in the phase factor.

The zero-order equations of motion are straightforwardly calculated from the H_0 in Eq. (2.4). Using $d\theta'/dt=\partial H_0/\partial P_\theta=\Omega-\omega/l$ and $dz/dt=v_z=p_z/\gamma m$ at zero order, we deduce that a particle can experience a large phase-synchronous acceleration from the perturbing wave fields if the phase of the lth term in H_1 is nearly time-independent, which recovers the relativistic cyclotron resonance condition given in Eq. (1.10).

The analysis of Karimabadi *et al.* (1990) addressed the structure of the resonances, the constant energy surfaces, the trapping widths and frequencies, the heating characteristics, and the condition for resonance overlap which leads to stochastic motion for the Hamiltonian of (2.4). Here we specialize the wave polarization to two cases of specific interest to tokamak heating, the O mode at $\omega\sim\Omega_e$ and the X mode at $\omega\sim 2\Omega_e$ perpendicularly incident from the outside of the torus, where there is easy port access and wave propagation into the magnetic axis is straightforward. For the O mode near perpendicular incidence, $A_1\approx A_z$, $A_2=\Phi_0=0$, $k_\perp\gg k_\parallel\sim 0$, and

$$H_1\sim\frac{mc^2}{\gamma}\frac{q\tilde{A}_1}{mc^2}\frac{p_z}{mc}J_1(k_\perp\rho)\sin(\theta-\omega t)\ . \qquad (2.6)$$

We further specialize to conditions for which the electron Larmor radius is small, which is valid for most circumstances of interest and allows the Bessel functions to be expanded for small argument. The fixed points are determined from Hamilton's equations

$$\frac{d}{dt}P_\theta=-\frac{\partial H}{\partial\theta'}=-\frac{p_z}{\sqrt{2}\gamma mc}\frac{k_\perp\tilde{A}_1}{B_0}\left[\frac{\Omega_0P_\theta}{mc^2}\right]^{1/2}mc^2\sin(\theta'+\pi/2)=0 \qquad (2.7a)$$

and

$$\frac{d\theta'}{dt}=\frac{\partial H}{\partial P_\theta}=\Omega_0\left[\frac{1}{\gamma}-\frac{\omega}{\Omega_0}-\frac{p_z}{2mc}\frac{k_\perp\tilde{A}_1}{B_0}\frac{(1+P_z^2/m^2c^2)}{\gamma^3}\left[\frac{mc^2}{2\Omega_0P_\theta}\right]^{1/2}\cos(\theta'+\pi/2)\right]=0\ . \qquad (2.7b)$$

If $(p_z/mc)(k_\perp\tilde{A}_1/B_0)(mc^2/\Omega_0P_\theta)^{1/2}\ll 1$, then the perturbation expansion remains valid; and the fixed points corresponding to $dP_\theta/dt=0$ and $d\theta'/dt=0$ satisfy both $\theta'=\pi/2+n\pi$ and the cyclotron resonance condition for small $k_\parallel v_z$, viz., $\omega=\Omega_0/\gamma$. Around an elliptic fixed point there is a set of closed nested orbits corresponding to wave-trapped trajectories. For small excursions from the elliptic fixed point, the Hamiltonian can be expanded to second order and put into the form of a simple-harmonic oscillator. The wave-trapped particle bounce frequency can then be readily calculated:

$$\omega_b^2=\left|\frac{\partial^2H}{\partial\theta'^2}\frac{\partial^2H}{\partial P_\theta^2}\right|=\Omega_0^2\left|\frac{p_z}{\gamma^4mc}\frac{k_0\tilde{A}_1}{B_0}\left[\frac{P_\theta\Omega_0}{2mc^2}\right]^{1/2}\right|\ . \qquad (2.8)$$

This specific result was obtained by expanding $J_1(k_\perp\rho)\approx k_\perp\rho/2$ and agrees with the results of Bolis and Spyrou (1986) and Nevins *et al.* (1987). Note that the trapping frequency scales as $|\tilde{A}_1|^{1/2}$.

The constant-energy surfaces and the fixed points have been examined in detail by Nevins *et al.* (1987), Kotel'nikov and Stupakov (1990), and Farina and Pozzoli (1988). The fixed-point values P_r of P_θ are determined by Eq. (2.7b). If we adopt units such that $m=c=|e|=1$, the fixed points for the O mode at perpendicular incidence can be obtained from the solution of

$$1-\frac{\gamma\omega}{\Omega_0}-\frac{\alpha^{(\mathrm{O})}}{2\gamma^2(P_\theta\Omega_0)^{1/2}}\cos\psi=0\ , \qquad (2.9)$$

where $\alpha^{(\mathrm{O})}\equiv(1/\sqrt{2})p_z(k_\perp\tilde{A}_1/B_0)(1+p_z^2)$, $\psi=n\pi$, and $\gamma^2=1+2P_\theta\Omega_0+p_z^2$. Figure 4 is taken from Kotel'nikov

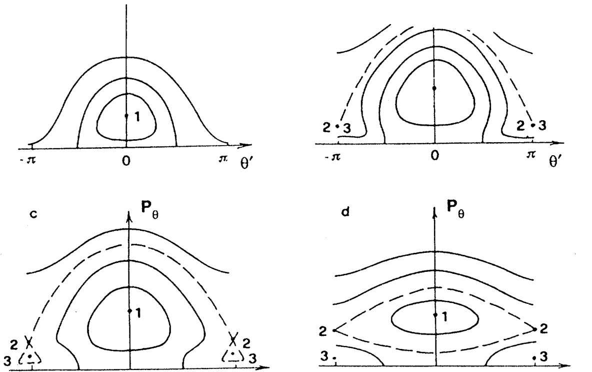

FIG. 4. Constant energy surfaces in the P_θ, θ' plane for ordinary mode heating at the fundamental cyclotron harmonic and different values of $\beta\equiv 1-\omega/\Omega_0$: (a) $\beta<\beta_c$, (b) $\beta=\beta_c$, (c) $\beta_c<\beta<2^{1/3}\beta_c$, and (d) $2^{1/3}\beta_c<\beta$, where $\beta_c\sim\alpha^{(0)2/3}$ (Kotel'nikov and Stupakov, 1989).

and Stupakov (1990) and illustrates the constant energy surfaces and the locations of the fixed points and the constant energy surfaces as functions of the parameters $\alpha^{(\mathrm{O})}$ and $\gamma_0^{-1}-\omega/\Omega_0$, where $\gamma_0^2=1+p_z^2$ and p_z is treated as a constant [this is only approximately true and has been quantified by Farina and Pozzoli (1991)]. For infinitesimal $\alpha^{(\mathrm{O})}$, the value of P_θ at the fixed points can be determined perturbatively by expanding in powers of $\alpha^{(\mathrm{O})}$. The zero-order solution is determined by $\omega=\Omega_0/\gamma$, which sets $P_\theta\Omega_0\approx P_r=1/\gamma_0-\omega/l\Omega_0$. For the weakly relativistic case, $\gamma\approx1+P_\theta\Omega_0+p_z^2/2$ in the second term of Eq. (2.9), and we can set $\gamma^2\rightarrow1$ in the third term if $\alpha^{(\mathrm{O})}$ is small. In this limit, $P_r=1/\gamma_0-\omega/l\Omega_0$ where $l=1$. At $\psi=\pi+2n\pi$ there is an elliptic fixed point labeled 1 in Fig. 4. For small $\alpha^{(\mathrm{O})}$, $\alpha^{(\mathrm{O})2/3}\ll|1-\gamma_0\omega/\Omega_0|$, there are another two fixed points at $\psi=0+2n\pi$, which are labeled 2 and 3 in Fig. 4. The X point lies above the O point. As the magnitude of $\alpha^{(\mathrm{O})}$ increases, the X and O points labeled 2 and 3 approach one another, merge, and disappear when $\alpha^{(\mathrm{O})2/3}>|1-\gamma_0\omega/\Omega_0|$. For small $\alpha^{(\mathrm{O})}$, the trapped-particle excursion amplitude δP_θ scales as $(\alpha^{(\mathrm{O})}P_r^{1/2})^{1/2}$ deduced from (2.7a) and a quadratic expansion of H_0, Eq. (2.4). The trapping frequency calculated in (2.8) scales as $\Omega_0\delta P_\theta$. We deduce from balancing the P_θ term in the Hamiltonian with the term proportional to $\alpha^{(\mathrm{O})}/P_\theta^{1/2}$, or by considering Eqs. (2.7a) and (2.8b), that the resonance oscillation scales as $\delta P_\theta\sim\alpha^{(\mathrm{O})2/3}$ and the trapping frequency scales as $\Omega_0\delta P_\theta$ when $\alpha^{(\mathrm{O})2/3}>|1-\gamma_0\omega/\Omega_0|$ in the strongly nonlinear regime. These results were obtained by Nevins *et al.* (1987) and Kotel'nikov and Stupakov (1990). The results for the weakly trapped limit agree with Kitsenko *et al.* (1975) and Bolis and Spyrou (1986), while the results in the strongly nonlinear limit agree with Kitsenko and Pankratov (1984) and Davidson (1987).

The calculation of fixed points, resonance oscillation amplitude, and trapping frequency for the X mode at $\omega\approx2\Omega_e$ and perpendicular incidence proceeds similarly. The X mode at second harmonic with $k_\parallel\approx0$ is dominantly electromagnetic with $A_1=0$, $A_2\gg\Phi_0$ and

$$H_1=\frac{mc^2}{\gamma}\frac{|qA_2|}{mc^2}\frac{P_\perp}{mc}\frac{J_1(k_\perp\rho)}{2}\sin(2\theta-\omega t)$$

$$\approx\frac{mc^2}{\gamma}\frac{k_\perp\tilde{A}_2}{B_0}\frac{|\Omega_0P_\theta|}{2mc^2}\sin(2\theta-\omega t) \qquad (2.10)$$

for $k_\perp\rho\ll1$. Equations for dP_θ/dt and $d\theta'/dt$ analogous to Eq. (2.7) are calculated directly, from which the fixed points are then determined. For small wave amplitudes, there is a fixed point near $P_\theta\Omega_0=P_r=1/\gamma_0-\omega/l\Omega_0$ where $l=2$ and we again have set $m=c=|e|=1$. In analogy to the solutions to Eq. (2.9), we consider the weakly relativistic limit to obtain $P_\theta\Omega_0=P_r\pm\alpha^{(\mathrm{X})}$, where $\alpha^{(\mathrm{X})}\equiv k_\perp\tilde{A}_2/2B_0$ and the upper sign corresponds to an X point at $\theta'+\pi/2=2n\pi$ (Fig. 5). For small values of $\alpha^{(\mathrm{X})}$, there are closed nested surfaces around the O point, and the trapping frequency deduced from a quadratic expansion in P_θ and θ' around the O point gives

$$\omega_b^2=\Omega_0^2\left|\frac{k_\perp\tilde{A}_2}{B_0}\frac{2\Omega_0P_\theta}{\gamma^4mc^2}\right|. \qquad (2.11)$$

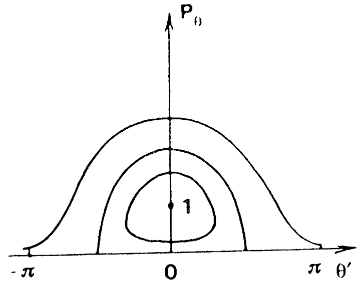

FIG. 5. Constant energy surfaces in the P_θ,θ' plane for extraordinary mode heating at the second harmonic.

The structure of the fixed points and the scaling of both the trapping frequency and the excursion of P_θ can be deduced easily from the Hamiltonian by expanding H_0 to second order in P_θ for $P_\theta\Omega_0/mc^2\ll1$ and balancing terms in H_0+H_1. When $|\alpha^{(\mathrm{X})}|\ll P_r$, the excursion δP_θ scales as $|\alpha^{(\mathrm{X})}P_r|^{1/2}$ and the trapping frequency scales as $\Omega_0\delta P_\theta$. As $\alpha^{(\mathrm{X})}$ grows, the trapping region swells and the X points migrate downward, finally reaching $P_\theta=0$ when $\alpha^{(\mathrm{X})}=P_\theta$. In this limit the trapping excursion scales as $\delta P_\theta\sim\alpha^{(\mathrm{X})}$, and the trapping frequency scales as $\Omega_0\delta P_\theta$.

The effective width of the separatrix can be further quantified by calculating the action enclosed; this allows a precise determination of the range of energies of incident electrons which become trapped. This has been carried out for $l=1$ by Kotelnikov and Stupakov (1991) and Farina and Pozzoli (1988), and for both $l=1$ and 2 by Farina and Pozzoli (1991). Cohen and Rognlien (1991) have shown that the action can be calculated in closed form through $l=6$. They further note that, for $l<4$, the separatrix energy width can be comparable to the resonant electron energy for $|E/B_0|\ll1$, so that the perturbation expansion of the Hamiltonian remains valid. For $l\geq4$, $|E/B_0|\gtrsim1$ is required, which invalidates the perturbation expansion of the Hamiltonian and makes other nonlinear effects like overlap of neighboring cyclotron-harmonic resonances important.

So far in this section we have calculated the resonant interaction of an electron with a single cyclotron harmonic. However, it is well known that neighboring cyclotron-harmonic components of a wave can interact with a charged particle leading to stochasticity when the trapping excursions in phase space overcome the separation between resonances (Chirikov, 1979). To calculate the stochasticity condition, the independent variables in the Hamiltonian are reduced by canonical transformation to a single pair of canonically conjugate coordinates (P_ψ,ψ). The separation δP_ψ between adjacent cyclotron harmonic resonances is determined by solving for the values of P_ψ for l and $l+1$ in the resonance condition Eq. (1.10). The trapping halfwidth ΔP_ψ for weak trapping is calculated by expanding H_0 expressed in terms of P_ψ and ψ to second order around an elliptic fixed point at $P_\psi = P_r$ and using

$$\Delta P_\psi = 2|\tilde{H}_1/(\partial^2 H_0/\partial P_\psi^2)|^{1/2} , \tag{2.12}$$

where $\tilde{H}_1$ is the amplitude of the interaction Hamiltonian. The trapped-particle bounce frequency from Eq. (2.8) is

$$\omega_b = \left| \frac{\partial^2 H_1}{\partial_\psi^2} \frac{\partial^2 H_0}{\partial P_\psi^2} \right|^{1/2} = \left| \tilde{H}_1 \frac{\partial^2 H_0}{\partial P_\psi^2} \right|^{1/2} . \tag{2.13}$$

Karimabadi *et al.* (1990) express Chirikov's stochasticity condition (Chirikov, 1979) as

$$\left| \frac{2\Delta P_\psi}{\delta P_\psi} \right| = \frac{4\omega_b}{\Omega_0/\gamma} \gtrsim 1 , \tag{2.14}$$

where γ is calculated at the O point and δP_ψ gives the separation between neighboring resonances. The explicit expressions for ω_b, ΔP_ψ, and δP_ψ, and the expressions relating P_ψ to P_θ and $P_\parallel$ depend on the wave polarization and the propagation characteristics. The results of Eq. (2.12) and (2.13) correspond to the weak trapping limit. The stochasticity condition will differ somewhat when the trapping around one resonance is strong, while the trapping around the neighboring resonance is weak.

The electron receives a succession of uncorrelated kicks from the wave and follows a diffusive path in phase space when the stochasticity condition is satisfied. The exceptions to this are in regions of phase in which the trajectories remain regular. We deduce from Hamilton's equations that the electron energy changes by $d\varepsilon = dt(dH/dt) = dt(\partial H_1/\partial t)$ and the parallel momentum changes by $dP_\parallel = dt(dP_\parallel/dt) = -dt(\partial H_1/\partial z)$ for an infinitesimal time dt. These increments define the heating characteristics with the sum over all cyclotron harmonics included in H_1,

$$\frac{d\varepsilon}{dP_\parallel} = \frac{\omega}{k_\parallel} = \frac{c}{N_\parallel} . \tag{2.15}$$

By comparison, the local value of the tangent to the resonance curve determined by (1.10) is given by $d\varepsilon/dP_\parallel = N_\parallel c$. Thus, for $N_\parallel$ very close to unity, the heating characteristic can align itself with the resonance curve (Fig. 6). This is the condition for cyclotron autoresonance. Furthermore, Karimabadi *et al.* (1990) show that the surfaces of constant H_0 are open for $N_\parallel \leq 1$: they are parabolic for $N_\parallel = 1$ and hyperbolic for $N_\parallel < 1$. Thus, while maintaining constancy of $H (H \approx H_0$ for $H_1 \ll H_0)$, the particle can be resonantly accelerated to very high kinetic energies for $N_\parallel \approx 1$.

The expression (2.15) is correct only in a uniform magnetic field; otherwise, $P_\parallel$ is not constant even in the absence of the wave. The expression is locally correct but not particularly useful if B_0 is constant but $k_\parallel$ varies. A modified description which allows such variations but includes only a single harmonic will be presented in the following [Eq. (2.34)]. For a single harmonic, the characteristics in a varying magnetic field are easily obtained from Hamilton's equations for the rate of change of ε and the canonical momentum P_θ: $\varepsilon = (\omega/l)P_\theta + \text{const.}$

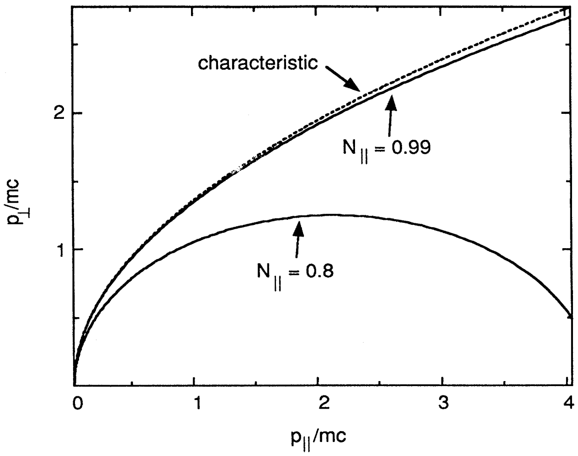

FIG. 6. Cyclotron resonance curves in momentum space for $l\Omega_0/\omega = 0.96$ and $N_\parallel = 0.8$ and 0.99 illustrating cyclotron autoresonance as $N_\parallel \to 1$. A heating characteristic is shown with a dashed curve.

The stochasticity accompanying the overlap of cyclotron resonances sets in at relatively higher wave amplitudes than for those required for the overlap of bounce resonances in a nonuniform magnetic field (Bernstein and Baxter, 1981; Rognlien, 1983a; Smith and Cohen, 1983; Hafizi and Aamodt, 1988). A quasilinear diffusion model has been found to adequately describe stochastic diffusion due to overlap of bounce resonances over much of the velocity space (Smith, Byers, and LoDestro, 1980; Cohen, Cohen, and Rognlien, 1983).

Another consequence of the wave-particle interaction that can be deduced directly from the Hamiltonian is the wave-driven cross-field transport of the heated electrons. For a single plane wave with $\mathbf{k} = k_\perp \hat{\mathbf{x}} + k_\parallel \hat{\mathbf{z}}$, it is easy to extend the analysis of Smith and Cohen (1983) and show that

$$\frac{\dot{H}}{\omega} = -\frac{qB_0}{k_\perp c} \dot{Y}$$

where $\dot{H}$ is the time derivative of the Hamiltonian and $\dot{Y}$ is the time derivative of the guiding-center position in y. Therefore, for a given kick in particle energy $\Delta\varepsilon$, there is a displacement in the guiding-center position given by

$$\Delta Y = -\frac{\Delta\varepsilon}{mc^2} \frac{c}{\Omega_0} N_\perp ,$$

where $N_\perp = k_\perp c/\omega$. Thus, significant heating will be accompanied by cross-field displacements that may be appreciable in units of c/Ω_0. However, it should be kept in mind that c/Ω_0 in a 5 T magnetic field is less than 0.04

cm, which is several orders of magnitude smaller than typical tokamak minor radii. Kupfer (1991) has used a similar analysis to deduce the radial diffusion coefficients accompanying quasilinear ECH.

The second half of this section illustrates the physics of wave trapping, stochasticity, and other nonlinearities in four mechanisms for heating and driving current in tokamaks.

B. Heating and current-drive mechanisms

Heating and current drive are closely linked in the four heating and current-drive mechanisms analyzed in this section. All four mechanisms depend on the cyclotron resonance condition (1.10). By introducing a wave having a finite $k_\parallel$ of definite sign, electrons transitting in a preferred toroidal direction will be heated and collide less often with other electrons and ions. This results in a net contribution to the toroidal current in addition to heating the plasma (Fisch, 1987).

The first heating and current-drive mechanism reviewed in this section is that introduced by Nevins *et al.* (1987) and is directly relevant to FEL heating in the MTX. Consider first, for simplicity, O-mode heating at normal incidence to the magnetic field and neglect any change in $N_\parallel$ or B_0 over the axial extent of the microwave beam. Because of the finite width of the wave envelope, electrons streaming along the magnetic field enter the edge of the wave and experience a wave amplitude that rises smoothly, peaks, and then decreases back to zero as the electrons exit the other side of the wave envelope. The following ordering of characteristic frequencies corresponds to high-power FEL operation in MTX (Nevins *et al.*, 1987; Thomassen, 1986).

$$\Omega_e \gg \omega_b \gg v_\parallel / w \gg \tau_{\rm FEL}^{-1} \gg v_\parallel / 2\pi R \gg \nu_e \gg T_{\rm FEL}^{-1} , \tag{2.16}$$

where Ω_e is the electron cyclotron frequency, ω_b is the trapping frequency of the resonant particles (which could be most of the illuminated electrons at the peak of the pulse and near $\omega = l\Omega_0$ in MTX), $v_\parallel$ is the parallel electron velocity, w is the width of the wave envelope along the magnetic field line, ν_e is the electron 90° collision frequency, R is the major radius of the tokamak, $\tau_{\rm FEL}$ is the FEL pulse length, and $T_{\rm FEL}$ is the time in between FEL pulses. Figure 7 shows a sequence of (P_θ, θ) phase space snapshots illustrating the evolution of principal separatrix and fixed points as experienced by the electrons transitting the pulse. The O point labeled 3 in Fig. 4 has been omitted in Fig. 7 in the interest of simplicity; its inclusion does not significantly alter the following arguments.

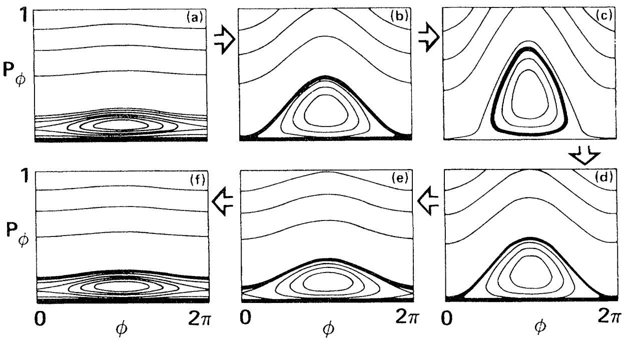

FIG. 7. (a)–(f) A sequence of snapshots of electron phase space moving across the microwave beam illustrating the heating mechanism in the strongly nonlinear regime (Nevins *et al.*, 1987). The thin lines are surfaces of constant H. The particles are indicated by the heavy lines. Particles are first pulled through the hyperbolic fixed point from below [(a)–(c)], and then half are expelled above the separatrix [(d)–(f)].

With the ordering of frequencies indicated in (2.16), the electron trajectories evolve adiabatically as the wave amplitude they see slowly changes; and the action is conserved except near the separatrices and the X points. Adiabaticity fails near the separatrices and the X points, because the trapping frequency ω_b decreases to zero so that $\omega_b \gg v_\parallel / w$ is no longer true ($v_\parallel / w$ is a measure of the characteristic rate of change of the wave amplitude seen by the electrons). After the electrons enter the FEL pulse and the wave amplitude swells, the X points and the lower separatrix migrate to smaller values of P_θ. Electrons are swept up by the growing wave and trapped. Their orbits take them around the O point on constant-energy surfaces with a relatively uniform distribution of phases. After the amplitude peaks and then decreases, the lower separatrix and X points rise; and the volume of phase space trapped by the wave within the separatrices shrinks. As the trapped particles get closer to the separatrices and to the X points, their action is no longer conserved because the trapping frequency decreases to zero. Electrons are detrapped as the wave amplitude further shrinks, and the volume of trapped particles decreases.

Nevins *et al.* (1987), Kotel'nikov and Stupakov (1990), and Cohen and Rognlien (1991) have calculated the rate of increase of untrapped phase-space volume above and below the trapped region as the decrease of the wave amplitude causes detrapping. For both the O mode at $\omega \approx \Omega_e$ and the X mode at $\omega \approx 2\Omega_e$, the phase-space volumes above and below the separatrix grow at the same rate, so that half of the resonant particles are expelled from the separatrix at significantly higher kinetic energies and heating results. To prove this, one expresses the Hamiltonian in action-angle variables, P_ψ and ψ, where P_ψ is the action and is adiabatically conserved as the wave amplitude slowly varies. The volume in phase space is given by

$$dA = dP_\psi d\psi = dP_\psi d\bar{H} / (\partial \bar{H} / \partial \psi) = -(dP_\psi / \dot{P}_\psi) d\bar{H} , \tag{2.17}$$

where $\bar{H} \equiv H - H_s$ is the value of the Hamiltonian relative to its value H_s at the separatrix, and where $\dot{P}_\psi$ is the total time derivative of P_ψ along the particle orbit. The time derivative of the area surrounding the separatrix is then

$$\dot{A}=-\int \frac{dP_\psi \dot{\bar{H}}}{\dot{P}_\psi} , \tag{2.18}$$

which is a sum of equal contributions from above and below the separatrix (Kotel'nikov and Stupakov, 1990). Here $\dot{\bar{H}}=\dot{\alpha}(\partial/\partial\alpha)(H-H_s)$, where α represents the wave amplitude. Thus, the finite spatial width of the electron cyclotron wave in the direction parallel to the magnetic field causes the detrapping and heating of the resonant electrons.

The nonlinear heating has been estimated analytically and evaluated numerically by Nevins *et al.* (1987), and quantified analytically by Kotel'nikov and Stupakov (1991), Pozzoli and Ronzio (1989), and Farina and Pozzoli (1991). Following Nevins *et al.* (1987), define an opacity $\tau_{\rm NL}=P_a/P_0$, where P_a is the absorbed power when wave attenuation is ignored, and P_0 is the incident power. The model will be applied to the O mode at $\omega\approx\Omega_e$ and the X mode at $\omega\approx 2\Omega_e$ that are normally incident on a plane stratified slab, and we allow gradients in B_0 only parallel to the wave propagation. There are several regimes of absorption depending on the values of the dimensionless parameters

$$p_1\equiv\Delta P(m_ec^2/T_e) , \quad p_2\equiv(m_ec^2/T_e)(2\pi/\omega\tau_c) , \tag{2.19}$$

where $\tau_c=w/v_\parallel$ is the transit time (which, for this simple case, is also the linear correlation time) and ΔP is the characteristic resonance excursion of P_θ in dimensionless units. It was deduced earlier that $\Delta P\sim\alpha^{1/(2-q)}$ in the limit of strong wave trapping, where $q=\frac{1}{2}$ for the O mode, $q=1$ for the X mode; and $\alpha^{(\rm O)}$ and $\alpha^{(\rm X)}$ were given after Eqs. (2.9) and (2.10). Thus, p_1 is the ratio of the nonlinear energy excursion to the thermal energy width; and p_2 is the ratio of the resonance width due to the finite correlation time to the thermal resonance width. In the first of two linear regimes, $p_1<p_2$ and $p_2<1$, a resonant electron acquires an amount of energy, $\Delta\varepsilon_L$, of order

$$\frac{\Delta\varepsilon_L}{T_e}\approx\frac{m_ec^2}{T_e}\dot{P}_\theta\tau_c\approx\alpha\Omega_0\tau_c(T_e/m_ec^2)^{q-1}\sim p_1^{2-q}/p_2 . \tag{2.20}$$

The relative resonance width $\Delta v_{\rm L}$ is calculated by equating the relativistic shift in the cyclotron resonance condition to the decorrelation frequency $2\pi/\tau_c$, from which one obtains $\Delta v_L\sim p_2v_e$. Thus, the fraction of resonant electrons is approximately p_2 for $p_2<1$. The relative deformation of the heated electron distribution function for electrons heated by $\Delta\varepsilon_{\rm L}$ is of order $\Delta\varepsilon_{\rm L}/T_e$ over the linear resonance width $\Delta v_{\rm L}$. Then the energy gain of the electrons averaged over the distribution function is

$$\langle\Delta\varepsilon_{\rm L}\rangle/T_e\approx p_2(\Delta\varepsilon_{\rm L}/T_e)^2\sim p_1^{4-2q}/p_2 . \tag{2.21}$$

The absorbed power P_a in this first linear regime is then

$$P_a^{\rm (L1)}\sim n_ev_eT_ehd_{\rm L}\frac{\langle\Delta\varepsilon_{\rm L}\rangle}{T_e}\sim n_ev_ehd_{\rm L1}\left[\frac{m_ec^2}{T_e}\right]^{4-2q}\frac{\alpha^2}{p_2} , \tag{2.22}$$

where h is the height of the ECH beam, $d_{\rm L1}\approx 4(T_e/m_ec^2)R$ is the width of the linear absorption layer due to thermal broadening of the cyclotron resonance, and R is the major radius of the tokamak, which is an adequate estimate of the magnetic scale length. The incident power is

$$P_0\approx Nchw(\tilde{E}^2/8\pi)\sim\alpha^2B_0^2chw(m_ec^2/T_e)^{2-2q}/N , \tag{2.23}$$

where $N=kc/\omega$ is the index of refraction. We define the opacity to be the ratio

$$\tau_{\rm L1}=\frac{P_a^{\rm (L1)}}{P_0}=A\frac{T_e}{m_ec^2}\frac{R}{\lambda_0}\frac{\omega_{pe}^2}{\Omega_e^2}N , \tag{2.24}$$

where A is a dimensionless constant that must be set equal to π^2 to match linear absorption theory (Nevins *et al.* (1987).

In the second linear regime, $p_1<p_2$ and $p_2>1$, the resonance width is now determined solely by the inverse of the correlation time τ_c^{-1} rather than by thermal effects. In consequence, there are two compensating changes in the estimate of the optical depth. With $p_2>1$, the entire electron distribution is resonant with the wave. Hence, $\Delta v_{\rm L}\sim p_2v_e$ in the first linear regime is replaced by v_e and

$$\langle\Delta\varepsilon_{\rm L2}\rangle/T_e\approx(\Delta\varepsilon_{\rm L}/T_e)^2\sim p_1^{4-2q}/p_2^2 . \tag{2.25}$$

The other change in the calculation of the opacity is that the width of the absorption layer is now set by the inverse correlation time rather than by thermal broadening of the cyclotron frequency, so that $d_{\rm L2}\approx R/\Omega_e\tau_c\approx p_2d_{\rm L1}$. These two changes cancel one another in determining the absorbed power, which is given by

$$P_a^{\rm (L2)}\sim n_ev_eT_ehd_{\rm L2}(m_ec^2/T_e)^{4-2q}\alpha^2/p_2^2\sim P_a^{\rm (L1)} \tag{2.26}$$

and the opacity is unchanged from (2.24),

$$\tau_{L2}=\frac{P_a^{\rm (L2)}}{P_0}=\tau_{\rm L1} . \tag{2.27}$$

For larger wave amplitudes so that $\omega_b\tau_c\geq 1$ for most of the resonant electrons, nonlinear effects limit the resonant energy excursion $\Delta\varepsilon$. The condition $\omega_b\tau_c\geq 1$ is equivalent to the linear step size $\Delta\varepsilon_L/T_e\sim p_1^{2-q}/p_2$ in (2.20), exceeding the relative linear resonance width in energy $\Delta v_{\rm L}/v_e\sim p_2$. Here ω_b is the bounce frequency for a weakly trapped electron. In this regime the step size for energy gain or loss is the island width $mv_e\Delta v\approx\Delta\varepsilon\approx m_ec^2\delta p$, where $\delta p\sim\alpha^{1/2}\sim p_1^{1-q/2}$. For $p_1<1$, not all of the electrons are trapped; the weakly trapped fraction scales as $\Delta\varepsilon/T_e\sim p_1^{1-q/2}$; and thermal effects determine the depth of the resonance layer. The trapping causes both heating and cooling of the resonant electrons, but there are more colder particles being heated than hotter particles that cool. The fraction of the trapped electrons that experiences net heating by an amount equal to the step size scales as an additional factor of $\Delta\varepsilon/T_e$. Thus, the energy gain averaged over the distribution function is

$$\langle \Delta\varepsilon_{\mathrm{NL1}} \rangle \approx T_e \left[\frac{\Delta\varepsilon}{T_e} \right]^3 \sim T_e p_1^{3-3q/2} \; . \tag{2.28}$$

Hence, the absorbed power is

$$P_a^{(\mathrm{NL1})} \approx n_e v_e T_e h d_{\mathrm{L1}} \left[\frac{\Delta\varepsilon}{T_e} \right]^3 \sim p_1^{3-3q/2} \; , \tag{2.29}$$

and the nonlinear opacity is

$$\tau_{\mathrm{NL1}} \equiv \frac{P_a^{(\mathrm{NL1})}}{P_0} \approx \frac{p_2}{p_1^{1-q/2}} \tau_{\mathrm{L}} \; . \tag{2.30}$$

In physical parameters,

$$\tau_{\mathrm{NL1}}^{(\mathrm{O})} \approx A(R/\lambda_0)(\omega_{pe}^2/\Omega_e^2) N (2\pi/\omega\tau_c) \times (T_e/m_e c^2)^{1/2} (B_0/k_\perp A_1)^{1/2}$$

and

$$\tau_{\mathrm{NL1}}^{(\mathrm{X})} \approx A(R/\lambda_0)(\omega_{pe}^2/\Omega_e^2) N (2\pi/\omega\tau_c) \times (T_e/m_e c^2)^{1/2} (2B_0/k_\perp A_2)^{1/2} \; .$$

The strongly nonlinear regime of absorption corresponds to even higher wave amplitudes $p_1 > \max(1, p_2)$. The width of the wave-trapped region in phase space is large, and essentially all of the electrons passing through the microwave beam become trapped. Half of the electrons gain energy $\Delta\varepsilon/T_e \sim p_1$ as they pass through the separatrix and X points on leaving the microwave pulse. Because $p_1 > p_2$ in this regime, nonlinear effects also determine the absorption depth, which is increased by a factor of p_1 relative to the linear absorption depth d_{L1}. Hence,

$$P_a^{(\mathrm{NL2})} \approx n_e v_e T_e h p_1 d_{\mathrm{L1}} (\Delta\varepsilon/T_e) \sim p_1^2 \; , \tag{2.31}$$

and the opacity is given by

$$\tau_{\mathrm{NL2}} \equiv \frac{P_a^{(\mathrm{NL2})}}{P_0} \approx \frac{p_2}{p_1^{2-2q}} \tau_L \; . \tag{2.32}$$

In physical parameters,

$$\tau_{\mathrm{NL2}}^{(\mathrm{O})} \approx A(R/\lambda_0)(2\pi/\omega\tau_c)(\omega_{pe}^2/\Omega_e^2) \times N (T_e/m_e c^2)^{2/3} (B_0/k_\perp A_1)^{2/3}$$

and

$$\tau_{\mathrm{NL2}}^{(\mathrm{X})} \approx A(R/\lambda_0)(2\pi/\omega\tau_c)(\omega_{pe}^2/\Omega_e^2) N \; .$$

Table I summarizes the four regimes of absorption as determined by the parameters p_1 and p_2. The dependence of the nonlinear opacities on wave amplitude enters through the parameter p_1. We observe that the opacity either remains unchanged or decreases as a function of increasing wave amplitude for O-mode heating at the first harmonic and X-mode heating at the second harmonic. The opacities join smoothly at each boundary between regimes except for the X mode at the boundary $p_1 = p_2 > 1$ between the second linear and second nonlinear regimes. This suggests that there is an additional absorption regime for the X mode that has been missed by these arguments.

TABLE I. ECH absorption regimes.

Regime	p_1	p_2	τ/τ_{L}
L1	$p_1 < p_2^{1/(1-q/2)}$	$p_2 < 1$	1
L2	$p_1 < p_2$	$p_2 > 1$	1
NL1	$p_1 < 1$	$p_2 < p_1$	$p_2/p_1^{1-q/2}$
NL2	$p_1 > (1, p_2)_{\max}$	$p_2 < p_1$	p_2/p_1^{2-2q}

We note that Kotel'nikov and Stupakov (1991) have obtained the same scaling for the O-mode opacity in the strongly nonlinear regime and have calculated the multiplicative constant $A \approx 1$ in the following manner. They deduced the energy gain of an electron transiting a large amplitude ordinary mode from the relativistic Hamiltonian analysis using Eq. (2.18) and their calculation of the 50% probability of being detrapped above or below the sepatrix on the exit from the wave. Their result for the absorbed energy is parametrized in terms of the parallel momentum of the electron p_z (whose change is assumed to be small) and the magnetic field location x relative to the cyclotron resonance. By assuming a Maxwellian distribution for p_z and a linear dependence of the magnetic profile on x near the resonance, they were then able to integrate the absorbed energy per electron over the electron distribution function and with respect to x to obtain the energy absorbed per unit time and per unit length in y. The ratio of the absorbed power to the incident power per unit length in y is the nonlinear opacity. The result has been further substantiated in the analytical and semianalytical calculations of Farina and Pozzoli (1991) and in earlier numerical orbit calculations by Nevins *et al.* (1987). Farina and Pozzoli (1991) included the effects of nonconstant p_z in their work. For the parameters proposed for high-power FEL experiments in MTX, $p_1 > 1$ and $p_2 < 1$, which puts the expected absorption into the second nonlinear regime. However, the heating in MTX is expected to be dominated by the rising-bucket mechanism reviewed later in this section. Current drive will accompany the nonlinear heating if the incident electron cyclotron waves have a $k_\parallel$ with a definite sign. Current drive and current-drive efficiency will be addressed later in the paper.

This picture can be substantially modified by variations in $N_\parallel$ or B over the axial extent of the microwave beam (Cohen and Rognlien, 1991; Cohen, Cohen, Nevins, *et al.* 1988, Cohen *et al.*, 1989). Variations in $N_\parallel$ or B cause the resonance to move in momentum space. If the variations are adiabatic, so that the time for the resonance to move a separatrix width exceeds the trapping time, then trapped electrons remain trapped as the resonance moves, and consequently can extract more energy from the microwave beam. The process is sometimes referred to as acceleration by a rising phase-space bucket. At the limit of marginal adiabaticity, it is analogous to acceleration in a synchrotron (Bethe and Rose, 1937; McMillan, 1945); and more generally, it is analogous to acceleration in a linear rf accelerator (Humphries, 1986). The process is the inverse of the deceleration of resonant electrons in a free-electron laser with a tapered wiggler (Colson and Sessler, 1985; Roberson and Sprangle, 1989).

Variations in B over the extent of the beam are typically very small in a tokamak, at most of order $(r/R)(w/2\pi Rq)$, where here q is the safety factor; the resultant change in energy $\Delta\gamma/\gamma \approx \Delta B/B$ is typically small. On the other hand, variations in $N_\parallel$ can appreciably increase the energy gain and, hence, the opacity. This is essentially true if one deliberately spreads the microwave beam with, for example, a cyclindrical mirror as shown in Fig. 8(a); but the modifications are important even for the variations in $N_\parallel$ which result from the combination of the natural divergence of the microwave beam as it emerges from the transmission system and curvature of the magnetic field lines. The effect is illustrated in Fig. 8. The parallel index of refraction increases from point (1) to point (2) in Fig. 8(a). The corresponding resonance curves are shown in Fig. 8(b). An electron initially resonant at (1) can be trapped and adiabatically lifted to a higher energy at (2) along a heating characteristic.

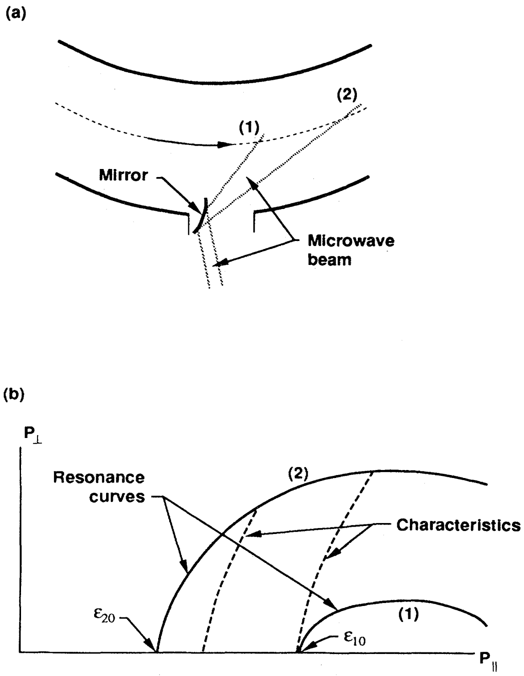

FIG. 8. Rising bucket concept (R. Cohen *et al.*, 1989). (a) Microwaves launched into a tokamak and reflected by a convex mirror to spread $k_\parallel$. (b) Resonance curves and heating characteristics in momentum space.

The heating characteristic here differs in a subtle way from that described by Eq. (2.15) derived for the stochastic regime, in which all cyclotron harmonics were included and it was assumed tacitly that $k_\parallel$ did not vary. Here, the heating characteristic is specific to a single harmonic number; and weak variations of the wave quantities and the applied magnetic field in z are allowed explicitly. The heating characteristic is derived from $d\varepsilon/dP_\theta = -(\partial H/\partial t)/(\partial H/\partial\theta) = \omega/l$, where H is given by Eqs. (2.4) and (2.5) with $k_\parallel z \rightarrow \int k_\parallel dz$; and the heating characteristic for the harmonic is given by (Hafizi and Aamodt, 1987; Rognlien, 1983b)

$$\varepsilon = \mu B_r + \text{const} , \tag{2.33}$$

where $B_r \equiv m_e c\omega/el$ [the l appearing here in the denominator of B_r was omitted by Cohen, Cohen, and Nevins, *et al.* (1988a) and Cohen *et al.* (1989)] and $\mu = eP_\theta/m_e c$ is the relativistic magnetic moment.

The energy gain for a typical situation in which magnetic gradients are insignificant across the beam is

$$\Delta\varepsilon = p_{\parallel i} c \left[-N_{\parallel i} + N_{\parallel f} \left[\frac{1-N_{\parallel i}^2}{1-N_{\parallel f}^2} \right]^{1/2} \right] , \tag{2.34}$$

where $N_{\parallel i}$ and $N_{\parallel f}$ are the initial and final parallel indices of refraction, and $p_{\parallel i}$ is the initial parallel momentum.

An important feature of Eq. (2.34) is that the energy gain becomes large and in fact diverges as $N_{\parallel f} \rightarrow 1$, which, as noted earlier, is the cyclotron autoresonance condition. This is particularly significant for current-drive applications, since current-drive efficiency increases with the energy of the accelerated electrons. Hence, we can devise "rising-bucket" current drive schemes which are optimized for diverging beams where the maximum-$N_\parallel$ ray is nearly tangent to the flux surfaces where the absorption is large.

The energy gained by individual electrons varies from that given by Eq. (2.34) by an amount of the order of the nonlinear resonance width, as electrons can be trapped from below resonance and detrapped above or vice versa. The absorption can be calculated (Cohen and Rognlien, 1991) from Eq. (2.34), the expressions for the nonlinear resonance width, the probabilities of trapping and detrapping above versus below resonance for fixed $N_\parallel$ and B ($\frac{1}{2}$ for either fundamental or second-harmonic heating), and energy conservation. The absorption coefficient is nonlocal: the absorption from a specific ray depends on the number and distribution of trapped electrons traversing the ray, which in turn depends on the intensity and $N_\parallel$ of all rays previously traversed. In a "sudden adiabatic" turn-on and turn-off approximation, in which an island is assumed to grow adiabatically at a fixed initial energy until all electrons destined to become trapped have been trapped, then accelerate without trapping or detrapping electrons, and then decay adiabatically at a fixed energy, the procedure outlined above yields closed-form expressions for the beam-averaged optical thickness.

The optical thickness τ is given by (Cohen and Rognlien, 1991):

$$\tau=\tau_{\mathrm{bl}}+\tau_{\mathrm{bw}} \tag{2.35}$$

where τ_{bl} and τ_{bw}, respectively, are contributions arising from the acceleration of the phase-space island ("bucket") and the finite width of the bucket. The bucket-width term is that derived earlier (τ_{NL1} or τ_{NL2}) for the absorption in the absence of gradients (with p_1 generalized as below), while τ_{bl} is given by

$$\tau_{\mathrm{bl}}=A_l\tau_{l0}p_3\hat{\psi}\delta\tilde{E}_e \tag{2.36}$$

where

$$A_l=\frac{Q_l^2N_\perp^{2l-3}p_2\Theta^{-1}}{\pi^{5/2}l^2p_1^{4-l}(1-N_\parallel^2)^2(l-1)!}\ ,$$

$$\hat{\psi}\equiv\frac{\psi+\psi^*}{\hat{\Delta}N+\hat{\Delta}^*N}\ ,$$

and

$$\tau_{l0}\equiv\pi^2\Theta^l\frac{l^{2l-2}}{2^{l-1}(l-1)!}\frac{\omega_{pe}^2}{\Omega_{ce}^2}\frac{\hat{R}}{\lambda}$$

with ω_{pe} and Ω_{ce} the electron plasma and cyclotron frequencies, and

$$\delta\tilde{E}_e=\delta E_e/T=\min(1,(8/\pi)p_0^{1/2}\Theta^{-1+l/4})\ .$$

Other quantities appearing in these expressions are: l=harmonic number, $Q_l=(2^{1/2}E_-+N_\perp\gamma E_\parallel v_\parallel/c)/E_k$ is the polarization factor; E_k and E_- are the amplitudes of the electric field and its left-hand circularly polarized component; $\Theta=T/mc^2$, $p_0\equiv\alpha\gamma/(1-N_\parallel^2)$, $p_1\equiv p_0^{1/(2-q)}/\Theta$ (a generalization of the previously given definition to oblique propagation), $\alpha\equiv2^{-l/2}(E_kQ_l/\gamma B)l^{l-2}N_\perp^{l-1}/(l-1)!$, $p_3\equiv(\hat{\Delta}N+\hat{\Delta}^*N)/(2\Theta)^{1/2}$,

$$\hat{\Delta}N=\left[-N_{\parallel1}+N_{\parallel2}\left[\frac{1-N_{\parallel1}^2}{1-N_{\parallel2}^2}\right]^{1/2}\right](1-N_{\parallel1}^2)\ ,$$

$\hat{\Delta}^*N(N_{\parallel1},N_{\parallel2})=\hat{\Delta}N(-N_{\parallel2},-N_{\parallel1})$ (and similarly for ψ), $\hat{R}=R_0/\cos\phi$, R_0 is the major radius at the cyclotron resonance, ϕ is the angle of the poloidal projection of the central microwave ray with the major-radius direction, $\psi=\min(\psi_b,\psi_s+\psi_b\delta E/2T)$,

$$\psi_b=\hat{\Delta}N\pi^{1/2}\delta E/(4T)+\Psi\ ,$$

$$\psi_s=\frac{3}{4}\frac{\pi^{1/2}}{\theta}\left[\frac{N_{\parallel2}^2}{1-N_{\parallel2}^2}\left[\Delta N-\frac{N_{\parallel2}^3-N_{\parallel1}^3}{3}\right]+\frac{\Delta N}{3}-\frac{2}{3}\frac{N_{\parallel2}(1-N_{\parallel1}^2)^{3/2}}{(1-N_{\parallel2}^2)^{1/2}}\right]+(2\Theta)^{-1/2}\frac{(\hat{\Delta}N)^2}{(1-N_{\parallel1}^2)}\ ,$$

$$\Psi\equiv\Psi(N_{\parallel1},N_{\parallel2})=(2\Theta)^{-1/2}\left[N_{\parallel1}^2-N_{\parallel1}N_{\parallel2}\left[\frac{1-N_{\parallel1}^2}{1-N_{\parallel2}^2}\right]^{1/2}-\frac{N_{\parallel2}(\arcsin N_{\parallel1}-\arcsin N_{\parallel2})}{(1-N_{\parallel2}^2)^{1/2}}\right]\ ,$$

$$\delta E/T=\max(\eta_bp_1,(8/\pi)\Theta^{-1+l/4}p_0^{1/2})\ ,$$

and $\eta_b=2(27/16)^{1/3}\approx2.38$ for fundamental heating, while $\eta_b=2$ for second harmonic. These expressions apply for fundamental or second-harmonic heating (extraordinary and ordinary modes) of a Maxwellian electron distribution, with diverging beams [$N_\parallel\mathrm{sgn}(v_\parallel)$ increases as electrons cross the beam], and assume that the variation of $N_\parallel$ over the extent of the microwave beam dominates over the change in B_0. Generalizations to other harmonics, non-Maxwellian plasmas, and converging beams can be found in Cohen and Rognlien (1991).

An important qualitative feature of Eq. (2.36) is that the optical thickness increases with the spread of $N_\parallel$ and can even exceed the linear value for rather moderate spreads (includes those which can arise from the combination of toroidal curvature and natural beam divergence). This will be explicitly demonstrated in Sec. V. The derivation of Eq. (2.36) assumes that the buckets are lifted adiabatically. When this is not the case, the absorption becomes linear. An interpolation formula describing partially adiabatic bucket lift is given by Cohen and Rognlien (1991).

An implicit assumption in the preceding discussion of nonlinear absorption was that the trapping regions of phase space centered on neighboring cyclotron resonances did not overlap. However, as the wave amplitude increases the trapping regions swell; and with sufficiently large wave amplitude there is overlap of the neighboring trapping regions (Menyuk *et al.*, 1987, 1988; Karimabadi *et al.*, 1990). The principal cyclotron resonance, the neighboring interacting resonances, and the heating characteristics are all determined by the same values of wave frequency and $k_\parallel$. Thus, electrons with a preferred sign of $v_\parallel$ can be stochastically accelerated leading to current drive in addition to heating.

Stochastic electron diffusion along heating characteristics occurs when resonances overlap. When the principal cyclotron harmonic number is relatively low, the separation of the neighboring resonances in $p_\perp$ and $p_\parallel$ is substantial. As a result, just preceding the onset of resonance overlap, the trapping around the principal resonance will be described typically by the strong trapping physics presented earlier in this section. The closest neighboring resonance in momentum space will correspond to the next higher cyclotron harmonic number in most circumstances, and the energy of the resonant particles will be significantly higher than those in the principal resonance (see Fig. 3 and Figs. 1 and 2 of Meynuk *et al.*, 1988). In consequence of the larger value of γ, the island width of the neighboring resonance will have a smaller amplitude. The width of the neighboring resonance need not be very large to induce stochasticity because the primary resonance width is already large. Thus, the trapping around the neighboring resonance is typically in the weak regime while the trapping around the primary resonance is strong (Lichtenberg and Lieberman, 1983). The appropriate overlap condition is not given by (2.14) for this case, and the correct analytical expression for intense ECH has not appeared in the literature as yet. However, numerical determination of the stochasticity thresholds has been made by Rognlien and Nevins (1987) based on explicit orbit integrations (see Sec. V).

Figure 9 displays the values of the right-hand circularly polarized electric field component E_{cr}/B_0 for the extraordinary mode and in circumstances representative of MTX operation as calculated by Rognlien and Nevins (1987). Here, $N_{\parallel}=0$ and $N_{\perp}=1$; and infinitely wide plane waves were considered. The orbit integrations demonstrate that for $k_{\perp}\rho \ll 1$ initially, the right circularly polarized component is dominant over the response to the left circular component. The threshold amplitudes shown for the X mode are systematically lower than for the O-mode case (the O-mode threshold amplitudes satisfy $E_{\parallel}/B_0 \geq 0.3$ with the minimum value at perpendicular incidence occurring near $\omega/\Omega_0=0.9$) and significantly exceed the electric field strengths expected in MTX, $E/B_0 \lesssim 0.02$, unless substantial focusing is introduced or occurs nonlinearly. The stochasticity threshold can be lowered by introducing a second FEL at a different frequency. For the case of right circularly polarized X modes with frequencies $\omega/\Omega_e=1.7$ and 1.96 at normal incidence, numerical orbit integrations determined that the total power at the threshold for stochasticity was reduced by $\sim\frac{1}{2}$ over the single-wave case (Rognlien and Nevins, 1987).

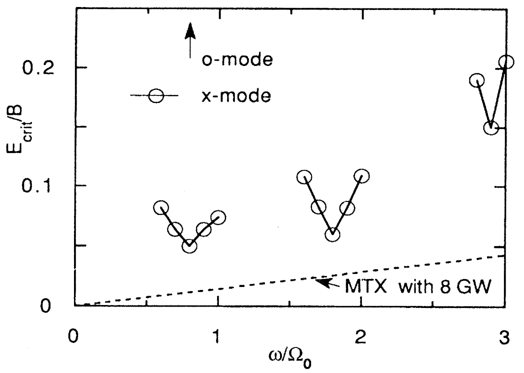

FIG. 9. Stochasticity threshold values of the normalized right-hand component of the electric field E_{crit}/B_0 for the extraordinary mode for different values ω/Ω_0 at perpendicular incidence. For this low-density example, the total electric field is $E_0=\sqrt{2}E_{\mathrm{crit}}$. For the O-mode case, the threshold is $E_{\parallel}/B_0\sim 0.3$ as indicated.

Because of the significant amplitudes required to achieve stochasticity, a matter of particular concern for the application of stochastic heating and current drive is the possibility of parametric instability (Porkolab and Cohen, 1988), which will be addressed in Sec. IV. The question of parametric instability is closely related to whether ponderomotive effects are important. The ponderomotive force is important compared to the thermal pressure in influencing force balance in the plasma when

$$\frac{E^2}{B_0^2} \gtrsim \frac{T_e}{m_e c^2} \ . \tag{2.37}$$

Operation at high power in MTX with $T_e=1-2$ keV in the core plasma is expected to satisfy $E^2/B_0^2 \ll T_e/m_e c$. Only at the edge of the plasma where the temperature falls is the ponderomotive force likely to be appreciable. However, if the stochastic regime could be achieved in MTX, (2.37) would be satisfied before the plasma substantially heated; and ponderomotive effects and self-focusing could be important. Consideration of ponderomotive self-focusing is presented in Sec. IV.

Electron dynamics in the stochastic regime have been studied by numerically integrating the orbits in the work of Menyuk *et al.* (1987, 1988), Rognlien and Nevins (1987), Hizanidis *et al.* (1989), and Karimabadi (1990), and analytically by Hizanidis (1989). Hizanidis (1989) derived a Fokker-Planck model of the electron diffusion appropriate for an infinite plane wave with amplitude well above the threshold for stochasticity. Near the threshold, not all of the momentum phase plane is stochastic: some islands of regular motion remain. For higher wave amplitudes the stochasticity is more complete [for example, see Figs. 3 and 4 of Hizanidis *et al.* (1989)]. The numerical results of Hizanidis *et al.* (1989) demonstrate that as a function of increasing angle of propagation with respect to the magnetic field, the trapping widths for a right circularly polarized monochromatic wave increase; and the resonances are more closely spaced in momentum space so that the threshold for stochasticity decreases. The numerical results also exhibit a relatively short initial transient after which the mean-square deviations of various moments of the electron distribution grow linearly in time in fairly good agreement with theory. The dependence of the diffusion coefficient on wave amplitude predicted by theory and calculated numerically is approximately quadratic. However, later in time the stochastic motion is not described very well by Fokker-Planck theory. In the stochastic regime, nearly all of the electrons passing through the microwave pulse will be strongly heated and the plasma becomes strongly absorbing. For MTX applications, in the stochastic regime electron energies grow by order of their rest-mass energy; and large opacities result (Rognlien and Nevins, 1987).

The fourth heating and current-drive mechanism is beat-wave current drive. In beat-wave current drive, two intense, high-frequency transverse waves nonlinearly mix to resonantly excite a low-frequency longitudinal wave that imparts energy and momentum to the plasma as it damps. This application of beat-wave excitation to current drive in a magnetized plasma was suggested by R. M. O. Galvão and T. Tajima in 1983 in unpublished work. At about the same time, Cohen independently calculated the nonlinear coupling of transverse waves to a Langmuir wave and determined the resulting current-drive efficiency when the Langmuir wave was Landau damped by passing electrons (Cohen, 1984). Since then there have been additional one- and two-dimensional calculations and simulations by Tajima (1985), Mendonca and Galvão (1986), Mendonca (1986), Cohen, Cohen, Logan, *et al.* (1988), Heikkinen *et al.* (1989), Amin and Cairns (1990), and references therein. Recently there has been an experimental demonstration of beat-wave coupling in a toroidal plasma, the Davis Diverted Tokamak at Lawrence Livermore National Laboratory; and the experiment will attempt to observe a driven current (Rogers *et al.*, 1989).

Beat-wave excitation is an example of a resonant three-wave interaction. The frequency and wave-number matching conditions required to ensure a strong, phase-coherent interaction are $\omega_1-\omega_2=\omega_3$, $\mathbf{k}_1-\mathbf{k}_2=\mathbf{k}_3$.

There are a number of requirements to be met for the achievement of high efficiency in beat-wave heating and current drive (Cohen, Cohen, Logan, *et al.* (1988). The difference frequency of the two microwave pump beams must match the local electron plasma frequency to excite a large-amplitude plasma wave. It is advantageous to excite the beat wave and damp it on resonant electrons on or inside the magnetic axis to minimize the degradation of the current drive due to magnetically trapped electrons [the same consideration is true for the other rf current-drive schemes (Fisch, 1987)]. Furthermore, the beat-wave phase velocity parallel to $\mathbf{B}_0$ must fall in an appropriate velocity range so that there are sufficient numbers of electrons to damp the Langmuir wave and carry all the current. The two transverse waves should be similarly polarized to permit nonlinear coupling. Finally, the wave momentum and energy deposited in the plasma depend nonlinearly on the product of the two microwave beam powers.

The physical mechanism at work in beat-wave excitation is as follows. The electron equation of motion is influenced by quadratically nonlinear driving forces, e.g., the Lorentz force and the electric field force at the linearly displaced particle position. The contributions to these forces coming from the low-frequency beat produced by the bilinear mixing of orbit perturbations and fields from the two high-frequency transverse waves ($\omega \geq \Omega_e$) constitute the ponderomotive forces at the low frequency and can produce an acceleration that resonantly excites a longitudinal wave. The nonlinear beat of the electron density perturbation with the high-frequency velocity perturbations produces high-frequency current-density perturbations that drive changes to the microwave beams in the mixing region. This process is an example of stimulated Raman scattering.

The nonlinear beat-wave equations have been presented in several papers. Here we use the formalism of Cohen, Cohen, Logan *et al.* (1988) for parallel and antiparallel beat-wave coupling. Amin and Cairns (1990) have generalized this formulation to two dimensions. The nonlinear wave equation that describes the conservation of wave action flux at steady state and from which the efficiency of beat-wave current drive can be deduced is

$$\hat{k}_1\cdot\nabla J_1=\frac{-2\pi k_3^2}{k_1k_2}J_1J_2\,\mathrm{Im}[\chi_e(1+\chi_i)/\varepsilon]=-\hat{k}_2\cdot\nabla J_2 \tag{2.38}$$

for parallel or antiparallel orientations of the pump waves with identical polarization, where $J_{1,2}=(k_{1,2}/2\pi)|u_{1,2}/c|^2$ are the transverse-wave action flux densities in natural units, $u_{1,2}$ are the linear electron quiver velocities in the waves, χ_e and χ_i are the conventional linear electron and ion dielectric susceptibilities evaluated at $(\omega_1-\omega_2, \mathbf{k}_1-\mathbf{k}_2)$, and $\varepsilon=1+\chi_e+\chi_i$. The perturbation theory leading to (2.38) assumes $|u_{1,2}/c|\ll 1$ and $|\omega_1-\omega_2| \ll \omega_1$, $\omega_2\sim\Omega_e$. The high-frequency wave energy flux densities, i.e., the power densities, are given by $\omega_{1,2}J_{1,2}$.

Conservation of wave action for collinear wave propagation follows directly from (2.38), which leads to $\Delta J_1=\pm\Delta J_2$ for parallel (+) or antiparallel (−) wave orientations. Relative to the energy introduced in the two transverse waves, only a fraction $q_e\approx\omega_3/[\omega_1(1+\omega_2\hat{\rho}/\omega_1)]$ can be acquired by the beat wave as a consequence of action-flux conservation ($\hat{\rho}=J_2^{\mathrm{in}}/J_1^{\mathrm{in}}$ is the input ratio of action fluxes). Analytical calculations (Cohen, 1984) have determined that the pump-depletion factor $R_a\equiv\Delta J_1/J_1^{\mathrm{in}}\to 1$ for $(\pi k_3^2L/k_1)|u_1u_2/c^2|>1$ in a plasma with a linear density gradient, $L^{-1}\equiv|\nabla \ln n_e|$. Detailed solutions for R_a are shown in Fig. 1 of Cohen, Cohen, Logan, *et al*, (1988). Good pump depletion enhances the heating and current-drive efficiencies associated with this scheme. Examples of the power requirements to achieve high beat-wave current-drive efficiencies in both MTX and a reactor plasma using FEL's are given by Cohen, Cohen, Logan, *et al.* (1988) and Sec. III.C here.

Beat-wave current drive offers the possibility of good efficiency and precise control over where and when the current is driven. Unwanted competition from neighboring cyclotron harmonics is easily avoided, and degradation of the current drive by magnetically trapped particles is weak. The accessibility of the beat wave is readily guaranteed by the easy accessibility of the driving waves. The penalty for this is the requirement of two intense microwave sources and the reduction of the heating and current-drive efficiency by the factor q_eR_a, where $q_e \lesssim \frac{1}{3}$ in most practical applications. The dependence of the beat-wave excitation mechanism on both the relative angle of the two microwave beams and the transverse beam profiles has been addressed in the calculations of Amin and Cairns (1990). Two-dimensional effects are important in determining optimal strategies for efficient beat-wave heating and current drive; the work of Amin and Cairns shows that collinear orientations are preferable and $q_eR_a=0.35$ can be achieved.

When the two transverse waves are aligned parallel to one another, the lower frequency transverse wave that is amplified by the beat-wave process can nonlinearly mix with the beat wave to excite a third transverse wave at frequency $\omega_2-(\omega_1-\omega_2)$ which acts as an additional pump wave to reinforce the generation of the beat wave. In fact, a cascade of frequency down-shifted transverse waves can be induced (Cohen *et al.*, 1972; Heikkinen *et al.*, 1988). Each cascade step can deposit another quantum of energy into the beat wave and the plasma which would circumvent the limitation associated with $q_e<1$ at each cascade step. Another potential benefit when the transverse waves are aligned parallel is that the beat wave produced has a high phase velocity approaching the group velocity of light in the plasma. This would facilitate the acceleration of electrons to relativistic energies (Tajima and Dawson, 1979; Heikkinen *et al.*, 1988). The principal disadvantages of the cascade are that owing to the dependence of the nonlinear coupling in (2.38) on k_3^2, which is much smaller for parallel beat-wave coupling than it is for the antiparallel orientation, much higher transverse-wave intensities are required and the competition with nonlinear self-focusing and parasitic parametric instabilities, e.g., stimulated Raman and Brillouin backscatter, may greatly inhibit beat-wave coupling in the parallel orientation and inhibit its efficiency (Cohen, Cohen, Logan, *et al.*, 1988).

Another variation of beat-wave current drive that overcomes the limit set by $q_e<1$ has been devised by Matsuda (1988). Only a single intense transverse pump wave is introduced to nonlinearly induce a parametric decay to a scattered transverse wave and a longitudinal wave, e.g., a Langmuir wave whose Landau damping on passing electrons heats the plasma and drives current. If the parametric instability can show a strong preference for producing a Langmuir wave propagating along the toroidal magnetic field line and lead to good depletion of the pump wave, then the product q_eR_a appearing in the heating and current-drive efficiency can be replaced by a factor that can approach unity in value.

In the examples of beam-wave excitation cited here, only Langmuir waves propagating parallel to the applied magnetic field have been analyzed. However, the coupling to other beat waves propagating at an oblique angle with respect to the magnetic field might provide a better vehicle for current drive. For example, a cyclotron-auto-resonant, upper-hybrid beat wave might lead to improved current-drive efficiencies by producing very hot electrons whose collisionality is significantly reduced.

Calculations of the current-drive efficiencies for the four mechanisms introduced in this section will be given in the next section. Examples of the simulations of these heating and current drive mechanisms are presented in Sec. V.

III. CURRENT-DRIVE APPLICATIONS

A. Pulsed current drive

The physics of quasisteady current drive using pulsed electromagnetic waves has been analyzed by Nevins (1987). The important time scales for current drive using intense, pulsed FEL's are

$$\tau_{\rm rf} \ll \nu_e^{-1} < T_{\rm rf} \ll T_{L/R} \; , \tag{3.1}$$

where $\tau_{\rm rf}$ is the pulse length of the electromagnetic wave source, ν_e is the electron collision frequency, $T_{\rm rf}$ is the time between pulses, and $T_{L/R}$ is the inductive/resistive decay time of the tokamak plasma. Because of the relatively high inductance and relatively low collisionality and resistance of a hot tokamak plasma, the $T_{L/R}$ time scale over which the plasma responds to changes in the toroidal current is long compared to the pulse length of the wave heating and the collisional relaxation time of the electrons. As a result, the following picture of current drive emerges.

The pulsed ECH shifts resonant electrons to higher energy where they collide less often and give rise to a current (Fisch and Boozer, 1980). Parallel momentum as well as energy can be delivered to the resonant electrons leading directly to current, especially for the beat-wave mechanism. The plasma's rapid response to the local infusion of current is to generate a backwards electromotive force (emf), which is produced by the time derivative of the magnetic flux according to Faraday's law. This accelerates the bulk electrons counter to the wave-heated electrons and cancels all but $O(T_{\rm rf}/T_{L/R})$ of the injected peak current as calculated by Nevins (1987). In between pulses, electron collisions relax the deformed electron velocity distribution; and both the back-emf and the fluctuating component of the current concomitantly decay. Because the peak cyclical perturbation of the current is smaller than the total average current by $T_{\rm rf}/T_{L/R}\ll 1$, a large average current can be sustained with pulsed injection. Nevins (1987) calculated this cyclical process in detail using circuit equations introduced in earlier work by Karney and Fisch (1986). Nevins also considered current-profile effects and the possibility of runaway production.

A simple model of non-inductive current drive was furnished by Cohen, Cohen, Nevins, *et al.* (1988). The toroidal current-balance equation deduced from electron momentum conservation and continuity is

$$\frac{d}{dt}j_\phi = S_\phi(t) - \nu_h j_\phi^h - \nu_b j_\phi^b + \frac{e^2 n_e}{m_e}E_\phi , \tag{3.2}$$

where $j_\phi = j_\phi^h + j_\phi^b$ is the total current summed over the heated component and the bulk electrons, ν_h and ν_b are the characteristic collision rates for the two electron components ($\nu_h < \nu_b$), and $S_\phi(t)$ is the time-dependent source of toroidal current introduced by electromagnetic waves, for example. The toroidal current j_ϕ acts as a source for the poloidal magnetic field as described by Ampere's law; and the time derivative of the poloidal magnetic flux induces a toroidal electric field E_ϕ as dictated by Faraday's law. At steady state, $dj_\phi/dt = E_\phi = 0$; and, if we assume that $\langle \nu_b j_\phi^b \rangle \ll \langle \nu_h j_\phi^h \rangle$, because j_ϕ^b is driven by E_ϕ (which is zero at steady state) and collisionally relaxes more rapidly than does j_ϕ^h, then Eq. (3.2) leads to $j_\phi \approx j_\phi^h \approx \langle S_\phi(t) \rangle / \nu_h$, where $\langle S_\phi(t) \rangle$ is the time-averaged current source. A current-drive efficiency is then readily obtained by dividing the current density integrated over the current channel by the input power in the electromagnetic waves. Examples of current-drive efficiencies that can be attained using various applications of intense, pulsed ECH are given later in this section. Detailed calculations of noninductive current drive based on solutions of the Fokker-Planck equation describing the collisional relaxation of the plasma and circuit equations for the evolution of the toroidal current and voltage have been presented in the comprehensive review of current drive by Fisch (1987).

B. Trapped-particle effects

By definition, trapped electrons are reflected by the increasing magnetic field as they follow field lines which wind around the torus to smaller major radius. Thus, trapped electrons carry no current on average. Their presence degrades current-drive efficiency in two different ways. Trapped electrons absorb energy without contributing to the current, and when initially passing electrons absorb energy so that they become trapped, there is a current increment produced opposite to that produced when the accelerated particle remains passing. There have been several calculations of trapped-particle effects on ECH (Start *et al.*, 1983; Chan *et al.*, 1982; Antonsen and Hui, 1984; Yoshioka *et al.*, 1986; Yoshioka and Antonsen, 1986; Harvey *et al.*, 1989; and R. Cohen, 1987).

R. Cohen (1987) used the adjoint methods of Yoshioka *et al.* (1986) to analytically solve the generalized Spitzer-Harm problem for the wave-driven current and the collisional relaxation of the perturbed distribution function including trapped-particle effects. It is assumed that the collisions are well described by scattering off a Maxwellian background. The introduction of a square-well approximation for the magnetic field facilitates an analytical solution. R. Cohen's calculation either models or retains all important relativistic effects. A Green's function for the linearized Fokker-Planck equation is derived from which the current drive can be calculated once the wave-induced particle flux Γ_W is specified for a particular current-drive mechanism.

The starting point of R. Cohen's calculation is the expression of Antonsen and Hui (1984), or, equivalently, of Fisch and Boozer (1980), for the wave-induced current:

$$\frac{J_\parallel}{B} = \left\langle \int d^3\mathbf{p}\,\Gamma_W \cdot \frac{\partial}{\partial \mathbf{p}} G \right\rangle , \tag{3.3}$$

where $\langle\ \rangle$ denotes a flux-surface average and $G = e\langle B_\phi/R \rangle^{-1} g \exp(\varepsilon/T)$. Here $R^{-1} \equiv |\nabla_\phi|$, ϕ is the toroidal angle, ε is the electron energy, T is the temperature of the background electrons, B_ϕ is the toroidal magnetic field, and g is the Spitzer-Harm distribution function modified to include magnetically trapped particles. The equation satisfied by g at steady state is

$$v_\parallel \hat{b} \cdot \nabla g + C(g) = -v_\parallel \hat{b} \cdot \nabla \phi \exp(-\varepsilon/T) , \tag{3.4}$$

where $C(g)$ is the collision operator linearized about a background Maxwellian of temperature T. This equation is bounce-averaged with g expanded in increasing powers of the ratio of the collision frequency to the transit (or bounce) frequency. The bounce-averaged collision operator is evaluated in the high-energy (but nonrelativistic) limit $mv^2/2T \gg 1$. Introducing $h = g\exp(\varepsilon/T)$ and $h = \langle R_\phi/R \rangle cF(v)H(\eta)/(4\nu v_t^3)$, where $R_\phi = B_\phi/B_0$, $F(v) = v/c$ in the nonrelativistic limit, $\nu = 4\pi n e^4 \ln\Lambda / m^2 v_t^3$, $v_t = (2T/m)^{1/2}$, $\eta = v_\perp^2/v^2$, and v is the speed, R. Cohen obtained the following inhomogeneous Legendre equation for H to leading order in T/mv^2,

$$-4H + \frac{1}{2}(1+Z)\frac{d}{d\lambda}(1-\lambda^2)\frac{dH}{d\lambda} = \pm 4\lambda , \tag{3.5}$$

where $\lambda = (1-\eta)^{1/2} = v_\parallel/v$, Z is the charge state of the ions, and the sign of the right side is determined by the sign of $v_\parallel$. The bounce-averaged collision operator was replaced by the local operator evaluated at the bottom of the magnetic well in obtaining Eq. (3.5). With the boundary conditions that H is regular at $\eta = 0$ and vanishes at the trapped-passing boundary $\eta = \eta_s = B_0/B_{\max}$ because H is finite only for passing particles, the analytic solution of (3.5) is

$$H = -\frac{4\lambda}{Z+5}\left[1 - \frac{\lambda_s}{|\lambda|}\frac{P_\alpha(|\lambda|)}{P_\alpha(\lambda_s)}\right] , \tag{3.6}$$

where P_α is a Legendre function with index α satisfying the relation $\alpha(\alpha+1) = -8/(1+Z)$. With this expression, g and, hence, G are determined; and with Γ_W specified for the particular current-drive mechanism, a $J_\parallel$ can be calculated from (3.3) that incorporates both relativistic and trapped-particle effects. R. Cohen (1987) used this Green's function approach to calculate analytically the current-drive efficiencies for conventional ECH and lower-hybrid current drive with continuous wave sources. For this purpose, quasilinear diffusion coefficients were employed for Γ_W. In addition, this analysis has been used as the basis of a current-drive diagnostic in particle simulations of intense, pulsed ECH and beat-wave current drive (Cohen, Cohen, Logan, *et al.*, 1988), whose results are reviewed in the following discussion of current-drive efficiencies.

C. Current-drive efficiencies

The most precise calculations of the current-drive efficiencies for the four mechanisms using intense pulses described in Sec. II are based on numerical particle-orbit calculations and self-consistent particle simulations. Examples of these calculations are presented in Sec. V. Here we will summarize the current-drive efficiencies obtained from orbit calculations and the particle simulations. These current-drive efficiencies for intense, pulsed ECH are quite attractive when compared to present experimental standards and equal or exceed the best theoretical current-drive efficiencies for conventional lower hybrid and ECH current drive (Cohen, Cohen, Nevins, *et al.*, 1988; Cohen *et al.*, 1989).

To calculate the current-drive efficiency in the numerical orbit integrations and particle simulations, a diagnostic (Cohen, Cohen, Logan, *et al.*, (1988) has been fashioned based on R. Cohen's (1987) analytical expression for $J_\parallel$ reviewed in Sec. III.B. The diagnostic incorporates relativistic and trapped-particle effects, and is applicable to situations where the pulse length of the electromagnetic waves is short compared to the characteristic collision time of the particles accelerated by the waves so that the arguments of Sec. III.A and Nevins (1987) are applicable. Thus, the net effect of the wave pulse is a finite displacement of the particles in phase space, which is instantaneous on the collisional time scale. The diagnostic then calculates the current driven both directly and by the subsequent collisional decay. While the calculation of Sec. III.B is nominally steady state, it is easily verified that the driven current derived from the Green's function in Eqs. (3.3)–(3.6) is valid even for time-dependent and nondiffusive radio-frequency operators. By retaining time derivatives in the Fokker-Planck equation for the velocity distribution function and integrating over time, the expression given in (3.3) remains valid, provided that $J_\parallel$ and Γ_W are replaced by their time-averaged values. Equation (3.3) can be put into the form

$$\frac{J_\parallel}{B}=\left\langle \int d^3\mathbf{p}\, DG \right\rangle , \tag{3.7}$$

where G was defined after Eq. (3.3) and

$$D=[\delta(\mathbf{p}-\mathbf{p}_f)\delta(\mathbf{x}-\mathbf{x}_f)-\delta(\mathbf{p}-\mathbf{p}_i)\delta(\mathbf{x}-\mathbf{x}_i)]\delta(t-t_0)$$

for a finite *instantaneous* displacement of a particle by a wave from $(\mathbf{x}_i,\mathbf{p}_i)$ to $(\mathbf{x}_f,\mathbf{p}_f)$. Thus, the total time-integrated current from the wave-induced deformation of the electron distribution function is

$$\int dt\, I=e(h_f-h_i) \tag{3.8}$$

where $h=g\exp(\varepsilon/T)$. The time-integrated current produced by a pulse is summed over particles and then divided by the sum of the absorbed energies to obtain a current-drive efficiency

$$\eta_{\rm cd}=\frac{I}{P}=\frac{e\sum(h_f-h_i)}{\sum(\varepsilon_f-\varepsilon_i)} . \tag{3.9}$$

In addition to the analytical expression for h given in Eqs. (3.5) and (3.6), R. Cohen (1987) derived a description based on a numerical solution for the angular part of h for circular flux surfaces that relaxed the square-well approximation for the magnetic field. The numerical expression was used in calculating $\eta_{\rm cd}$ by Cohen, Cohen, Logan, *et al.*, (1988) and Rognlien and Nevins (1987) for their particle simulations and orbit integrations; their results for $\eta_{\rm cd}$ differ at most by a few percent from those based on the analytical expression for h.

We now compare the current-drive efficiencies for three options exploiting the intensity of FEL pulses: rising buckets, stochastic acceleration, and beat waves. A relatively simple analytical formula for the current-drive efficiency of the beat-wave mechanism is reviewed here, which agrees fairly well with detailed numerical calculations over a range of beat-wave phase velocities. Cohen and Rognlien (1991) have derived a prescription for numerically calculating the rising-bucket current-drive efficiency, which is closely related to the numerical prescription used in conjunction with beat-wave current-drive simulations (Cohen, Cohen, Logan, *et al.*, (1988). The same kind of numerical prescription has been used to compute the current-drive efficiency for stochastic current drive. The Fokker-Planck analysis of Hizanidis (1989) has not been used to estimate the current-drive efficiency in the stochastic regime, because the orbit calculations of Hizanidis *et al.* (1989) have shown that the Fokker-Planck description for stochastic ECH is not valid for early or late times in a pulse. We have used the analysis reviewed in this section to determine the current-drive efficiencies numerically for the three options mentioned using intense FEL pulses and will summarize the results for the three representative examples of interest in magnetic fusion.

The first heating and current-drive mechanism described in Sec. II is superseded by rising buckets, because in practical applications $\hat{\mathbf{b}}\cdot\nabla B_0$ and $\hat{\mathbf{b}}\cdot\nabla k_\parallel$ are both finite. A conventional measure of current-drive efficiency is defined by $\hat{\eta}_{\rm cd}=nIR/P$, where n is the density in units of $10^{20}\ \mathrm{m}^{-3}$, I is the current in MA, R is the major radius in meters, and P is the power in MW. All three options can yield $\hat{\eta}_{\rm cd}$ in excess of the quasilinear value, which would be obtained in the limit of weak, diffusive ECH. For MTX applications (Thomassen, 1986; Jong *et al.*, 1989), stochastic current drive can yield the best efficiency in the range 0.1 to 0.2, neglecting ponderomotive effects, but is likely to be degraded by parametric instabilities, nonlinear self-focusing, and synchrotron radiation.

Rising-bucket current drive could yield efficiencies around 0.1 if a tail in the electron energy distribution can be drawn out to about 8 keV and if waves with $N_{\parallel} \approx 0.9$ can be propagated into the plasma. With less stringent conditions, $\hat{\eta}_{\rm cd} \sim 0.05$ for rising buckets can be achieved. Beat-wave current drive can produce $\hat{\eta}_{\rm cd} \approx 0.05$ with considerable control over where the current is deposited, but requires two intense microwave sources. Beat-wave current drive is the only one of the three options that does *not* generate loss-cone-like distributions, which may excite microinstabilities. All three options yield $\hat{\eta}_{\rm cd} \sim 0.3$ when applied to the International Thermonuclear Experimental Reactor (ITER), which has a much hotter plasma ($T_e = 20-25$ keV in ITER and 2 keV in MTX). Current-drive calculations for the Compact Ignition Tokamak (CIT, renamed the Burning Plasma Experiment, BPX) at $T_e = 10$ keV lead to efficiencies that are intermediate between MTX and ITER (see Table II).

We next review the current-drive efficiencies for the three options using intense pulses in more detail. The case of conventional low-amplitude ECH current drive, which infinitesimally displaces resonant electrons, is a useful standard of comparison. The quasilinear ECH current-drive efficiency has been evaluated using the calculation of R. Cohen (1987). Cohen points out that the efficiency is greatest for absorption on the low-field side of resonance and at the inside of the flux surface (the former so as to have additive direct-momentum and anisotropic resistivity contributions to the driven current; the latter so as to minimize trapped-particle effects). The efficiency varies almost linearly with the energy of the resonant electrons. For MTX parameters with $T_e = 2$ keV and $l\Omega_0/\omega = 0.92$, $\hat{\eta}_{\rm cd}$ varies from 0.028 for $\varepsilon/T_e \approx 3$ to 0.042 for $\varepsilon/T_e \approx 5$, where ε is the resonant energy. For ITER parameters, $T_e = 20$ keV and $l\Omega_0/\omega = 0.8$, we have $\hat{\eta}_{\rm cd} \approx 0.3$ for $\varepsilon/T_e = 5$ and $l = 1$. At higher energies ε, there is competition from the second-harmonic resonance that degrades $\hat{\eta}_{\rm cd}$; and this competition sets in at lower values of ε for $l > 1$. Rising-bucket physics can enhance the current-drive efficiency in two ways. First, there is the direct effect of acceleration to high energies, particularly if the range of $N_{\parallel}$ extends to near unity [see Eq. (2.34)]. When the absorption is on the inside of the flux surface and power is launched from the outside, this effect enhances the efficiency on that flux surface. (When the absorption is on the outside or power is launched from the inside, the accelerated buckets can deposit their electrons in or close to the trapped-particle region of momentum space, resulting in a decrease in efficiency.) Additionally, there is an indirect benefit, which can be even more significant, resulting from the possible increase of opacity over linear values. Increased opacity implies absorption farther from the cyclotron resonance layer, which, for outside launch, implies absorption by higher-parallel-energy electrons and, hence, higher current-drive efficiency.

TABLE II. Representative ECH current-drive efficiencies nIR/P (10^{20} A/m^{2}W).

Mechanism	MTX	CIT	ITER
Quasilinear	0.03–0.04	0.1–0.15	0.2–0.3
Beat waves	0.03–0.05	0.2	0.2–0.4
Rising buckets	0.05–0.1	0.2–0.4	0.3–0.6
Stochastic	0.1–0.2	0.15–0.3	0.2–0.4

Rising-bucket current drive has been studied using numerical integration of particle orbits (Sec. V) and an analytical model. The current-drive efficiency is deduced from Eq. (3.9) in both calculations. The analytic estimate proceeds as follows (Cohen and Rognlien, 1991); the current-drive efficiency is estimated by evaluating it [from the relation (3.9)] on a representative characteristic whose minimum energy (in the illuminated portion of momentum space) $\varepsilon_{\rm min}$ is greater by T than ε_0, the minimum energy in all of the illuminated portion of momentum space. Since rising-bucket current drive is primarily of interest for a spread of $N_{\parallel}$ sufficient to make the range of energy along the representative characteristic large compared to the temperature T, we evaluate the current-drive efficiency by assuming that all particles are moved along this characteristic from energy $\varepsilon_{\rm min} + T$ to $\varepsilon_{\rm max}$, the maximum energy on the illuminated portion of the characteristic. The choice $\varepsilon_{\rm min} + T$ accounts for phase-space displacement effects: in the "sudden adiabatic turn-on and turn-off" approximation described in the discussion of the opacity calculation, electrons would be trapped at $\varepsilon_{\rm min}$, but phase-space displacement fills in the empty hole in phase space. The net effect is equivalent to electrons being trapped at energy T above the minimum. Finally, if we wish to estimate the current-drive efficiency for the entire ray-bundle rather than a single flux surface, the evaluation is done on a representative flux surface where much of the absorption occurs, chosen so that $\varepsilon_0 \approx T \ln(1 + \tau_{\rm NL}/2)$.

In order to benchmark this procedure and also assess the direct enhancement of the current-drive efficiency on a given flux surface, Cohen and Rognlien (1991) carried out this simplified procedure and compared the efficiencies with those inferred from orbit-code calculations (for a single flux surface, with specified ε_0) for several sets of plasma parameters, as shown in Table III. The ε_0 values chosen are representative of the bulk electron temperatures in MTX (2 keV) and ITER (20 keV) (although, in ITER, the opacities for harmonics such that the bucket mechanism is effective are sufficiently high that the microwaves would not be expected to penetrate to flux surfaces where ε_0 is this low). The various values of T serve to mock up the effect of previous FEL pulses in producing a tail in the resonant portion of the electron distribution function. We observe from Table III that the analytic procedure tends to underestimate the numerical efficiency, by anywhere from 0 (one case) to over 50%. Also shown in Table III are efficiencies for conventional (quasilinear) ECH evaluated on the representative

TABLE III. Comparison of analytic and numerical current-drive efficiencies for intense ECH and weak-ECH (quasilinear) efficiency. Here θ is the poloidal angle at which absorption occurs ($\theta=0$ is the outside of the flux surface); $\eta=n(10^{20}\ \mathrm{m}^{-3})I(\mathrm{A})R(\mathrm{m})/P(\mathrm{W})$, where P is the absorbed power, and ε_0 is the minimum resonant energy (consistent with Y and $N_{\parallel 2}$).

ε_0 (keV)	Y	$N_{\parallel 2}$	T (keV)	θ	η_{anal}	η_{num}	η_{weak}
20	0.8	0.846	20	π	0.22	0.30	0.22
				$\pi/2$	0.20	0.26	0.20
				0	0.18	0.21	0.19
			50	$\pi/2$	0.34	0.39	0.28
20	0.78	0.917	20	$\pi/2$	0.25	0.29	0.20
			50	$\pi/2$	0.43	0.42	0.29
2	0.93	0.835	2	π	0.032	0.054	0.020
				$\pi/2$	0.018	0.034	0.017
				0	0.001	0.008	0.014
			6	π	0.071	0.104	0.036
				$\pi/2$	0.046	0.071	0.033
2	0.923	0.914	2	π	0.048	0.075	0.020
				$\pi/2$	0.026	0.048	0.017
			6	π	0.106	0.126	0.036
				$\pi/2$	0.072	0.087	0.033

characteristic. As anticipated from the preceding discussion, the rising-bucket efficiencies (particularly the numerically calculated values) exceed quasilinear for absorption on the inside of the flux surface, but not necessarily for absorption on the outside.

Assessment of the indirect effect of increased opacity on global current-drive efficiency is more difficult, as it involves issues such as the tradeoff of opacity with competition from absorption at higher harmonic numbers (Smith *et al.*, 1987); the required ray-tracing studies have not yet been done. A measure of the effect is provided, however, by the simple criterion $\varepsilon_0 \approx T \ln(1+\tau_{\mathrm{NL}}/2)$ introduced above. In the limit where the energy gained by a bucket, Eq. (2.34), is small compared to $\varepsilon_{\min}$, the nonrelativistic current-drive efficiency scales approximately with $\varepsilon_{\min}$; hence the efficiency would increase by a factor of roughly $[1+\ln(1+\tau_{\mathrm{NL}}/2)]/[1+\ln(1+\tau_{\mathrm{L}}/2)]$. For fundamental O-mode current drive in ITER, this factor would be about 1.4. The finiteness of the energy increment will tend to increase this ratio, while relativistic effects decrease it. More detailed studies can be found in Cohen and Rognlien (1991).

The combination of increased opacity, increased current-drive efficiency, and harmonic selectivity of the bucket adiabaticity criterion can assist in overcoming the limit on conventional ECH current-drive efficiency imposed by harmonic competition (Smith *et al.*, 1987). It is not difficult to arrange for a particular harmonic to be adiabatic, while higher harmonics are not. Hence, one can exploit the advantage of increased opacity to plow a larger fraction of the wave energy into absorption at the desired harmonic, and it will do so with enhanced current-drive efficiency. With proper ray aiming, the higher harmonics, for which current is driven in the wrong direction, absorb less of the power and drive current with the relatively lower linear-ECH current-drive efficiency.

The primary outstanding issues associated with rising-bucket current drive are microstability (see Sec. IV.D) and the degree of penetration of individual ECH rays. The success of the direct enhancement of the current-drive efficiency depends on the highest $N_{\parallel}$ rays penetrating to where they are needed; they must not absorb at a significantly larger minor radius than where the lower $N_{\parallel}$ rays are absorbed. Assessment of this requirement, as well as quantitative evaluation of the global effect of increased opacity on current-drive efficiency, requires implementation of nonlocal, per-ray absorption coefficients into a ray-tracing code.

Particle orbits have been numerically integrated to calculate the current-drive efficiency for stochastic acceleration (Rognlien and Nevins, 1987). The particle-orbit calculations determine the final momentum-space distribution resulting from a Maxwellian population passing through the intense FEL pulse. This data is then used in the current-drive diagnostic Eq. (3.9) to calculate the net current driven during the subsequent collisional relaxation. The current drive is then obtained from the ratio of the integrated current to the energy absorbed. Results for stochastic acceleration on the magnetic axis are shown in Fig. 10 for two angles of propagation with respect to $\mathbf{B}_0$ as a function of the right-hand circularly polarized electric field strength, E_{cr}/B_0. Ponderomotive effects have been omitted here. The threshold for stochasticity at 70° is lower than at 45°, but the maximum obtainable efficiency is higher at 45° because that wave has more parallel momentum. The initial temperature of the distribution in these examples is 1 keV. For an initial

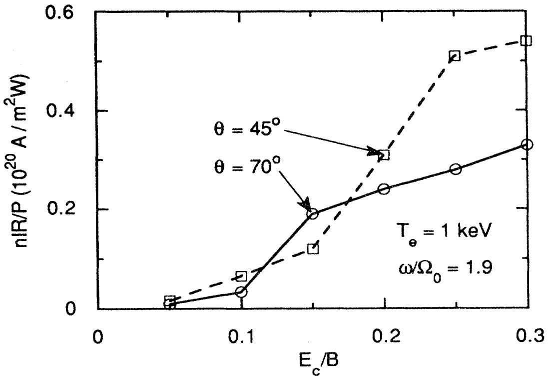

FIG. 10. Stochastic current-drive efficiency nIR/P (10^{20} A/m^2 W) on axis as a function of the normalized right-hand electric field amplitude E_c/B_0 for $\theta=45°$ and 70° angles of incidence, $\omega/\Omega_0=1.9$, and $T_e=1$ keV.

temperature of 20 keV, the maximum efficiencies are similar but the threshold for stochastic acceleration extends to lower E_{cr}/B_0. Current-drive efficiencies as high as 0.2 can be obtained for values of E_{cr}/B_0 corresponding to a 8 GW pulse with focusing to a 0.5 cm beam radius and $B_0=5$ T, but the results are quite sensitive to the electric-field strength. Trapped-particle effects are not included in the results plotted here and reduce the efficiencies by factors of 0.5 and 0.7 for angles of 70° and 45°, respectively.

Beat-wave current-drive efficiencies have been calculated analytically and in self-consistent particle simulation (Cohen, Cohen, Logan, *et al.*, 1988). The electron current density introduced on each toroidal transit of the electrons is directly calculated from the momentum flux density liberated by the resonantly damped beat wave, whose damping is assumed to be complete if the phase velocity of the beat wave does not fall too far out on the tail of the electron velocity distribution. Because the three-wave interaction producing the beat wave conserves wave-action flux as well as momentum and energy flux, the momentum and current sources for the electrons are proportional to the wave power available to the beat wave, which is given by q_eR_a times the input power in the high-frequency pump wave, where q_e is the quantum efficiency and R_a is the relative action transfer defined and discussed in Sec. II. It is shown by Cohen, Cohen, Logan, *et al.*, (1988) that the current-drive efficiency for beat waves can be derived from Eq. (3.2) and is given by

$$\hat{\eta}_{\mathrm{bw}}=q_eR_a\frac{e}{m_e\nu_h}\frac{1}{2\pi R_0 v_\parallel}\,, \tag{3.10}$$

where ν_h is the classical collisional slowing-down rate for a fast electron and $v_\parallel=(\omega_1-\omega_2)/(\mathbf{k}_1-\mathbf{k}_2)\cdot\hat{\mathbf{b}}$ is the parallel velocity of the electrons resonantly damping the beat wave.

A careful relativistic treatment of radio-frequency current drive for an electrostatic wave that is completely damped by resonant particles gives a current-drive efficiency (Fisch, 1987)

$$\hat{\eta}_{\mathrm{cd}}=\frac{I_{\mathrm{cd}}}{P_{\mathrm{cd}}}=\frac{31.2}{\ln\Lambda}\left[\frac{\hat{J}}{\hat{P}}\right]\frac{1}{R_0(m)n_e(10^{20}\,\mathrm{m}^{-3})}\,, \tag{3.11}$$

where $\hat{J}/\hat{P}$ is a function of the momentum of the current-carrying particles. In the nonrelativistic limit with $v_\parallel \gg v_\perp$, $\hat{J}/\hat{P}=8x^2/(5+Z_{\mathrm{eff}})$ and $x^2=2\varepsilon/mc^2$ where ε is the energy of the resonant electrons. The beat-wave current-drive efficiency $\hat{\eta}_{\mathrm{bw}}=nIR/P$ is reduced by q_eR_a so that

$$\hat{\eta}_{\mathrm{bw}}=q_eR_a\hat{\eta}_{\mathrm{cd}}\approx 0.8\times10^{-2}q_eR_a\varepsilon\ (\mathrm{keV}) \tag{3.12}$$

in the nonrelativistic limit, with $8/(5+Z_{\mathrm{eff}})\approx1$ and $31.2/\ln\Lambda\approx2$. There is good agreement between (3.12) and (3.10). For resonant velocities where relativistic effects begin to be important, the current-drive efficiency saturates with increasing electron energy: $\hat{J}/\hat{P}=O(1)$ for $x=p_\parallel/mc>O(1)$ and $p_\perp \ll p_\parallel$. The current-drive efficiency depends on both the peak electromagnetic wave power (to achieve a satisfactory value of R_a) and the energy of the current-carrying electrons (which determines $\hat{J}/\hat{P}$ and thus $\hat{\eta}_{\mathrm{cd}}$). Trapped-particle effects should have little influence for beat-wave current drive involving an acceleration of the electrons that is mainly parallel to the magnetic field and which can be done on the inside of the magnetic axis.

Particle simulations of beat-wave current drive were performed with the EMONE electromagnetic code (Cohen *et al.*, 1975; Cohen, Cohen, Logan, *et al.*, 1988). The current-drive diagnostic described in this section was incorporated in the simulations. The results of parameter studies, in which the absolute phase velocity of the beat wave $\Delta\omega/\Delta k v_e$ was varied with the initial plasma temperature fixed at a value of 3 keV representative of MTX and 20 keV for ITER, are shown in Fig. 11. The current-drive efficiency $\hat{\eta}_{\mathrm{bw}}$ peaked at $\Delta\omega/\Delta k v_e\sim4.5$ with $\hat{\eta}_{\mathrm{bw}}\sim0.05$. For the significantly hotter ITER plasma, $\hat{\eta}_{\mathrm{bw}}$ peaked at $\Delta\omega/\Delta k v_e\sim2.5$ with $\hat{\eta}_{\mathrm{bw}}\gtrsim0.3$. The simple analytical expressions (3.10) and (3.12) are reasonably accurate in predicting $\hat{\eta}_{\mathrm{bw}}$ for $\Delta\omega/\Delta k v_e$ less than the optimal values, although they slightly underestimate the current-drive efficiencies obtained in the simulations. Furthermore, because the analytical expressions assumed that the plasma wave was completely damped by the electrons for all beat-wave phase velocities, the analytical expressions grossly overestimate the current-drive at high phase velocities where the Landau damping becomes too weak and there are insufficient numbers of electrons to carry the current. Specific beat-wave current-drive scenarios were calculated for MTX by Cohen, Cohen, Logan, *et al.*, (1988) using particle simulations and a ray-tracing code.

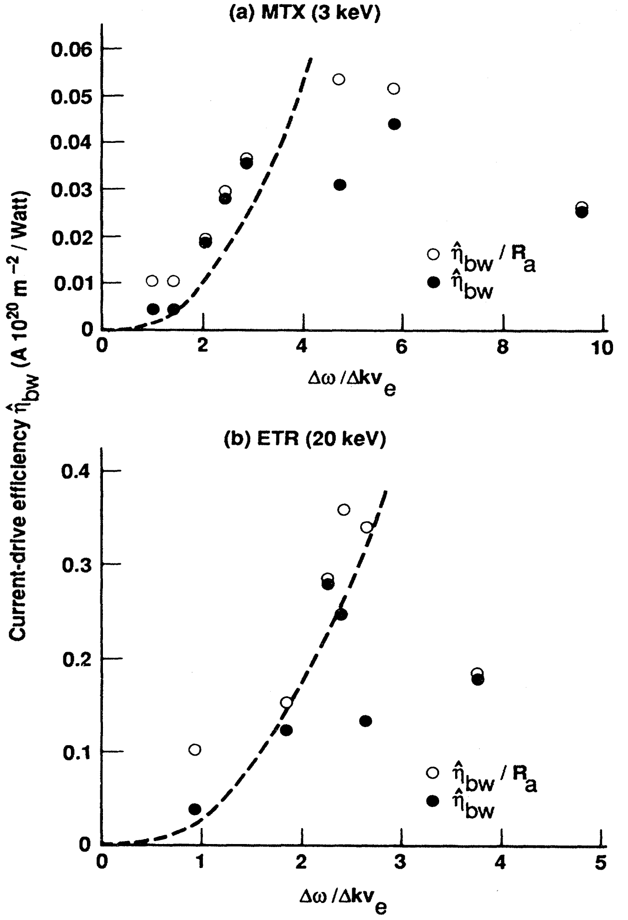

FIG. 11. Beat-wave current-drive efficiency $\hat{\eta}_{\rm bw}$ and $\hat{\eta}_{\rm bw}/R_a$ (to correct for the incomplete action transfer in artificially short simulations) as a function of the beat-wave relative phase velocity $\Delta\omega/\Delta k v_e$ for MTX and reactor cases (Cohen, Cohen, Nevins, *et al.*, 1988).

IV. STABILITY OF AN INTENSE ELECTRON CYCLOTRON WAVE

Numerous nonlinear effects can occur when an intense, coherent electromagnetic wave impinges upon a plasma. We have already reviewed several nonlinear aspects of the wave-particle interaction. In this section we review the possible parametric destabilization of waves in the plasma as the result of ponderomotive effects and trapped particles induced by an intense electron cyclotron wave. We also review nonlinear self-focusing and a first theoretical study of the microstability of an FEL-heated plasma. These nonlinear phenomena are important because they can result in the absorption, depletion, scattering, or modulation of the FEL, which may be deleterious to the intended application of the FEL to heating, current drive, or control of magnetohydrodynamic instabilities through localized current drive. If the heated electron distribution is unstable, the resulting wave turbulence can lead to anomalous heat and particle transport. In addition, electron microinstability can be used as a diagnostic of the plasma heating.

A. Parametric instabilities

The parametric instability of the plasma heated with cyclotron waves is a mature area of research, and there have been numerous theoretical analyses and papers reported experimental observations. A number of theoretical reviews and surveys have been published. The literature is so extensive that we shall direct the interested reader to only a few exemplary papers and the references therein, which will serve as an introduction to the literature. We shall present the general dispersion relation describing the parametric decay of an electromagnetic plane wave in a uniform magnetized plasma into both electromagnetic and electrostatic waves. We shall identify some of the most important parametric instabilities that might be encountered for an intense electron cyclotron wave.

Porkolab (1977, 1978) reviewed the theoretical analysis and experimental status of parametric instabilities associated with wave heating of magnetically confined plasmas. Porkolab's theoretical calculations assumed that the incident electromagnetic wave had a negligible wave number in the region where it nonlinearly decayed into electrostatic waves in the plasma. A number of possible decay products were considered. Ott, Hui, and Chu (1980) analyzed electrostatic decay instabilities for finite-wave-number pump waves with frequencies near the electron cyclotron frequency. Stefan and Bers (1984) surveyed parametric instabilities associated with electron cyclotron heating that lead to nonlinear absorption; they analyzed a dispersion relation for finite-wave-number ordinary and extraordinary pump waves which decay into electrostatic waves and were particularly interested in the secondary decay instabilities of the parametrically destabilized electrostatic waves. Stefan and Krall (1985) reviewed nonlinear conversion and parametric absorption of finite-wave number electron cyclotron waves as applied to the heating of bumpy torus plasmas. The secondary parametric decay and possible cascade of the decay products, as well as pump depletion, were among the saturation mechanisms analyzed by Stefan and Krall.

The generalization of the dispersion relations describing parametric decays into electrostatic waves to include stimulated scattering has been presented by B. Cohen (1987a), Stefan *et al.* (1987), Stenflo (1989), and others. In stimulated scattering, an incident electromagnetic wave can parametrically couple to a scattered electromagnetic wave and another mode that is typically an electrostatic normal mode or quasimode in the plasma. In a uniform magnetized plasma, the dispersion relation for both stimulated scattering and a parametric decay into electrostatic modes for weakly nonlinear incident electromagnetic wave is (B. Cohen, 1987a; Stefan *et al.*, 1987)

$$\varepsilon-\tfrac{1}{4}\chi_e(1+\chi_i)\left[\frac{k^2|\mathbf{k}_+\times\mathbf{v}_0|^2}{k_+^2D_+}-\frac{k^2(\mathbf{k}_+\cdot\mathbf{v}_0)^2}{k_+^2\omega_+^2\varepsilon_+}+\frac{k^2|\mathbf{k}_-\times\mathbf{v}_0|^2}{k_-^2D_-}-\frac{k^2(\mathbf{k}_-\cdot\mathbf{v}_0)^2}{k_-^2\omega_-^2\varepsilon_-}\right]=0 \tag{4.1}$$

for $v_e^2, v_0^2 \ll c^2$, $k_{0\perp}\rho_e \ll 1$, and $\omega_0 \gg \omega, \Omega_i, \omega_{\rm pi}$, where ρ_e is the electron Larmor radius, v_e is the electron thermal speed, $\omega_{\rm pi}$ is the ion plasma frequency, χ_e and χ_i are the linear susceptibilities in a warm, magnetized plasma evaluated at $(\omega,\mathbf{k})$, $\varepsilon = 1+\chi_e+\chi_i$ is the linear longitudinal dielectric function evaluated at $(\omega,\mathbf{k})$, $D_\pm \equiv (\mathbf{k}\pm\mathbf{k}_0)^2c^2 - (\omega\pm\omega_0)^2\varepsilon_\pm$, $\varepsilon_\pm = \varepsilon(\omega\pm\omega_0, \mathbf{k}\pm\mathbf{k}_0)$, and $\mathbf{v}_0$ is the linear oscillation velocity of an electron in the electromagnetic pump wave in the presence of an applied magnetic field. The derivation of (4.1) depends on a perturbation expansion in the pump-wave amplitude and does not include relativistic or trapping effects. The stability of an intense electromagnetic wave to the growth of sidebands in the presence of wave-trapped electrons is reviewed in Sec. IV.B.

Equation (4.1) describes stimulated scattering, filamentation, and parametric decay instabilities with $\omega \ll \omega_0$. Parametric decay into two upper-hybrid waves or two obliquely propagating, magnetized plasma waves is not included in (4.1), in analogy to the similar observation for an unmagnetized plasma (Drake *et al.*, 1974). Stenflo (1989) showed that Eq. (4.1) can be straightforwardly generalized to include collisions. The dispersion relation Eq. (4.1) acquires additional terms for an amplitude-modulated electromagnetic pump wave, as has been illustrated for ion-cyclotron pump waves by Similon and Kaufman (1984), D'Ippolito and Myra (1985), Cohen and Rognlien (1985), and Otani and Cohen (1988). Equation (4.1) yields the dispersion relation for parametric decay or stimulated scattering by a low-frequency electrostatic normal mode when $\varepsilon(\omega,\mathbf{k})$ nearly vanishes. The electromagnetic pump wave couples the low-frequency mode to upper and lower-frequency sidebands $(\omega\pm\omega_0, \mathbf{k}\pm\mathbf{k}_0)$. When D_+ or D_- nearly vanish, and ε_+ and ε_- are finite, the pump wave couples the low-frequency electrostatic mode to an electromagnetic sideband; this corresponds to stimulated scattering. When ε_+ or ε_- nearly vanish, and D_+ and D_- are finite, the dispersion relation describes parametric decay to electrostatic decay products. When the coupling is strong enough, a sideband can couple unstably to a low-frequency quasimode or to a heavily damped mode (nonlinear Landau damping or stimulated Thomson scattering) for which ε is finite. Filamentation is an example of two electromagnetic sidebands coupling equally strongly to a low-frequency quasimode. The oscillating two-stream instability is an example of two electrostatic sidebands coupling equally strongly to a low-frequency quasimode.

Porkolab and Cohen (1988) used Eq. (4.1) to survey the potential for parametric instabilities associated with intense electron cyclotron heating in the MTX. They analyzed the parametric instability of ordinary modes perpendicularly incident from the outside of the torus at a frequency near the fundamental electron cyclotron frequency and extraordinary modes perpendicularly incident from the outside of the torus at the second harmonic of the electron cyclotron frequency. Both nonlinear decays into electrostatic modes (absorptive instabilities) and stimulated scattering (reflective instabilities) were considered for a collisionless plasma with parameters appropriate to MTX. Local growth rates, threshold conditions, and convective stabilization criteria were calculated for several important parametric instabilities. When the pump wave decays into two normal modes, the local threshold condition is $\gamma_0^2 > \Gamma_1\Gamma_2$, where γ_0 is the local growth rate, and Γ_1 and Γ_2 are the damping rates of the decay products. In a nonuniform plasma, the threshold condition for instability to overcome convec-

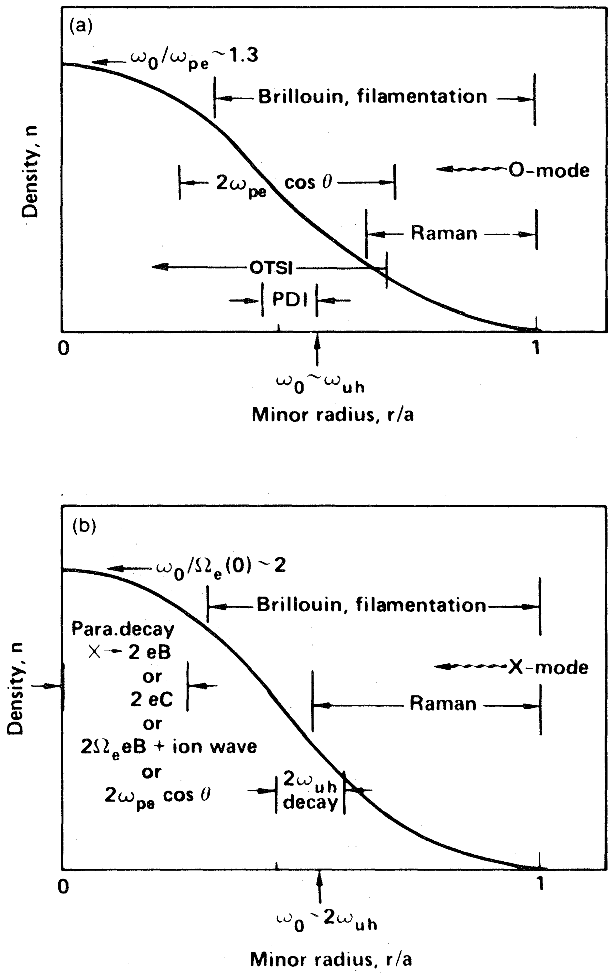

FIG. 12. Schematic of parametric processes associated with (a) ordinary-mode ($\omega_0 \approx \Omega_e$) and (b) extraordinary mode ($\omega_0 \approx 2\Omega_e$) wave heating. eB denotes an electron Bernstein wave, eC denotes an electron cyclotron wave, PDI is the parametric decay instability, and OTSI is the oscillating two-stream instability.

TABLE IV. Parametric instabilities for ordinary-mode heating in MTX.

Instability	$(\omega,\mathbf{k})$ matching satisfied	Importance, comments
Reflective		
1. Raman scattering by upper hybrid wave	No	No
2. Raman scattering by lower hybrid wave	Yes	No, convectively stable
3. Brillouin scattering by ion cyclotron wave	Yes	Unstable, maybe important
4. Brillouin scattering by ion quasimode	Yes	Unstable, maybe important
5. Brillouin scattering by ion Bernstein wave	Yes	No, convectively stable
Absorptive		
6. Decay to upper hybrid and ion quasimode	Yes	No, convectively stable
7. Oscillating two-stream	Yes	Unstable
8. Parametric decay to two magnetized plasma waves	Yes	Probably important if $\frac{1}{4} \le \omega_{pe}^2/\Omega_e^2 \le 1$

tive losses is $\gamma_0^2 \gg K' V_{1x} V_{2x}$, where $K' \equiv \nabla\cdot(\mathbf{k}_0 - \mathbf{k}_1 - \mathbf{k}_2)$, and V_{1x} and V_{2x} are the group velocities of the decay waves in the direction of the inhomogeneity. When the low-frequency wave is a quasimode and the sideband is a normal mode, the local threshold condition is $\gamma_0 > \Gamma_2$, and the convective threshold is $\gamma_0 > |V_{2x}(d\varepsilon_-/dx)|$. Figure 12 displays a schematic of the important phenomena, and Tables IV and V summarize the conclusions of Porkolab and Cohen (1988) and Perkins (1988) for MTX. Perkins (1988) corrected the assessment of Porkolab and Cohen of the oscillating two-stream instability for the ordinary mode and showed that it can be important in MTX.

There are several absorptive parametric instabilities that are likely to occur at high power in MTX. The absorptive instabilities will divert wave power into other waves, which will heat the plasma, but will also increase the level of wave turbulence. The increased level of turbulence can be deleterious to particle and energy confinement. The reflective instabilities are dangerous because they can result in scattering significant amounts of the incident wave energy from its intended purpose. In this regard, Brillouin backscatter by forward and backward electrostatic ion cyclotron waves have the lowest local and convective thresholds, and have appreciable local growth rates, $\gamma_0 = O(\Omega_i)$. Brillouin backscatter is predicted to exhibit significant convective amplification for the 8 GW and 50 nsec pulses anticipated in MTX unless nonlinear effects limit the backscatter. For larger and hotter target plasmas than in MTX, the area of the laser spot size can be increased and both v_0/v_e and v_0/c can be reduced, which will diminish the possibility and strength of parametric instabilities. Increasing the frequency bandwidth and using very short laser pulses can also lessen the risk of parametric instabilities (Porkolab and Cohen, 1988).

TABLE V. Parametric instabilities for X-mode heating in MTX.

Instability	$(\omega,\mathbf{k})$ matching satisfied	Importance, comments
Reflective		
1. Raman scattering by upper hybrid waves	Yes	Yes, convectively unstable
2. Raman scattering by lower hybrid waves	Yes	No, convectively stable
3. Brillouin scattering by ion cyclotron wave or quasimode	Yes	Yes, convectively unstable
4. Brillouin scattering by ion Bernstein waves	Yes	No, convectively stable
Absorptive		
5. Parametric decay: X→2 upper hybrid waves	Yes	Yes, convectively unstable, maybe absolute
6. Parametric decay: X→2 electron Bernstein or electron cyclotron or two magnetized plasma waves	Yes	Yes, convectively unstable, maybe absolute
7. Parametric decay: X→upper hybrid + ion quasimode	No	No, cannot satisfy matching
8. Oscillating two-stream: 2X→2 upper hybrid + quasimode	No	No, cannot satisfy matching
9. Parametric decay: X→2 electron Bernstein wave + ion wave	Yes	Yes, convectively unstable

B. Trapped-particle sideband instability

When a large-amplitude, monochromatic wave resonantly accelerates particles and traps them, the cyclical motion of the trapped particles causes a beating with the principal wave that can destabilize sidebands separated in frequency by the trapping frequency from the principal wave. This phenomenon has been observed experimentally and analyzed theoretically for Langmuir waves by Kruer *et al.* (1969) and for whistlers by Denavit and Sudan (1975). More recently, Cohen and Cohen (1988a, 1990) derived the dispersion relation for an electromagnetic trapped-particle sideband instability for a large-amplitude ordinary mode at perpendicular incidence as proposed in the FEL experiments in MTX.

A sideband instability could have at least two possibly important effects on FEL heating experiments. For the case that $\nabla_{\parallel} k_{\parallel 0}=0$, the modulation induced by unstable sidebands could broaden the power spectrum, detrap the resonant electrons, and improve the overall absorption. In the second case, consider $\nabla_{\parallel} k_{\parallel 0}\neq 0$, $\nabla_{\parallel}\mathbf{B}_0\neq 0$, and FEL heating exploiting the rising-bucket concept. A strong sideband instability could detrap resonant electrons and "spill" the buckets, preventing improved absorption. For parameters appropriate to high-power FEL operation in MTX, Cohen and Cohen find a weakly unstable sideband instability with growth rates that are steeply peaked at the frequencies $\omega_0 \pm \omega_b$, where ω_0 is the frequency of the principal ordinary mode and ω_b is the trapped-particle bounce frequency calculated in Eq. (2.8). The local growth rate γ_0 is sufficient in MTX to exceed the threshold condition set by collisional damping of the sidebands, $\gamma_0^2 > \Gamma_+ \Gamma_-$ where $\Gamma_\pm \approx (\omega_{pe}^2/\omega_0^2)\nu_{ei}/2$ and ν_{ei} is the electron-ion collision rate. However, the growth rate is weak ($\gamma_0 \approx 10^{-5}\Omega_e$); and the sidebands convect rapidly at the group velocity of the ordinary wave with a spatial gain length that greatly exceeds the minor radius of MTX.

The derivation of the dispersion relation due to Cohen and Cohen (1988a, 1990) is reasonably straightforward, and only a brief synopsis will be given here. The relativistic Hamiltonian introduced in Sec. II.A is expanded about the principal elliptic fixed point to second order in the excursions in P_θ and θ to describe the trapping in the principal wave. The linear perturbation to this Hamiltonian due to the upper and lower sidebands ($\omega \pm \omega_0$, $\mathbf{k} \pm \mathbf{k}_0$) is introduced. The linear perturbation has the form of H_1 in Eq. (2.6), but is summed over both sidebands. The solution of the linearly perturbed motion now resembles closely that of a harmonic oscillator whose natural frequency is ω_b being driven by a plane wave with frequency ω_0. From the solution of the linearly perturbed motion, the linearly perturbed electron distribution function is obtained by introducing a Klimontovich representation. The linearly perturbed current $j_z^{(1)}$ is then calculated by integrating over the perturbed distribution function for use in Maxwell's equations to determine the sideband field amplitudes self-consistently. The determinant of the sideband coefficients matrix yields the dispersion relation describing the normal modes:

$$1-M\left[\frac{1}{D(\omega+\omega_0,k+k_0)}+\frac{1}{D(\omega-\omega_0,k-k_0)}\right]=0\ , \tag{4.2}$$

where $D(\omega \pm \omega_0, k \pm k_0)=c^2(k \pm k_0)^2-(\omega \pm \omega_0)^2+\omega_{pe}^2$, $\mathbf{k}$ and $\mathbf{k}_0$ are parallel,

$$M=(\omega_t^2/32\gamma)(p_z/p_\perp)^2(k_0\rho)^2(kv_0)^2(\omega_b^2-\omega^2)^{-1}\ ,$$

γ is the relativistic factor at the elliptic fixed point, p_z and $p_\perp$ are the corresponding momenta, and ω_t is the electron plasma frequency for the density of trapped electrons. This dispersion relation is identical in form to the dispersion relations for the Langmuir (Kruer *et al.*, 1969) and whistler (Denavit and Sudan, 1975) sideband instabilities. For $|kk_0c^2/\omega_0<\omega_b|$ there is instability, and for $\omega \neq \omega_b$ the frequency is given by

$$\omega=kk_0c^2/\omega_0 \pm i\{\beta k^4N^2(1-N^2)$$
$$\times\omega_0^4([k_0^4(\omega_b^2-k^2k_0^2c^4/\omega_0^2)])^{-1}\}^{1/2}\ ,$$

where $N=k_0c/\omega_0$, $\beta=(N^4\omega_t^2/64\gamma\omega_0^2)(v_0v_ep_z/c^2p_\perp)^2$, and $v_e=\rho\Omega_e$. The maximum growth rate peaks sharply at $kk_0c^2/\omega_0=\omega_b$ and

$$\omega=\omega_b+(1/2+i\sqrt{3/2})(\beta/2)^{1/3}\omega_bN^{-2}(1-N^2)^{1/3}\ .$$

There is stability for $kk_0c^2/\omega_0>\omega_b$.

The sideband coupling is relatively weak here because the coupling coefficient of one of the sidebands with the principal mode to excite the other sideband is proportional to the product of $(k_0\rho)^2 \ll 1$ and $(v_0/c)^2 =(eE_z/\gamma m\omega_0 c)^2 \ll 1$. The proportionality to $(k_0\rho)^2$ derives from the small-argument expansion of $J_1(k_0\rho)^2$, and the proportionality to $(v_0/c)^2$ is due to the product of $v_z^{(0)}$ in the principal wave and the perturbed displacement in the nonlinear current. We expect that the sideband instability for the extraordinary wave nearly perpendicularly incident at the second harmonic is similarly weak for the following reasons. The perturbed Hamiltonian Eq. (2.10) is again proportional to $J_1(k_\perp\rho)$. The dispersion relation for the X mode at $\omega_0 \approx 2\Omega_e$ is dominantly electromagnetic; thus, the wave equations for the sidebands require the perturbed currents $j_x^{(1)}$ and $j_y^{(1)}$, which depend on the products of $v_x^{(0)}$ and $v_y^{(0)}$, respectively, with the perturbed displacement in analogy with the O-mode case. Thus, it is concluded that an electromagnetic sideband instability exists; but it is a weak instability for physical conditions similar to the FEL heating experiments in MTX.

A one-dimensional electromagnetic particle simulation of the sideband instability of a monochromatic ordinary mode with frequency $\omega \approx \Omega_e$ was reported by Cohen and Cohen (1988b). The initial-value simulation exhibited significant wave attenuation of the ordinary mode due to electron trapping and deformation of the electron distribution, and very weak growth of the sidebands predicted theoretically to be weakly unstable. The attenuation of the ordinary wave and the time dependence of its amplitude preclude quantitative comparison with the analytical theory, which assumes a constant amplitude for the main wave.

C. Nonlinear self-focusing

One of the parametric instabilities described by Eq. (4.1) is ponderomotive filamentation. Porkolab and Cohen (1988) calculated the linear convective growth lengths for the coupling of an incident ordinary-mode plane wave to linearly unstable, infinitesimal-amplitude, ordinary-mode sidebands. This is an example of the linear ponderomotive filamentation instability. For MTX parameters, Porkolab and Cohen (1988) determined that the linear convective growth length for filamentation is comparable to the minor radius of the tokamak. However, a more realistic calculation of filamentation or self-focusing models the incident ordinary wave as having finite lateral extent, which corresponds to a nonlinear modulation of the principal wave by finite-amplitude sidebands and allows for the possible nonlinear self-focusing of the incident wave. Analytical and numerical calculations of nonlinear self-focusing for ordinary-mode FEL heating in MTX suggest that there may be appreciable nonlinear ponderomotive self-focusing in proposed high-power experiments (Cardinali *et al.*, 1988; Cohen, Cohen, Nevins, *et al.*, 1988; Lontano *et al.*, 1989; Cohen *et al.*, 1991).

The analysis of nonlinear self-focusing begins with the wave equation derived from Maxwell's equations:

$$\frac{1}{c^2}\frac{\partial^2 \mathbf{E}}{\partial t^2}+\nabla(\nabla\cdot\mathbf{E})-\nabla^2\mathbf{E}+\frac{4\pi}{c^2}\frac{\partial \mathbf{J}}{\partial t}=0 . \tag{4.3}$$

For ordinary modes incident nearly perpendicular to an applied magnetic field, or for an unmagnetized plasma, a fluid model for the high-frequency plasma current carried by the electrons gives (Kaw *et al.*, 1973; Max, 1976; Cardinali *et al.*, 1988)

$$\frac{\partial \mathbf{J}}{\partial t}=\frac{n_e e^2 \mathbf{E}}{m_e} . \tag{4.4}$$

For finite $k_{\parallel}v_e$ and $k_{\parallel}v_{\parallel}$, the quasisteady magnetized plasma response to the ponderomotive force produced by the high-frequency electromagnetic waves is (Max, 1976; Cohen, Cohen, Nevins, *et al.*, 1988; Cohen *et al.*, 1990)

$$n_e=Z_i n_i=n_0\exp[-e^2\langle E^2\rangle/2m_e\omega_0^2(T_e+T_i/Z_i)] . \tag{4.5}$$

For laser amplitudes satisfying

$$v_0/c<O(2)(\omega_0/\omega_{pe})(m_e/m_i)^{1/2} , \tag{4.6}$$

ponderomotive self-focusing is dominant over relativistic self-focusing and modulational instability (Max *et al.*, 1974), and the laser is stable to relativistic self-focusing for powers P satisfying (Schmidt and Horton, 1985)

$$P<\tfrac{9}{2}(\omega_0/\omega_{pe})^2\times 10^9 \text{ W} . \tag{4.7}$$

Max (1976) used Eqs. (4.3)–(4.5) to derive a threshold power condition for steady-state, self-trapped filaments induced by the ponderomotive force:

$$P>P_0(1-n_e/n_c)^{1/2}(n_c/n_e) , \tag{4.8}$$

where $P_0=m_e c^3(T_e+T_i/Z_i)/e^2=17$ MW (T_e+T_i/Z_i) (keV) and n_c is the critical density where the plasma and laser frequencies are equal. Proposed high-power FEL experiments in tokamaks satisfy all of the inequalities (4.6)–(4.8).

Cohen, Cohen, Nevins *et al.* (1988) adopted the analysis of Max (1976) to study steady-state self-focusing. By neglecting $\nabla(\nabla\cdot)$ and introducing both an eikonal representation and the paraxial assumption that $\partial^2/\partial z^2$ is small compared to $k_0(\partial/\partial z)$ and $\nabla_\perp^2$ operating on the slowly varying wave amplitude, a simplified wave-envelope equation was derived. With the additional assumptions that the wave envelope is cylindrically symmetric, varies radially as a Gaussian, and remains Gaussian, the self-focusing calculation was reduced to a quadrature. The relative beam radius as a function of the penetration distance into the plasma was calculated by Cohen, Cohen, Nevins, *et al.* (1988) for MTX parameters. For a simple slab density and profile, and a laser beam composed of parallel rays at incidence, self-focusing occurs very close to the magnetic axis for $v_0^2/4v_e^2(1+T_i/T_e)=0.03$, $T_i=T_e=1$ keV, $Z_i=1$, and $\omega_{pe}^2/\omega_0^2=\frac{1}{2}$. Introducing an angular divergence into the laser beam or Gaussian profiles for the plasma density and temperature forces the self-focusing to occur at a greater distance into the plasma.

The work of Cardinali *et al.* (1988) and Lontano *et al.* (1989) addressed the space-time dynamics of ponderomotive self-focusing. This is relevant because the current induction-linac driven FEL technology involves finite-length pulses (30–50 nsec) in MTX. Cardinali and coworkers incorporated a hydrodynamic description of the plasma ion response retaining ion inertia and invoked quasineutrality to determine the electron density. They then applied both a self-similar analysis and numerical integration to Eqs. (4.3) and (4.4), and evaluated both steady-state and space-time solutions for the location of the first focus in the plasma assuming either strongly or weakly magnetized ions. For uniform slab density and temperature profiles, and with parallel electromagnetic rays incident and no cyclotron absorption, Cardinali *et al.* calculated that a first focus would appear in a distance less than 30 cm (twice the minor radius of MTX) after 10–20 nsec for high-power operation $P\sim 8$ GW and $T_i=T_e=1$ keV.

A different approach to the space-time dynamics of ponderomotive self-focusing was given in Cohen *et al.* (1991). In this paper both steady-state and time-dependent, paraxial solutions of Eqs. (4.3)–(4.5) were obtained by numerical integration. The wave envelope was not required to remain Gaussian. Computed steady-state flux contours (the flux is defined as $\int dr\, r|E|^2$) are shown in Fig. 13. If the beam had retained its Gaussian shape, the contours would have remained equally spaced. Without the Gaussian assumption, intense beams focus in shorter distances; and rings of increased intensity develop downstream of the first focus. The time-dependent calculations of Cohen *et al.* (1991) retain time derivatives in the wave equation (4.3), while assuming that the hydrostatic plasma response in Eq. (4.5) is valid. This assumption is valid in a magnetized plasma if the self-focusing time is longer than the ion and electron transit times across the laser beam parallel to the applied magnetic field and if $k^2\lambda_s^2 \ll \Omega_s^2/\omega_{ps}^2$ for each species, where λ_s is the ion or electron Debye length. The second condition is satisfied if the Larmor radius of each species is smaller than the laser beam width. The first condition depends on the self-focusing rate and is more difficult to satisfy in physical applications of interest.

Cohen *et al.* (1991) reduced Eqs. (4.3)–(4.5) to the scaled dimensionless nonlinear wave equation

$$\left[\frac{\partial}{\partial T}+\frac{\partial}{\partial Z}+\frac{\partial}{\partial Z}\ln k_0^{1/2}\right]E = \frac{i}{2}\left\{\frac{1}{R}\frac{\partial}{\partial R}\left[\frac{R\,\partial E}{\partial R}\right]+fE\left[1-\exp\left[-\frac{|E|^2}{g}\right]\right]\right\} \tag{4.9}$$

with the scaling transformations $dT=\hat{\omega}_{p0}^2 dt/\omega_0$, $dZ=\hat{\omega}_{p0}^2 dz/\omega_0 v_g(z)$, $dR=\hat{\omega}_{p0}dr/c$, and $E=(e/m_e\omega_0)\tilde{E}(\mathbf{x},t)/2v_{e0}(1+T_{i0}/Z_iT_{e0})^{1/2}$, where $v_{e0}^2=T_{e0}/m_e$ and the unperturbed equilibrium density and temperature profiles were allowed to vary in z (the propagation direction of the incident wave): $\hat{\omega}_{pe}^2(z)=\hat{\omega}_{p0}^2 f(z)$, $T_e(z)=T_{e0}g(z)$, and $T_i(z)=T_{e0}g(z)$. The scaling transformations collect the important parameter dependences in compact form and allow the application of the solutions of the scaled equation to an infinite number of different physical systems. The boundary condition $E(Z=0, R, T)$ describing the incident pulse was defined, and the radial boundary was set at a large enough R compared to the beam radius so that $E=0$. The Z-vs-T trajectories of the first focus were computed for various values of v_0/v_{e0}, which depends on the wave strength and the plasma temperature, the incident beam width a, the angular divergence of the incident beam, and the density and temperature profiles. For decreasing v_0/v_{e0}, increasing $\omega_0 a/c$, increasing angular divergences, and density profiles that decrease faster than do the temperature profiles, the self-focusing occurred at larger values of Z and T, i.e., farther into the plasma and later in time. Other effects that weaken the self-focusing rate are absorption of the laser beam in the plasma [included in some of the steady-state calculations of Cohen *et al.* (1991)] and the scattering of the incident wave in the edge turbulence of the tokamak which increases the angular divergence of the laser.

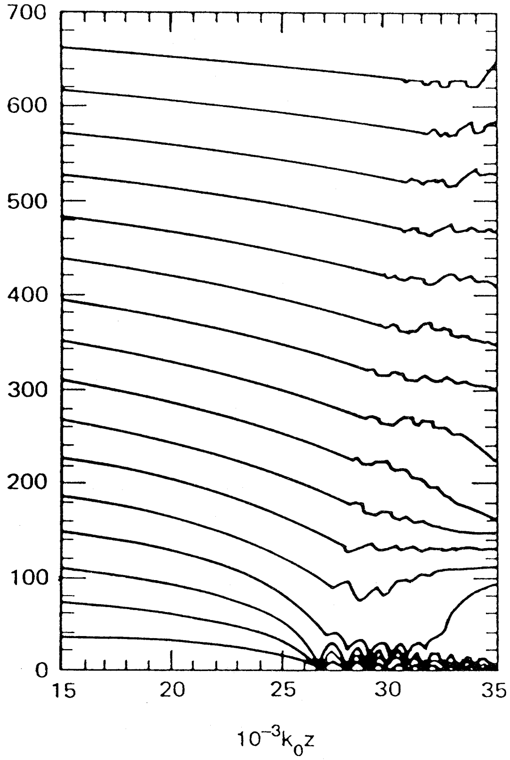

FIG. 13. Steady-state flux contours for an initial Gaussian profile with $v_0/v_e(1+T_i/Z_iT_e)^{1/2}=0.1$, $T_e+T_i/Z_i=10$ keV, and an initial Gaussian half-width $k_0\sigma=700$. If the beam had retained its Gaussian shape, the contours would have remained equally spaced (Cohen *et al.*, 1990).

The more restrictive condition on the validity of the hydrostatic assumption Eq. (4.5) was found to obey the following scaling. The self-focusing time scaled as $T_{\mathrm{sf}}\approx 500(v_{e0}/v_0)$ for $\omega_0 a/c \gtrsim O(10^2)$. With $v_i \approx 10^6$ (cm/sec)$[T_i\ (\mathrm{eV})]^{1/2}$ in hydrogen, the critical temperature above which the hydrostatic assumption is valid (provided that $\rho_i < a$) is then

$$T_i \geq (3.6\ \mathrm{keV})(n_e/n_c)^2(\omega_0 a/c)^2(v_0/v_{e0})^2\ .$$

Thus, for $(n_e/n_c)(v_0/v_{e0}) \leq 10^{-2}$ and $100 \leq \omega_0 a/c \leq 200$, $T_i \geq 5-10$ keV is required for the validity of the hydrostatic assumption. This condition can be satisfied for possible FEL applications in current large tokamaks like the Joint European Torus (JET) and the Tokamak Fusion Test Reactor (TFTR), and future tokamaks like CIT and ITER. The validity condition for the hydrostatic assumption is not satisfied for MTX applications at high power: Cohen *et al.* (1991) calculate a self-focusing time of 3–5 nsec for $(v_0/v_{e0})^2=0.24$, $\hat{\omega}_{p0}^2/\omega_0^2=0.5$, and $\omega_0/2\pi=140$ GHz anticipated in MTX where the ion transit time across the laser beam is approximately 30 nsec. Nevertheless, by ignoring ion dynamics, the calculation based on the hydrostatic assumption remains useful because it is pessimistic compared to the calculations of Cardinali *et al.* (1988) and Lontano *et al.* (1989), i.e., it overestimates the self-focusing rate. Thus, when these calculations determine that the self-focusing occurs in a time longer than the given pulse length or in a distance greater than the width of the plasma, one expects that self-focusing will not occur when ion dynamics are included. However, an important caveat is that the model calculation of Limpouch *et al.* (1988) including ion dynamics indicated that if the laser pulse is initiated abruptly, there can be transient oscillations in which self-focusing exceeds its steady-state amplitude.

D. Stability of the heated plasma

High-power microwave pulses from an FEL injected into a tokamak for heating and current drive can produce spatially localized distortions of the electron velocity distribution function that are severe. The heating and the distortion of the electron distribution alter the electron cyclotron emission of the plasma (Farina and Pozzoli, 1988) and can excite microinstabilities (Matsuda and Smith, 1990). The enhanced wave turbulence accompanying microinstability can degrade particle and energy confinement in the tokamak. Matsuda and Smith (1990) have begun a study of the microstability of FEL-heated electron distributions using a recently developed code that solves the fully relativistic dispersion relation for a uniform plasma with an arbitrary distribution function. The distribution function can be given by an analytical model or numerically defined on a velocity or momentum grid as output from a code that calculates particle orbits. With the distribution function defined, a relativistic conductivity tensor is computed; and a linear dispersion relation for electromagnetic normal modes is then calculated. Solution for the unstable roots of the electromagnetic dispersion relation leads to the construction of a stability diagram. The modes of most interest are near the electron cyclotron frequency: the whistler (driven by temperature anisotropy $T_{\perp e} > T_{\parallel e}$: Sudan, 1963), upper hybrid loss-cone (driven by a loss-cone electron velocity distribution; Ashour-Abdalla and Kennel, 1987), and cyclotron maser (relativistic, loss-cone driven: Wu and Lee, 1979; Lau and Chu, 1983) instabilities.

The linear dispersion relation that is solved in the code by Matsuda and Smith is

$$\det|\mathbf{n}\times(\mathbf{n}\times\mathbf{E})+\mathbf{K}\cdot\mathbf{E}|=0\ , \tag{4.10}$$

where $\mathbf{K}=\mathbf{I}+(4\pi i/\omega)\sum_j \boldsymbol{\sigma}_j$, $\mathbf{n}=c\mathbf{k}/\omega$, and $\boldsymbol{\sigma}_j$ is the complex conductivity tensor for a uniform plasma with an applied magnetic field. Integrals over the velocity distribution to evaluate $\boldsymbol{\sigma}_j$ are performed numerically using a Gauss quadrature, and special measures are introduced to resolve resonances carefully (Matsuda and Smith, 1990). Orbit calculations (Rognlien and Nevins, 1987) indicate that strongly heated electron hot electron distributions produced by FEL heating are highly non-Maxwellian and often have both a local minimum with respect to the perpendicular energy and a loss-cone. Matsuda and Smith devised a procedure using spline fits and digital filtering to approximate the numerical distribution functions obtained from the orbit code (Fig. 14). After checking their microstability code results against

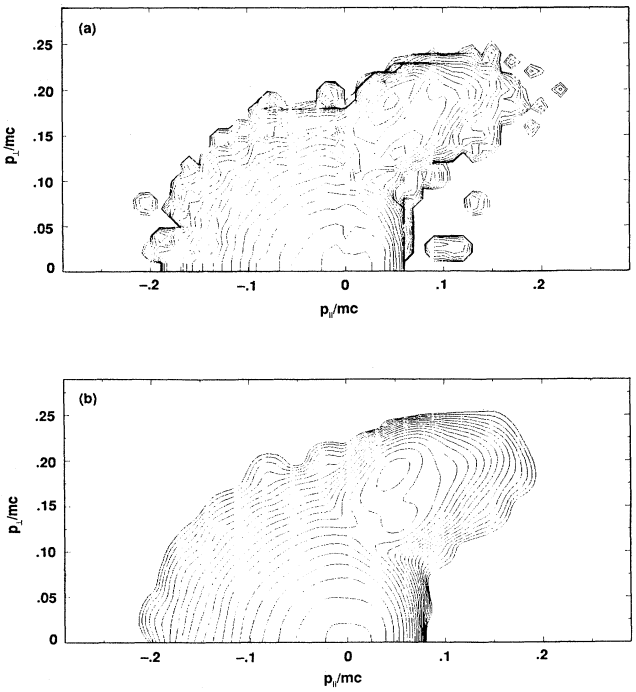

FIG. 14. Contour plots of an FEL-heated electron distribution function in momentum space from (a) an orbit code and (b) as filtered and fitted with splines for use in a microstability code (Matsuda and Smith, 1990).

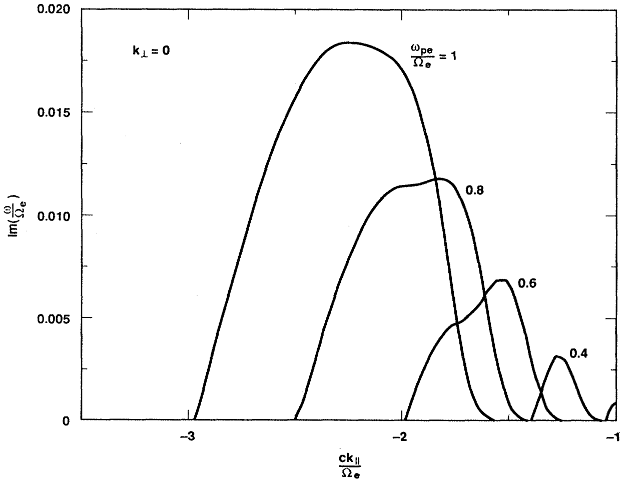

FIG. 15. Whistler instability growth rates as a function of $k_\parallel$ for various values of ω_{pe}/Ω_e and with $k_\perp=0$ (Matsuda and Smith, 1990).

the results of several published papers, they applied the code to an MTX case with 2 GW of power at 140 GHz, a beam cross-section of 6 cm × 8 cm, a toroidal field of 5 T, and a density of 1.8×10^{14} cm^{-3}. Preliminary results indicate that both the whistler and upper hybrid loss-cone modes are unstable with growth rates $\mathrm{Im}\omega/\Omega_e=(5-7)\times10^{-3}$ for $\omega_{pe}/\Omega_e=0.6$. Growth rates for the whistler instability for $k_\perp=0$ are plotted in Fig. 15. These growth rates are rapid compared to the inverse of typical pulse durations, and, hence, of concern, particularly for current-drive applications. However, finite-geometry effects, such as convective stabilization, have not yet been evaluated but are under investigation. Additionally, study of the cyclotron maser instability is in progress; and calculations indicate instability with $\mathrm{Re}\,\omega/\Omega_e\approx0.99$ and $\mathrm{Im}\,\omega/\Omega_e\approx3.6\times10^{-3}$ for $\omega_{pe}/\Omega_e=0.6$, and this growth rate has been maximized with respect to $k_\perp$ and $k_\parallel$ ($k_\parallel \ll k_\perp$).

V. SIMULATIONS OF FEL HEATING AND CURRENT DRIVE

A. Monte Carlo and self-consistent particle simulations

In this section we present a few examples of computer simulations of FEL heating and current drive. Analytical progress in describing aspects of the highly nonlinear interaction of an intense, pulsed electron cyclotron wave with a plasma is limited and subject to restrictive approximations. In order to test the approximate analytical calculations and obtain a more comprehensive picture of the phenomena that is subject to fewer assumptions and is closer to first principles, numerical simulations have been undertaken (Rognlien and Nevins, 1987; Nevins *et al.*, 1987; Cohen, Cohen, Nevins, *et al.*, 1988; Cohen, Cohen, Logan, *et al.*, 1988; Menyuk *et al.*, 1987, 1988; Akimoto and Karimabadi, 1989). The numerical simulations should be viewed as computational experiments that provide qualitative and quantitative insight into the FEL heating and current-drive phenomena.

The two most heavily used simulation methods for the study of the nonlinear aspects of FEL heating and current drive are orbit-following codes (so-called Monte Carlo codes) and self-consistent electromagnetic particle simulation codes. The orbit-following codes take the relativistic equations of motion for charged particles in prescribed electromagnetic fields and integrate the trajectories of an ensemble of test particles representing an initially Maxwellian distribution (Rognlien, 1983b). The equations of motion are a set of ordinary differential equations requiring a simple set of initial conditions for their solution. When collisional effects need to be included, a Monte Carlo scattering scheme has been adopted in which the test particles scatter on a background plasma with a prescribed density and velocity distribution (Rognlien, 1983a). Much of the physics of FEL heating and current drive separates cleanly into collisionless and collisional regimes because of the separation of time scales between the relatively fast electron transit times and the slow collisional time scale. The integration schemes used in the orbit-following codes may be the simple second-order-accurate schemes favored for self-consistent particle simulations (Hockney and Eastwood, 1981; Birdsall and Langdon, 1985), because these are readily optimized for efficient computer solution, or higher-order-accurate integration schemes where accurate integration through a resonance or turning point is desired (Ruth, 1983, Keefe, 1986).

The self-consistent electromagnetic particle simulations also integrate the relativistic particle equations of motion (Birdsall and Langdon, 1985). However, these codes additionally solve Maxwell's equation for the self-consistent electric and magnetic fields. To accomplish this, the charge and current densities for the particles are accumulated on a spatial grid by interpolation from the particle locations. These charge and current densities provide the sources in Maxwell's equations which determine the electromagnetic fields on the grid. Maxwell's equations are a set of partial differential equations that are solved on a spatial grid by fast Fourier transform or by finite-differencing and matrix inversion. The fields are interpolated from the grid back to the particle locations to accelerate the particles. In addition to the constraints on the particle-trajectory calculations, the self-consistent simulation must also accurately and stably resolve the propagation of the electromagnetic normal modes supported by its physics model. This leads to a set of constraints on the integration time step and the spacing of the spatial mesh. Furthermore, because the discrete particles emit and absorb electromagnetic waves in a self-consistent simulation, there are thermal fluctuations contributing to an electromagnetic noise level that leads to requirements on the number of particles to accurately resolve linear and nonlinear phenomena (Birdsall and Langdon, 1985). As the size of the simulation problem increases in terms of a characteristic wavelength, the Debye length, Larmor radius, or skin depth, the self-consistent simulation requires more grid points and more particles, and the cost of the computation rises concomitantly.

In what follows in this section, we shall review example calculations performed with orbit-following and self-consistent particle simulation codes addressing several aspects of FEL heating and current drive. First we describe simulations of nonlinear electron cyclotron heating in which electron trapping is important. This is followed with simulations of heating and current drive in which stochasticity or the rising-bucket mechanism is important. Beat-wave current drive is illustrated next. The section is concluded with examples of simulations of stimulated Brillouin backscatter and filamentation.

B. Nonlinear electron cyclotron heating

The theory of the resonant nonlinear wave-particle interaction for intense, pulsed electron cyclotron heating was reviewed in Sec. II. Owing to the finite transit time of an electron crossing the width of the beam parallel to the magnetic field for an electron cyclotron wave propagating across the magnetic field, resonant electrons are trapped and then detrapped nonadiabatically. Analytical calculations indicate that the detrapped electrons have a 50% probability of being accelerated to higher energy for first and second harmonic heating. The fraction of trapped electrons depends explicitly on the wave amplitude. At high wave amplitudes as described in Sec. II, the opacity of the plasma depends on the wave amplitude. In the absence of gradients in either the parallel wave number or the magnetic field that lead to rising-bucket enhancements of the opacity, the opacity is reduced from its linear value by nonlinear effects. The nonlinear absorption of intense, pulsed electron cyclotron waves has been studied with both orbit-following and self-consistent particle simulation codes (Nevins *et al.*, 1987).

Rognlien and Nevins (1987) used an orbit-following code to study the nonlinear absorption of an ordinary mode with frequency near the first harmonic that is incident nearly perpendicular to the magnetic field. Initial ensembles of Maxwellian test particles were launched on a flux surface near the cyclotron resonance. The absorbed power as a function of the incident field strength deduced from the orbit code is plotted in Fig. 16. Linear theory predicts that the absorbed power should increase as $\tilde{E}_{\parallel}^2$. The data points (crosses) for a uniform applied magnetic field and $k_{\parallel}=0$ show reasonable agreement with the theoretical prediction for the strongly nonlinear regime, for which the absorption is proportional to $\tilde{E}_{\parallel}^{4/3}$. The simulation data determines the overall multiplicative factor that the scaling arguments of Sec. II cannot set (Nevins *et al.*, 1987). In the subsequent work of Kotel'nikov and Stupakov (1990), the multiplicative factor $A \approx 1$ was calculated for the strongly nonlinear opacity of the ordinary mode which fits the data in Fig. 16 at the largest field amplitudes. In the numerical calculations reported by Nevins *et al.* (1987), a value of $A=1.6$ was used as an overall fit to the numerical results. The increased absorption observed in the orbit code for finite $dk_{\parallel}/ds$ and dB/ds is caused by rising buckets.

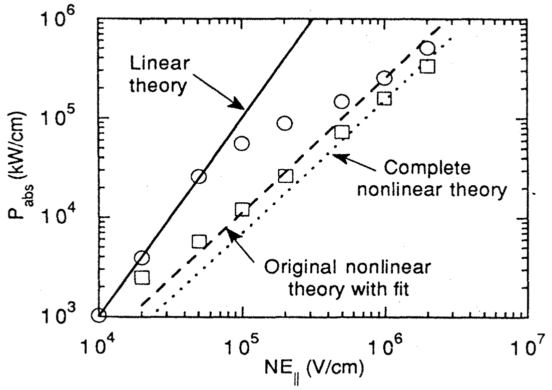

FIG. 16. Power absorbed per unit beam height for the O-mode with $\omega_0/\Omega_0=1$ from an orbit code for two cases: $k_{\parallel}=\partial B_0/\partial s=0$ corresponding to a minor radius of $r=0$ (squares) and for $k_{\parallel}=1.4+0.5(s-s_0)$ cm^{-1} with $\partial B_0/\partial s=3.7\times10^{-3}$ T/cm corresponding to $r=3$ cm in MTX (circles). Parameters are $T_e=1$ keV, $B_0=5$ T, and $n_e=1\times10^{14}$ cm^{-3}. The beam power width along B_0 is $w=3.7$ cm, yielding $p_2=1.3$ (Nevins *et al.*, 1987). The line labeled "complete theory" is from Kotel'nikov and Stupakov (1991).

The two-dimensional, relativistic, electromagnetic particle code ZOHAR (Langdon and Lasinski, 1976) was used to perform self-consistent particle simulations of nonlinear absorption (Nevins *et al.*, 1987; B. Cohen, 1987b). This model was used to simulate wave propagation across a prescribed plasma profile and includes wave attenuation on multiple flux surfaces in a natural way. Wave attenuation was omitted from the orbit-following code and was not included in the opacity estimates given in Sec. II.B. An ordinary mode with finite width in y was incident on a finite plasma slab with density and background magnetic field $B_0\hat{y}$ that varied in x. The boundary conditions were periodic in y and open in x (outgoing boundary conditions on particles and radiation).

The predictions of the scaling theory of Sec. II were compared to the particle simulation results, noting that the width of the plasma slab in the simulation was comparable to the width of the linear absorption layer. This reduced the opacity in all absorption regimes (by factors of 2 or 3). The value of τ_L given in (2.24) was reduced from $\tau_L=10$ to $\tau_L=3$ for the smallest resonance zone and to $\tau_L=5$ for a set of simulations with a wider resonance zone. The limited resonance zone alters the scaling arguments for the opacity. The range of wave intensities varied over $0\le\tilde{E}_{\parallel}/B_0\le0.4$ corresponding to $0\le p_1\le2.66$. Recall that $p_1=[N_{\perp}(E_{\parallel}/B_0)(m_ec^2/T_e)]^{2/3}$ for the ordinary mode. From the relative temperature of the plasma, $T_e/m_ec^2=0.09$ and the width of the incident beam along $\mathbf{B}_0$, $w=50k_0^{-1}$, $p_2=0.4$, where p_1 and p_2 were defined in Eq. (2.19). The first nonlinear regime corresponded to $1\ge p_1\ge p_2^{4/3}$, which was $1\ge p_1\ge0.3$ for these parameters. The absorption layer width d_L was replaced by a shorter distance d in these simulations, but the relative scaling of the opacity in the first nonlinear regime was unchanged from $\tau_{\mathrm{NL}1}\approx\tau_l(p_2/p_1^{3/4})$ given in Eq. (2.30). In the second nonlinear regime $p_1>1$. The absorption layer width was shortened from p_1d_l to d, and the average energy absorbed was reduced by an additional factor of p_1 because of the reduced layer width (Nevins *et al.*, 1987). Thus, the scaling of the opacity in the second nonlinear regime was predicted to be $\tau_{\mathrm{NL}2}\approx\tau_{\mathrm{L}}(p_2/p_1^3)$.

Results from self-consistent simulations are shown in Figs. 17 and 18. Figure 17 shows contours of the time-dependent electromagnetic field $B_z(x,y)$ for a simulation of a perpendicularly incident ordinary mode with $B_{\mathrm{rf}}/B_0=0.1$ and frequency that is resonant with the fundamental cyclotron harmonic at $x=30$ in the interior of the plasma. The background magnetic field varied linearly, $0.85\le\Omega_e/\omega_0\le1.35$. There was 75% absorption

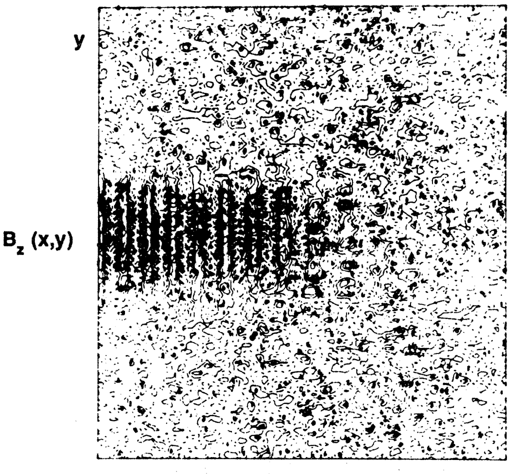

FIG. 17. Contours of magnetic field amplitude $B_z(x,y)$ in the x,y plane for a particle simulation of ordinary mode heating at perpendicular incidence and at the fundamental electron cyclotron harmonic showing good absorption.

of the ordinary mode in the simulation. The definition of τ in Fig. 18 is $\tau = -\ln$ (transmitted power/incident power), which is plotted as a function of p_1. Data for narrow (circles) and wider (triangles and x) resonance zones are shown. Increased absorption occurred for the wider resonance zone. The simulations were performed with 96 000 electrons and ions with a mass ratio of $m_i/m_e = 10$ and $T_i = T_e$ when mobile ions were included. The x-y mesh was 100×128; $\omega_{pe}^2/\omega_0^2 = 0.5$ at the peak of the electron density profile; and 3000 time steps were used with $\omega_0 t = 0.2$. The system size was $L_y = 120 k_0^{-1}$ and $L_x = 80 k_0^{-1}$ or $100 k_0^{-1}$. The data from the simulations agree reasonably well with the modified scaling arguments. At very low wave intensities, there is strong linear absorption $\tau > 4$, and the weak transmitted signal is difficult to measure with precision because of the competition with thermal noise. At high intensities, the observed absorption was improved over the expectation of the scaling theory. One possible mechanism that could contribute to the enhanced absorption is the resonant parametric decay of the ordinary mode into two magnetized plasma waves that is mentioned in Sec. IV.A. With the inclusion of ions in the simulations, the enhancement of the absorption was not as large for increasing wave intensity. There was evidence of nonlinear self-focusing in these simulations with mobile ions, which became more pronounced with increasing incident wave intensity. Nonlinear self-focusing depletes the local plasma density and raises the local value of the wave intensity. These two effects reduce the wave absorption and increase the transmission, while the narrowing of the laser beam reduces the correlation time τ_c, increases p_2, and tends to increase the absorption.

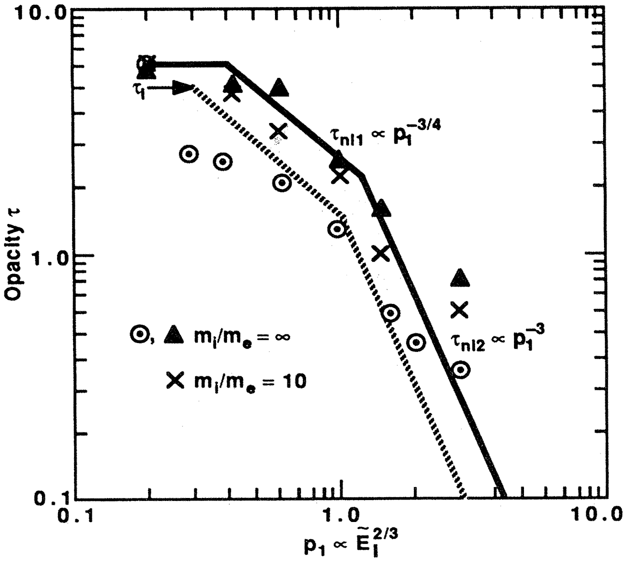

FIG. 18. Particle simulation results for the opacity as a function of $p_1 \propto \tilde{E}_\parallel^{2/3}$ for ordinary mode heating at perpendicular incidence and at the fundamental cyclotron harmonic (Nevins *et al.*, 1987). The curves indicate the predictions of scaling arguments as modified for the restricted spatial domain of the simulations.

C. Stochastic heating and current drive

The threshold condition for the wave amplitude required to induce resonance overlap and stochasticity was given in Sec. II. How stochasticity can be used as a heating and current-drive mechanism was also reviewed in Sec. II. We presented results from Rognlien and Nevins (1987) for the stochasticity threshold values of the wave electric field as a function of the wave frequency for the use of finite-width extraordinary and ordinary modes in MTX. There have been several other numerical studies of the onset of stochastic electron motion in the presence of a uniform electron cyclotron wave, for example, Menyuk *et al.* (1987, 1988), Hizanidis (1989), Karimabadi *et al.* (1990), and Akimoto and Karimabadi (1989). The calculations of Akimoto and Karimabadi (1989) were based on self-consistent particle simulations, while the rest were based on orbit-following codes. Stochastic current-drive efficiency calculations were reviewed in Sec. III. These calculations were produced with an orbit-following code (Rognlien and Nevins, 1987) omitting ponderomotive effects from the finite microwave beam profile. The calculation of the efficiency included effects of both collisional relaxation and magnetically trapped particles.

Figures 19, 20, and 21 further illustrate stochastic heating and current drive. These results are taken again from Rognlien and Nevins (1987). The surface of section plots in Fig. 19 show the transition from regular to stochastic motion for a right circularly polarized extraordinary wave with $\omega_0/\Omega_e^{(0)} = 1.96$, $k_\parallel = 0, E_{\rm rf}/B_0 = 0.02$ and

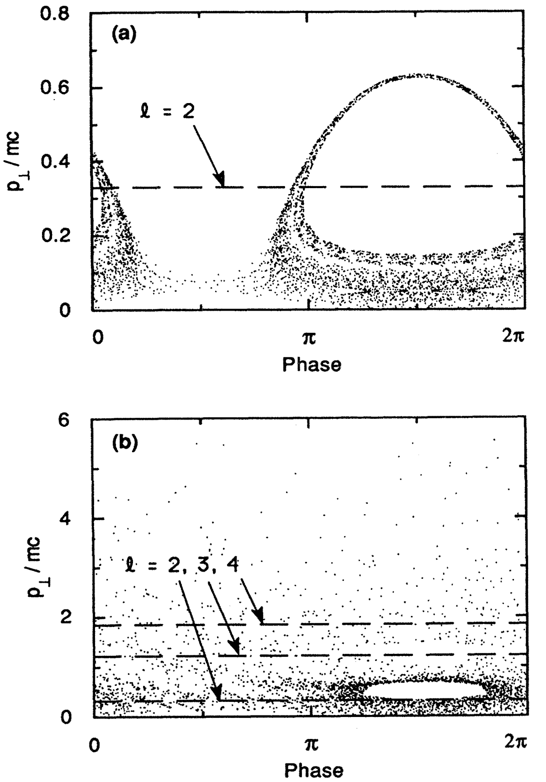

FIG. 19. Surface of section plots in the $P_\perp,\theta$ plane showing the transition to chaos for a right circularly polarized extraordinary wave with $\omega_0/\Omega_0=1.9$, $k_\parallel=0$, initial energies $\varepsilon_\perp=\varepsilon_\parallel=1$ keV, and (a) $E_c/B_0=0.0463$ and (b) $E_c/B_0=0.093$. The lines denoted by different l's give the cyclotron resonances for small wave amplitude.

0.2, and 1 keV electrons. The extraordinary wave was an infinite plane wave. Plotted in Fig. 20 are the results of orbit calculations for the initial and final momenta resulting from acceleration by an extraordinary wave with frequency $\omega_0/\Omega_e^{(O)}=1.9$ and well above the stochastic threshold for two different angles of propagation with respect to the magnetic field. These trajectories follow the heating characteristics calculated in Eq. (2.15). The stochastic threshold electric field amplitude for a right circularly polarized extraordinary mode with frequency $\omega_0/\Omega_e^{(O)}=1.9$ is plotted in Fig. 21 as a function of the propagation angle with respect to the magnetic field. When above threshold for stochasticity, the current-drive efficiency increases with increasing $k_\parallel/k$, but the threshold electric field increases also.

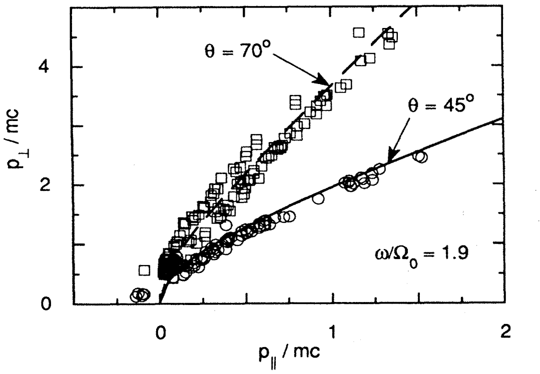

FIG. 20. Final positions in the $p_\perp/mc,p_\parallel/mc$ plane of electrons from an initial 1 keV Maxwellian after they pass through a 0.71 cm wide rf beam in the stochastic regime with $E_c/B_0=0.15$ and $\omega_0/\Omega_0=1.9$. Results for the extraordinary mode at two angles of propagation (70° and 45°) with respect to **B** are shown.

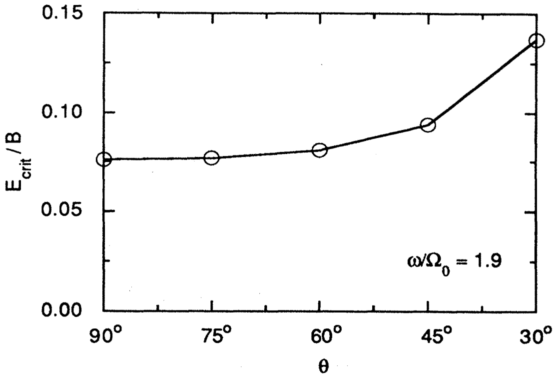

FIG. 21. The stochasticity threshold electric field strength E_c/B_0 for the right circularly polarized component of the extraordinary wave at frequency $\omega_0=1.9\Omega_0$ as a function of the angle between **k** and $\mathbf{B}_0$.

D. Rising buckets

The theory of electron cyclotron heating exploiting rising buckets was reviewed in Sec. II.B. Examples of the current-drive efficiency for rising-buckets were presented in Sec. III.C. Rising-bucket calculations have been made with both an orbit-following code (Cohen and Rognlien, 1991) and a self-consistent electromagnetic particle simulation (Cohen and Rognlien, 1989). We first describe selected results from orbit calculations.

Figure 16 shows simulation data form Nevins *et al.* (1987) for the absorbed power as a function of the electric field strength for a perpendicularly incident ordinary mode for both $k_\parallel=\partial B_0/\partial s=0$ on the magnetic axis and $k_\parallel=1.4+0.5(s-s_0)$ cm^{-1} with $\partial B_0/\partial s=3.7\times10^{-3}$ T/cm corresponding to $r=3$ cm in MTX. The other important parameters for the simulations were $T_e=1$ keV, $B_0=5$ T, $n_e=1\times10^{14}$ cm^{-3}, and a beam width along $\mathbf{B}_0$ of $w=3.7$ cm, which yielded $p_2=1.3$. The gradients in B_0 and $k_\parallel$, and the finite beam width facilitated rising-bucket acceleration, which led to the increased absorption noted in Fig. 16. Representative electron trajectories illustrating the difference between rising buckets and the nonlinear heating for $k_\parallel=0$ described in Nevins *et al.* (1987) are presented in Fig. 22. In the three cases, $dN_\parallel/dz$ was zero, positive, and negative, which corresponded to normal incidence, a diverging beam, and a converging beam. For each case, two electrons with

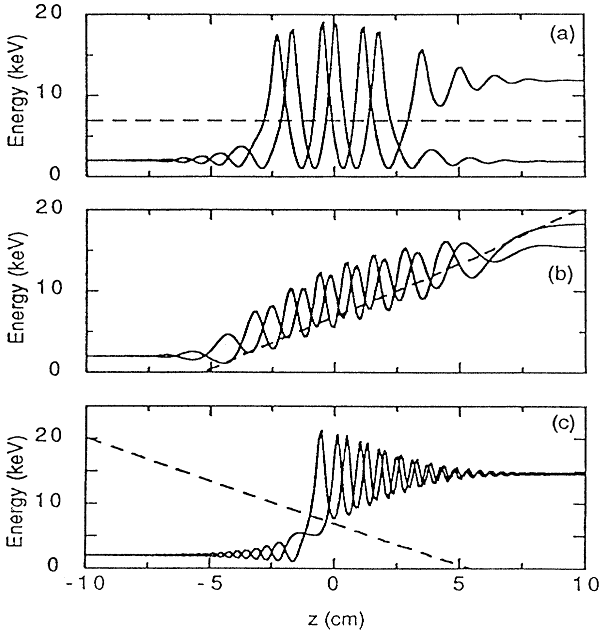

FIG. 22. Electron trajectories calculated with an orbit code illustrating bifurcation, and rising buckets and phase-space displacement. (R. Cohen and Rognlien, 1990). Particle energies as a function of z are plotted for (a) $dN_{\|}/dz=0$, (b) $dN_{\|}/dz>0$, and (c) $dN_{\|}/dz<0$. Two electrons with identical initial energies and differing gyrophases are shown in each plot. The resonant energies are shown as dashed lines.

$\varepsilon_{\perp}=\varepsilon_{\|}=1$ keV and different gyrophases are followed from $z=-10$ cm through a pulse with $\tilde{E}_{\|}=4\times10^5$ V/cm, $B_0=5.07$ T, $f=140$ GHz, and a Gaussian profile with 4 cm width centered at $z=0$. The resonant electron energy is plotted as a dashed line. Figure 22(a) shows the electrons becoming trapped and then detrapped, resulting in one electron being significantly heated and the other returning to its original energy. This illustrates the basic heating mechanism described by Nevins *et al.* (1987). Rising-bucket acceleration is demonstrated in Fig. 22(b) when the resonant energy is made to increase with increasing z. On the other hand, if the resonant energy decreases with z, the bottom of the separatrix (bucket) descends to the electron energy, as in Fig. 22(c); and the electrons are displaced to the top of the separatrix as the result of the strong but brief acceleration. This phase-space displacement mechanism is included within the rising-bucket theory of Cohen and Rognlien (1991). Figure 23 displays the deformation of the electron distribution function after passing through a microwave pulse with $\tilde{E}_{\|}=5\times10^4$ V/cm, $\Delta N_{\|}=0.25$, $B_0=5$ T, a beam width of 10.4 cm, and 1 keV initial temperature. Resonances and heating characteristics deduced from Eq. (2.37) are shown in Fig. 23(b). The results from the orbit calculations establish that with the appropriate spread of $k_{\|}$, the nonlinear opacity can significantly exceed the linear opacity. Figure 24 presents the ratio of the nonlinear opacity to the linear opacity from orbit calculations and analytical theory (Cohen and Rognlien, 1991) for a spread of $N_{\|}$ using parameters similar to those in Figs. 22 and 23.

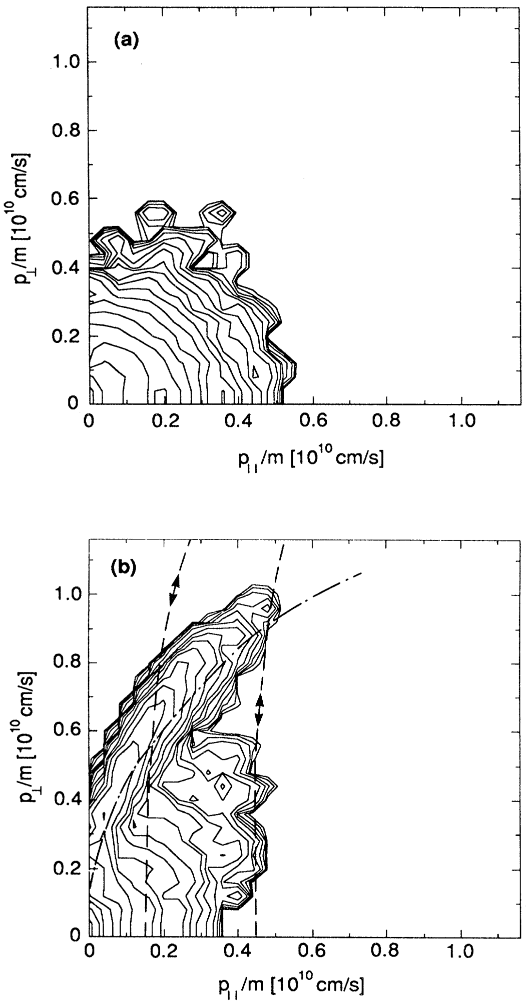

FIG. 23. Contour plots in the $p_{\perp},p_{\|}$ plane from an orbit code showing the electron distribution function (a) before and (b) after passing through an O-mode rf beam with $\omega_0/\Omega_0=1$. Heating characteristics are denoted in (b) as dotted lines, and the resonance at the exit side of the beam at the $1/e$ point of the electric field is indicated with a dot-dashed line. Here, $B_0=5$ T, $\Delta N_{\|}=0.25$, $E_{\|}=5\times10^4$ V/cm, the beam power width was 14.7 cm, and the initial temperature was $T_e=1$ keV.

A set of self-consistent electromagnetic particle simulations with the ZOHAR code (Langdon and Lasinski, 1976) were reported by Cohen and Rognlien (1989), who compared self-consistent simulations of rising-bucket acceleration to simulations performed with an orbit-following code. In the self-consistent simulations, an ordinary mode was launched with a square profile through an aperture that was $20k_0^{-1}$ wide at an angle of 45° with respect to a background magnetic field that varied linearly across the simulation so that $1.34\geq\omega_0/\Omega_e\geq1.08$. The relatively narrow aperture encouraged a beam diver-

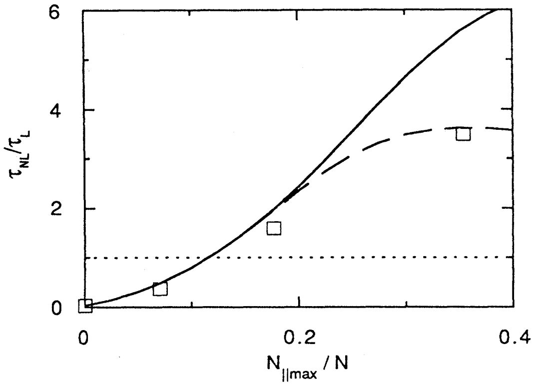

FIG. 24. A plot of the ratio of the nonlinear opacity to the linear opacity $\tau_{\rm NL}/\tau_{\rm L}$ as a function of $N_{\|\max}/N$ as determined by an orbit code and theory for parameters similar to those of Figs. 22 and 23. The dashed curve reflects a small modification of a coefficient in the theory to better fit the numerical particle orbit calculations. Here $N_{\|\max}$ is the value of $N_\|$ at the $1/e$ point of the electric field.

gence so that there was a spread of $N_\|$, $0.5<N_\|<0.95$. The plasma density had a flat-top profile with a maximum density corresponding to $\omega_{pe}/\omega_0=0.185$, and the electron distribution function was represented with 128 000 particles. The ions were a fixed charge-neutralizing background, and the duration of the simulation was $\omega_0 t=600$ with a time step $\omega_0 t=0.2$. The self-consistent simulations included wave attenuation, refraction, diffraction, and scattering due to thermal fluctuations in the electromagnetic fields. In these simulations, the product of the trapping frequency ω_b and the transit time across the beam τ_c satisfied $2\pi\ge\omega_b\tau_c\ge 1$. The condition that the bucket lift was adiabatic, i.e., that the trapping time was shorter than at the time to lift the resonance in energy by the width of the separatrix, was only marginally satisfied.

Results from the orbit-following and the self-consistent particle simulations are shown in Figs. 25 and 26. Conditions in the orbit code were established to mimic the electromagnetic field pattern and the spread of $N_\|$ achieved in the ZOHAR simulations (Fig. 25). The results of two sets of simulations with different wave amplitudes are shown in Fig. 26, $E_{\rm rf}/B_0=0.06$ and 0.24 at the aperture, which translated to $E_{\rm rf}/B_0=0.03$ and 0.13 at the resonance point in the plasma. There was fairly good agreement between the two types of simulations on the heated

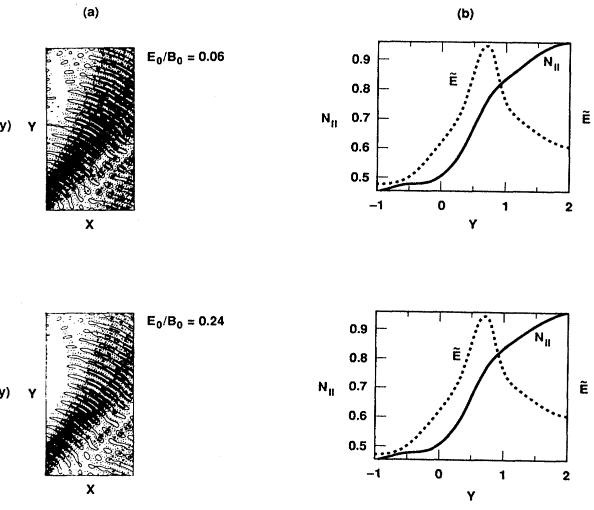

FIG. 25. (a) Contour plots of $E_z(x,y)$ in the x,y plane for a ZOHAR particle simulation of ordinary mode heating and rising buckets with 45° angle of incidence, peak amplitude at the aperture $E_0/B_0=0.06$ and 0.24, and frequency resonant with the fundamental electron cyclotron frequency in the center of the plasma slab. (b) Corresponding plots of the electric field and $N_\|$ on a flux surface in the middle of the plasma versus distance along the magnetic field from an orbit code used to compare to the particle simulation.

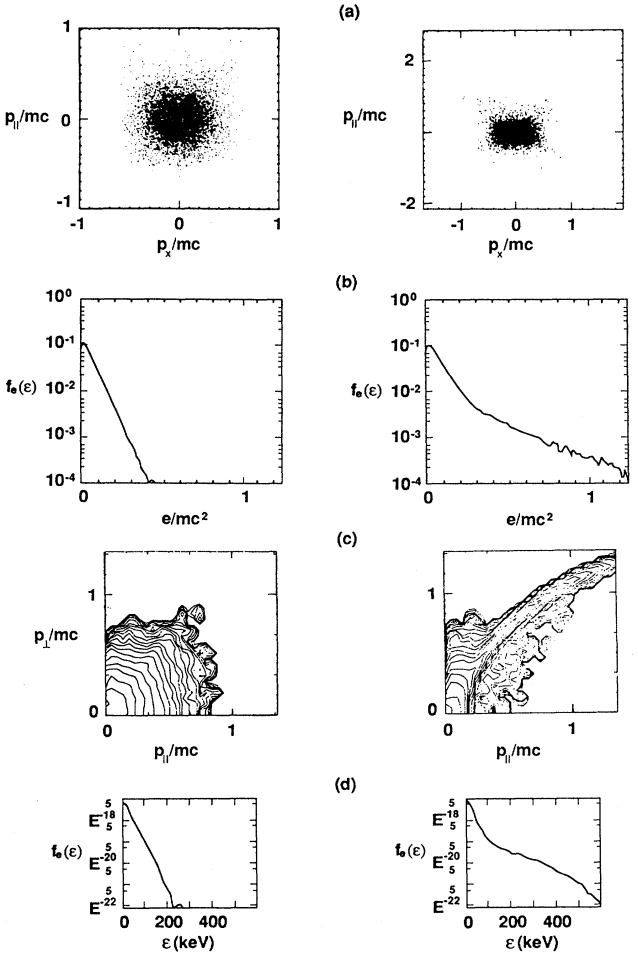

FIG. 26. (a) Scatter plots of the final momenta $p_y=p_\|$ and p_x from ZOHAR simulations of rising buckets for the two electric fields shown in Fig. 25. (b) Electron energy distribution versus energy in the particle simulation. (c) Contour plots in the $p_\perp,p_\|$ plane from the corresponding orbit-code simulation. (d) Electron energy distribution versus energy from the orbit code simulation illustrating rising buckets. The wave amplitudes were below the stochasticity threshold.

electron velocity distributions. Significant heating was observed, with individual particles gaining energies that exceeded their initial energies, $T_e(0)=0.04m_ec^2$: many electrons realized energy gains comparable to the $\Delta\varepsilon\approx 0.5m_ec^2$ predicted for complete bucket rise, Eq. (2.34), for $E_{\rm rf}/B_0\geq 0.1$ at the aperture. After the incident wave was adiabatically turned off in the ZOHAR simulations, the power spectrum for the electrostatic fields did not reveal any superthermal fluctuations nor microinstability; and thermal fluctuations and collisions (enhanced by particle discreteness) relaxed the anisotropies in the electron velocity distribution produced by the heating. Diagnostics of the single-particle orbits in the orbit code indicated that the electrons were trapped and experienced strong single-pass acceleration in the resonant wave field, but that $\omega_b\tau_c\lesssim\pi$ in most cases. The transit time in the particle simulations of rising buckets was short, because the system size was compressed. As a result, not all aspects of rising buckets were faithfully modeled by the self-consistent particle simulations.

E. Beat-wave current drive

The theory of beat-wave current drive was reviewed in Sec. II.B, and self-consistent particle simulation results for the current-drive efficiency were presented in Sec. III.C. Two-dimensional fluid simulations of beat-wave coupling were reported by Amin and Cairns (1990), whose work showed that parallel and antiparallel geometries were preferred. The one-dimensional particle simulations of Cohen, Cohen, Logan *et al.* (1988) using the self-consistent electromagnetic particle code EMONE (Cohen *et al.*, 1975; Birdsall and Langdon, 1985) have given a detailed picture of many nonlinear aspects of beat-wave current drive.

The particle simulations model the beat-wave coupling from first principles and, therefore, incorporate in a natural way the nonlinear transfer of wave action between the electromagnetic waves, electron Landau damping and electron trapping in the longitudinal beat wave, the possible nonlinear coupling of the beat wave to other electrostatic modes in the presence of ions and ion waves, and the possible multiple scattering of the two electromagnetic pump waves. As pointed out in Sec. III.C, an important finding in the simulations was the sensitivity of the beat-wave coupling and the current-drive efficiency to the ratio of the beat-wave phase velocity to the electron thermal speed; values of this ratio in the range of 2 to 4 for wave propagation parallel to the background magnetic field were found to be optimum to achieve good action transfer and current-drive efficiency. The simulations also demonstrated that the momentum transfer to the plasma was in good agreement with the Manley-Rowe relations governing conservation of wave action: Fig. 4 of Cohen, Cohen, Logan *et al.* (1988).

Figure 27 shows simulation results from Cohen, Cohen, Logan *et al.* (1988) for oppositely propagating transverse pump waves, wherein a large-amplitude plasma wave is excited. There is significant heating and tail formation in the electron velocity distribution, and there is nearly complete transfer of wave action from the higher frequency electromagnetic pump wave to lower frequency transverse waves. This simulation and the others reported in Cohen, Cohen, Logan *et al.* (1988) had no

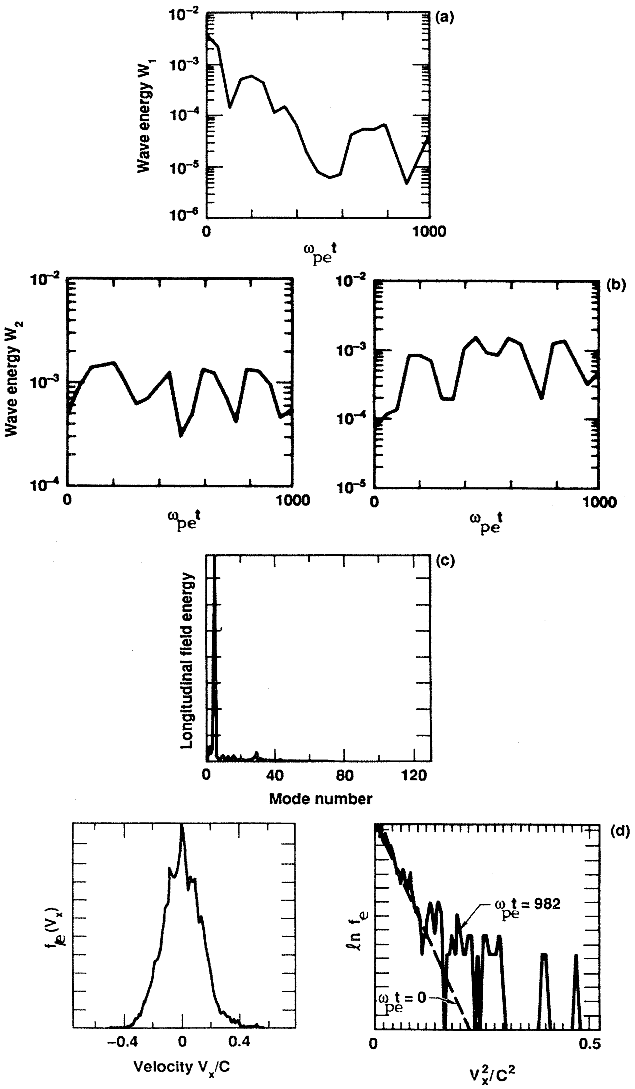

FIG. 27. Particle simulation results (Cohen, Cohen, Logan, *et al.*, 1988) for beat-wave current drive with opposed transverse waves with $\omega_1=2.24\omega_{pe}$, $\omega_2=1.12\omega_{pe}$, $v_e/c=0.13$, $m_i/m_e=100$, $u_1^{\rm in}/c=u_2^{\rm in}/c=0.04$, and $(\omega_1-\omega_2)/(k_1+k_2)=3.5v_e=0.45c$. (a) Higher-frequency pump-wave energy density versus time. (b) Lower-frequency pump-wave energy density components for left and right-going vacuum transverse waves versus time. (c) Longitudinal field energy density spectrum versus wave number at $\omega_{pe}t=100$ showing the beat-wave peak. (d) The electron velocity distribution versus velocity parallel to the beat-wave phase velocity at $\omega_{pe}t=1000$ showing tail formation. The trapping width was as large as v_e. 120% of the beat-wave momentum was deposited in the electrons and -20% in the ions.

background magnetic field.

Additional simulations by Cummings and Cohen (1989) including a background axial magnetic field demonstrated the requirement that the two transverse pump waves have the same polarization for good coupling. For propagation parallel to the background magnetic field, the normal modes are right and left circularly polarized. Simulations of a pair of linearly polarized pump waves showed that they decompose into a pair of right circularly polarized pump waves and a second pair of left circularly polarized pump waves. Each pair of waves had approximately one-half of the power of the original pair of waves, which reduced the rate of action transfer by one-half as predicted by theory (Cohen, Cohen, Logan *et al.*, 1988). Simulations with one pair of identically polarized, left or right circularly polarized pump waves showed no reduction in the rate of action transfer from the rate observed for two identically polarized pump waves with no background magnetic field.

F. Parametric instabilities

Parametric instabilities associated with FEL heating and current drive were reviewed in Sec. IV. Here we give two simulation examples of parametric instabilities that could occur in intense electron cyclotron heating. In both cases, the ZOHAR self-consistent electromagnetic particle code was used to simulate the interaction of an ordinary mode propagating perpendicular to a background magnetic field and normally incident on a plasma slab. Self-consistent particle simulation is well suited to the simulation of laser-plasma interactions and parametric instabilities where kinetic detail and a model that is close to first principles are desirable. However, the simulations accommodate only limited ranges of time and space scales, and typically use artificial parameters to compress the disparate time and space scales. Nevertheless, considerable insight and valuable theoretical understanding have been gained with the use of simulations.

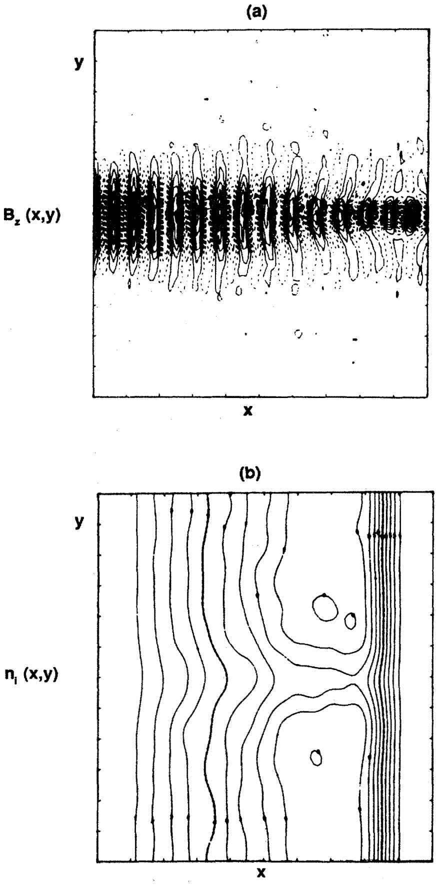

FIG. 28. ZOHAR particle simulation of ponderomotive self-focusing for a perpendicularly incident ordinary mode. The background magnetic field was oriented in the y direction. (a) Contours of the wave magnetic field in the x,y plane at $\omega_0 t = 300$ showing focusing of the wave. (b) Contours of the ion density in the x,y plane showing ducting of the plasma accompanying the self-focusing.

In the first example of parametric instability, Fig. 28 shows strong evidence of self-focusing in two-dimensional contour plots of the magnetic field of the wave and the ion density. The electromagnetic beam constricts and digs a channel through the plasma as it propagates across a background magnetic field. A series of two-dimensional simulations were performed by us with mobile ions having a mass ratio $m_i/m_e = 10$ and for various values of the incident ordinary mode amplitude. There was significant focusing of the beam in Fig. 28 for $v_0/c = 0.4$, $T_i = T_e = 0.09 m_e c^2$, $\omega_0 = |e/m_e| = c = 1$, a beam half-width $\omega_0 a/c \approx 15$, and a flat-top density profile with $\omega_{pe}^2/\omega_0^2 \leq 0.5$. The cyclotron frequency in the nonuniform background magnetic field varied linearly across the simulation domain, $0.85 \leq \Omega_e(x)/\omega_0 \leq 1.35$. With these parameters, the inequalities (4.6) and (4.7) were satisfied, i.e., ponderomotive self-focusing dominates relativistic self-focusing and modulational instability. Inequality (4.8) is not satisfied, from which we infer that steady-state, self-trapped filaments are not expected according to the nonlinear analysis of Max (1976). However, some convective focusing is certainly evident in Fig. 28.

Porkolab and Cohen (1988) calculated the maximum linear growth rate for convective filamentation of an ordinary mode:

$$k_x = \frac{1}{8} \frac{\omega_0}{v_g} \frac{\omega_{pe}^2}{\omega_0^2} \frac{v_0^2}{v_e^2} \left[1 + \frac{T_i}{Z_i T_e} \right]^{-1} . \tag{5.1}$$

Equation (5.1) suggests that the fastest growing linear perturbation of a wide beam would grow by approximately two e-foldings in traversing the simulation plasma for the parameters of Fig. 28. With wave amplitudes corresponding to $v_0/c \leq 0.2$, there would be less than one-half e-folding, which agrees with the self-focusing that was observed in a simulation with $v_0/c = 0.2$ and the substantial self-focusing evident with $v_0/c = 0.4$. It is noteworthy that these estimates based on a linear theory of self-focusing agree qualitatively well with the simulations, because the analytical theory omits both the finite beam width of the laser and the finite amplitude of the plasma perturbation.

The second example of parametric instability is stimulated Brillouin scattering of an ordinary mode that is backscattered by a lower hybrid wave. Stimulated Brillouin backscatter was identified in Sec. IV.A as potentially one of the most dangerous parametric instabilties for intense, pulsed ECH, because it can result in the reflection of a large amount of the laser energy before it reaches the absorption layer in the plasma. The following analytical arguments and results from one-dimensional particle simulations illustrate some of the physics of Brillouin backscatter in a magnetized plasma and serve as a useful paradigm (Cohen, Cohen, Nevin *et al.*, 1988).

Consider the backscatter of a perpendicularly incident ordinary wave ($\mathbf{k}\cdot\mathbf{B}_0=0$) by a perpendicularly propagating lower hybrid wave. The calculation of the frequency and growth rate has been given in (B. Cohen, 1987a). The local growth rate is given by

$$\gamma_0=\frac{k_0 v_0}{2}\frac{\omega_{pe}^2}{\Omega_e^2}\left[\frac{\omega_{lh}}{\omega_0}\right]^{1/2}\left[1+\frac{\omega_{pe}^2}{\Omega_e^2}\right]^{-1/2} , \qquad (5.2)$$

where $\omega_{lh}=\omega_{pi}/(1+\omega_{pe}^2/\Omega_e^2)^{1/2}$. The steady-state coupled-mode equations for the pump wave and the backscattered radiation are readily deduced from Maxwell's equations and a simple fluid theory (Kruer, 1980),

$$\frac{\partial}{\partial x}a_0=-\alpha\frac{\delta n_e}{n_0}a_1 , \quad \frac{\partial}{\partial x}a_1=-\alpha\frac{\delta n_e}{n_0}a_0 , \qquad (5.3)$$

where δn_e is the perturbed electron density in the ion wave, $a_{0,1}$ are the vector potentials for negligibly damped transverse modes, $\alpha\equiv(\pi/2)(\omega_{pe}^2/\omega_0^2)\lambda_0^{-1}(1-\omega_{pe}^2/\omega_0^2)^{-1/2}$, and λ_0 is the vacuum wavelength of the incident transverse wave. For backscattering over a uniform plasma of length L, Eq. (5.3) can be integrated for constant $\alpha\delta n_e/n_0$ to obtain a reflection coefficient for Brillouin backscatter

$$R_b=|a_1(0)/a_0(0)|^2=\tanh^2(\alpha L\delta n_e/n_0) . \qquad (5.4)$$

The reflection coefficient at saturation is then determined by the amplitude of the ion wave.

On a relatively short time scale determined by the growth rate of the instability and the initial fluctuation levels, the ion wave can grow to large amplitude and trap ions before significant heating or deformation of the equilibrium density profile can occur. Because of the strong background magnetic field across which plasma must be transported in order to steepen the density profile, profile steepening as a possible saturation mechanism is inhibited. An unmagnetized analytical description of the ions suffices to describe their trapping in the limit that the lower hybrid frequency and the growth rate greatly exceed the ion cyclotron frequency. From a simple waterbag model (Dawson *et al.*, 1973), an approximate trapping criterion can be derived:

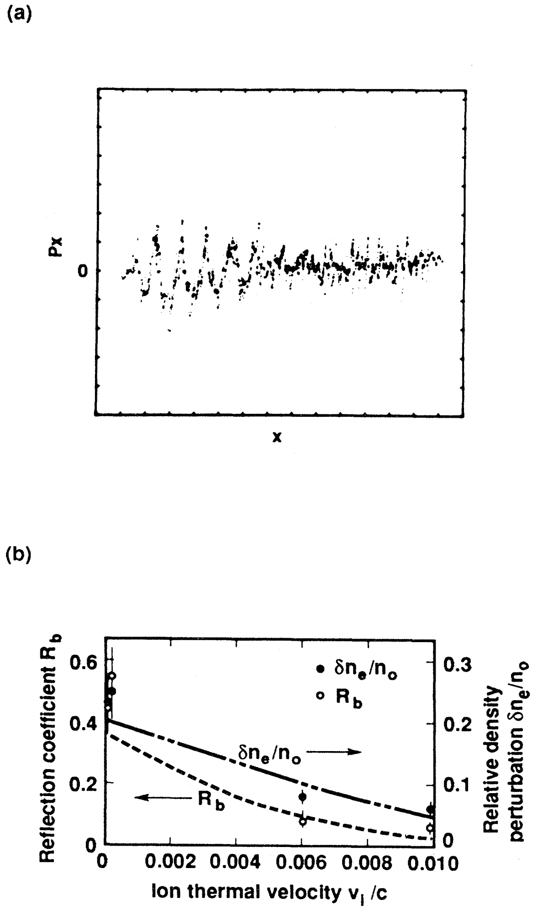

FIG. 29. One-dimensional particle simulation results for stimulated Brillouin backscatter by a lower-hybrid wave (Cohen, Cohen, Nevins, *et al.*, 1988). (a) Ion phase space, momentum p_x versus x, showing the onset of ion trapping, which saturates the backscatter. (b) The perturbed electron density $\delta n_e/n_0$ and reflection coefficient for Brillouin backscatter $R_b\equiv|a_1(0)/a_0(0)|^2$ at saturation as functions of the initial ion thermal velocity.

$$\frac{e\delta\phi}{m_i}\geq\frac{1}{2}\left[\frac{\omega_{lh}}{k}-\sqrt{3}v_i\right]^2$$

$$\rightarrow\frac{\delta n_e}{n_0}\geq\frac{1}{2}\frac{m_i}{m_e}\frac{\omega_{lh}^2}{\Omega_e^2}\left[1-\sqrt{3}\frac{kv_i}{\omega_{lh}}\right]^2 , \qquad (5.5)$$

where $\delta\phi$ is the electrostatic potential perturbation, $k=2k_0$, $v_i=(T_i/m_i)^{1/2}$, and the electron response is assumed to be linear. Use of Eq. (5.5) for $\delta n_e/n_0$ in Eq. (5.4) relates the reflection coefficient to the ion temperature. Figure 29(a) shows significant ion trapping in a snapshot of the ion phase space from a ZOHAR particle simulation, while in Fig. 29(b) we plot simulation results for the relative density perturbation and reflection coefficient at saturation compared to the theoretical estimates of Eqs. (5.4) and (5.5) as a function of the ion thermal velocity. Fairly good agreement with theory was obtained, and the strong effect that increasing the ion temperature on reducing the reflection coefficient was evident. The analysis for backscatter by electrostatic ion cyclotron waves is generally similar, but the ions are magnetized, which alters the trapping criterion (Cohen *et al.*, 1982).

Two-dimensional ZOHAR simulations of stimulated Brillouin scattering by lower hybrid waves showed a reduced level of backscattering as compared to the results of the one-dimensional simulations. The two-dimensional simulations were more (numerically) collisional, which decreased the growth rates and increased the thresholds; and competition with other parametric instabilities that led to plasma heating was observed. A likely candidate for a competing absorptive parametric instability was an oscillating two-stream instability that nonlinearly converts the incident O mode into upper hybrid or electron Bernstein sidebands and has growth rates comparable to Brillouin backscatter growth rates for the simulation parameters (Tripathi *et al.*, 1984).

VI. EXPERIMENTAL TESTS

The first laboratory tests of some of the theoretical issues associated with intense, pulsed FEL heating and current drive will be provided by the MTX experiment at the Lawrence Livermore National Laboratory (Thomassen, 1986). In 1992, the MTX FEL using the IMP wiggler is expected to deliver peak powers of 3 GW at 140 GHz with an extraction efficiency of 25–30% (Jong *et al.*, 1989). With a roughly elliptical spot pattern whose radii are 3.6 cm laterally and 2.6 cm vertically, this corresponds to 400 kV/cm or $E_{\parallel}/B_0=0.027$ for the O mode and $B=5$ T. This intensity will put the expected absorption in the strongly nonlinear regime ($p_1\sim 4$, $p_2\sim 1.3$) as modified by rising-bucket effects. The field intensity is well below the threshold for stochasticity. The divergence of the ray bundle introduces a spread in $k_{\parallel}$ and should enhance the absorption. The predicted opacity is $\tau=0.7$ with a diverging ray bundle, and $\tau\leq 0.2$ without rising-bucket effects. The microwave power transmitted and reflected by the plasma will be detected by calorimeters and microwave horns, and the local electron energy increase measured, from which the absorption will be inferred. Plasma heating and current drive will be negligible for single-pulse injection. Later in the experimental plan, fifty pulses will be injected at a 5 kHz rate. This will give sufficient energy to measurably heat the plasma. Because the FEL pulses will be short (≤ 50 ns), stimulated Brillouin backscatter is not expected to be severe. Some self-focusing may occur, which will be difficult to detect unless the self-focusing is extreme. By adjusting the toroidal magnetic field strength, the cyclotron resonance can be moved outside the plasma, which could be used to separate resonant absorption and self-focusing effects.

A second experimental facility at Livermore is being used to study aspects of beat-wave current drive. The Davis Diverted Tokamak (DDT) is a research tokamak operated jointly by the University of California at Davis and the Lawrence Livermore National Laboratory under the auspices of the Plasma Physics Research Institute. Two microwave sources with 140 kW peak power, frequencies in the range 8.8–9.5 GHz, and pulse lengths of 2.5 μs are launched in opposition to one another along a chord of the torus (Rogers *et al.*, 1989, 1990). The plasma density is varied in the range 1.2×10^8 to 2×10^9 cm^{-3} to test the resonant coupling of the microwaves to a Langmuir wave. Both a dipole antenna and a microwave scattering diagnostic will be used to measure the amplitude of electrostatic waves. The tokamak is operated without Ohmic current to make it easier to detect current drive. With the relatively low microwave powers in DDT, the relative action transfer and current drive expected are small. However, resonant excitation of a beat wave has been observed (Rogers *et al.*, 1990).

An important limitation on studying current drive in the DDT experiment is that the L/R time (~ 100 μs) is much longer than the 2.5 μs pulse length of the microwaves. Therefore, the beat-wave excitation will lead to a back-emf to cancel most of the current drive. The back-emf can be measured as a loop voltage. A distortion of the electron distribution function can be measured with an energy analyzer. In order to better drive current with a single microwave pulse, microwave sources will be installed with 1 ms pulse lengths that much exceed the L/R time. Although the low microwave powers in DDT restrict the expected beat-wave current drive to have a low efficiency, experiments in DDT should be able to quantitatively test the resonant excitation of beat waves and electron acceleration in a bounded, magnetized plasma. While there have been many experiments preceding DDT that have studied the resonant excitation of beat waves, beat-wave acceleration, and optical mixing (see the review by Stefan, Cohen, and Joshi, 1989, and references therein), the experimental observation of beat-wave current drive in the toroidal geometry of DDT will be significant for future magnetic fusion applications.

VII. CONCLUSIONS

This paper has reviewed recent theoretical analyses addressing the interaction of intense, pulsed, coherent electron cyclotron waves with plasmas. There are several reasons for the current interest in this subject. There has been dramatic progress in the development of induction-linac-driven free-electron lasers. The application of these high-power FEL's to microwave heating and current drive in the electron cyclotron range of frequencies has a number of technical advantages and will be tested in the MTX at the Lawrence Livermore National Laboratory. The associated laser-plasma interactions are also potentially relevant to ionospheric modification by radio-frequency waves, high-energy electron acceleration, and the propagation of intense, pulsed electromagnetic waves in astrophysical magnetized plasmas.

The physics of the interaction of an intense laser with a magnetized plasma is highly nonlinear, and there are many novel phenomena. Relativistic effects play an important role in the resonant wave-particle interactions. The coherent, intense, pulsed nature of the FEL has made possible considerable innovation and the invention of several new concepts utilizing FEL's for plasma heating and current drive that depend on stochasticity, rising buckets, and beat-wave coupling. Out of these new concepts may come efficient mechanisms for plasma heating, sustaining the toroidal current in a steady-state tokamak, controlling current and pressure profiles in order to stabilize magnetohydrodynamic fluctuations and disruptions (Hanada *et al.*, 1991), and diagnosing conditions in a hot plasma. The pulsed nature of FEL current drive is especially well suited to the possibility of doing feedback stabilization of disruptions by modifying the current locally in the profile. The new heating and current-drive concepts have been studied by first analyzing the underlying nonlinear wave-particle interactions. The analytical calculations of the nonlinear dynamics, the implications for current drive, and the stability of the laser-plasma system have been supported with computer simulations in many cases, which have both confirmed the analyses and extended the calculations beyond the limits of the analytical theories.

The calculations reviewed here need both extension and refinement, and many new research questions have been raised. For example, a comprehensive rigorous calculation of the nonlinear opacities in the various nonlinear regimes needs to be done; calculations of the stability of the heated plasma have only just begun; many more calculations need to be done on parametric instabilities and nonlinear self-focusing; and more simulations ought to be performed. The cross-field particle transport associated with intense, pulsed ECH has not been studied. There is a direct influence of a cyclotron wave on the electron guiding-center location related to the change in the electron's energy as described in Sec. II.A. There are other cross-field transport mechanisms to be considered, e.g., classical collisional transport and anomalous transport due to electric field fluctuations. We expect that the classical cross-field transport of the heated electrons in the presence of collisions will decrease as the electrons heat, because the square of the step size for the diffusion process scales with the square of the Larmor radius, viz., proportional to the energy $\varepsilon_\perp$, while the collision frequency decreases as $\varepsilon^{-3/2}$. However, if there is an increase in wave turbulence as a consequence of either parametric instabilities in the presence of the FEL or microinstability of the heated electron velocity distribution, then an increase in anomalous cross-field transport is likely.

Experimental data from high-power FEL heating and current-drive experiments is needed to give guidance and direction to further theoretical modeling and analysis. The MTX experiment should yield such data in the near future. The DDT experiment is expected to provide data testing some of the principles of beat-wave current drive.

The theoretical research completed to date on FEL heating and current drive indicates that the FEL technology being tested in MTX makes possible new and novel opportunities to improve the heating, confinement and current drive in fusion plasmas. We have reviewed calculations indicating that the opacities for intense, pulsed ECH mechanisms can much exceed the quasilinear opacity for ECH, and the corresponding current-drive efficiencies are attractive according to current standards. Thus, the application of FEL's to tokamak heating and current drive may lead eventually to improved prospects for controlled fusion. The theoretical research in this area has already led to a deeper understanding of the interaction of intense electromagnetic waves in a magnetized plasma.

ACKNOWLEDGMENTS

We are grateful to our many colleagues in the Magnetic Fusion Energy Program at the Lawrence Livermore National Laboratory for their help and encouragement in the research reviewed here. We are particularly grateful to G. R. Smith and Y. Matsuda for their research contributions and collaborative assistance. We also thank A. B. Langdon, B. F. Lasinski, J. C. Cummings, M. Porkolab, and A. L. Throop for their help and support. We are also pleased to acknowledge the interest and encouragement of K. I. Thomassen, B. G. Logan, and E. B. Hooper. This work was performed under the auspices of the U.S. Department of Energy by the Lawrence Livermore National Laboratory under Contract No. W-7405-Eng-48.

REFERENCES

Akimoto, K., and H. Karimabadi, 1989, Phys. Fluids B **1**, 2530.

Amin, M. R., and R. A. Cairns, 1990, Nucl. Fusion **30**, 327.

Antonsen, T. M., and B. Hui, 1984, IEEE Trans. Plasma Sci. **PS-12**, 118.

Ashour-Abdalla, M., and C. F. Kennel, 1978, J. Geophys. Res. **83**, 1531.

Batchelor, D. B., R. C. Goldfinger, and H. Weitzner, 1984, Phys. Fluids **27**, 1153.

Bernstein, I. B., and D. C. Baxter, 1981, Phys. Fluids **24**, 108.

Bethe, H. A., and M. E. Rose, 1937, Phys. Rev. **52**, 1254.

Birdsall, C. K., and A. B. Langdon, 1985, *Plasma Physics Via Computer Simulation* (McGraw-Hill, New York).

Bolis, F. S., and O. L. Spyrou, 1986, J. Plasma Phys. **12**, 124.

Bornatici, M. R., R. Cano, O. DeBarbieri, and F. Englemann, 1983, Nucl. Fusion **23**, 1153.

Budden, K. G., 1961, *Radio Waves in the Ionosphere* (Cambridge University Press, Cambridge, England).

Cardinali, A., M. Lontano, and A. M. Sergeev, 1988, in *15th European Conference on Controlled Fusion*, Dubrovnik, Yugoslavia, Vol. 12B, Part III, edited by S. Pešic and J. Jacquinot

(European Physical Society, Geneva), p. 976.

Chan, V. S., S. C. Chiu, J. Y. Hsu, and S. K. Wong, 1982, Nucl. Fusion **22**, 787.

Chen, F. F., 1974, *Introduction to Plasma Physics* (Plenum, New York).

Chirikov, B. V., 1979, Phys. Rep. **52**, 263.

Cohen, B. I., 1984, Comments Plasma Phys. Controlled Fusion **8**, 197.

Cohen, B. I., 1987a, Phys. Fluids **30**, 2676.

Cohen, B. I., 1987b, in *Proceedings of the U.S.-Japan Workshop on Plasma Modeling with MHD and Particle Simulation*, Napa, California, edited by C. K. Birdsall and T. Kamimura (University of California, Berkeley), p. 8.

Cohen, B. I., and R. H. Cohen, 1988a, Phys. Fluids **31**, 3444.

Cohen, B. I. , and R. H. Cohen, 1988b, in *Proceedings of the 1988 International Sherwood Theory Conference*, Gatlinburg, Tenn., edited by C. O. Beasley (Oak Ridge National Laboratory, Oak Ridge), p. 3C11.

Cohen, B. I., and R. H. Cohen, 1990, Phys. Fluis B **2**, 682.

Cohen, B. I. , R. H. Cohen, B. G. Logan, W. M. Nevins, G. R. Smith, A. V. Kluge, and A. H. Kritz, 1988, Nucl. Fusion **28**, 1519.

Cohen, B. I., R. H. Cohen, W. M. Nevins, T. D. Rognlien, P. T. Bonoli, and M. Porkolab, 1988, in *Theory of Fusion Plasmas*, International School of Plasma Physics, Chexbres, Switzerland), edited by J. Vaclavik, F. Troyon, and E. Sindoni (Editrice Compositori, Bologna), p. 597.

Cohen, B. I. , R. H. Cohen, and T. D. Rognlien, 1983, Phys. Fluids **26**, 808.

Cohen, B. I., A. N. Kaufman, and K. M. Watson, 1972, Phys. Rev. Lett. **29**, 581.

Cohen, B. I., B. F. Lasinski, A. B. Langdon, and J. C. Cummings, 1991, Phys. Fluids B **3**, 766.

Cohen, B. I., N. Maron, and G. R. Smith, 1982, Phys. Fluids **25**, 821.

Cohen, B. I., M. A. Mostrom, D. R. Nicholson, A. N. Kaufman, C. E. Max, and A B Langdon, 1975, Phys. Fluids **18**, 470.

Cohen, B. I., and T. D. Rognlien, 1985, Phys. Fluids **28**, 2793.

Cohen, B. I., and T. D. Rognlien, 1989, in *Proceedings of the 1989 International Sherwood Theory Conference*, San Antonio, Texas, edited by D. Barnes (Science Applications International, Austin), p. 3C15.

Cohen, R. H., 1987, Phys. Fluids **30**, 2442; **31**, 421(E).

Cohen, R. H., B. I. Cohen, W. M. Nevins, T. D. Rognlien, P. T. Bonoli, and M. Porkolab, 1989, in *Nonlinear Phenomena in Vlasov Plasmas* (Editions de Physique, Orsay, France), p. 335.

Cohen, R. H., and T. D. Rognlien, 1991, Phys. Fluids B (in press).

Colson, W. B., and A. M. Sessler, 1985, Annu. Rev. Nucl. Part. Sci. **35**, 25.

Cummings, J. C., and B. I. Cohen, 1989, private communication.

Davidson, R. C., 1987, Phys. Lett. A **126**, 21.

Davidson, R. C., T. Y. Yang, and R. E. Aamodt, 1989, J. Plasma Phys. **41**, 405.

Davydovskii, V. Ya., 1962, Zh. Eksp. Teor. Fiz. **43**, 886 [Sov. Phys. JETP **16**, 629 (1963)].

Dawson, J. M., W. L. Kruer, and B. Rosen, 1973, in *Dynamics of Ionized Gases*, edited by M. Lighthill, I. Imai, and H. Sato (University of Tokyo, Tokyo), p. 47.

Denavit, J., and R. N. Sudan, 1975, Phys. Fluids **18**, 575.

D'Ippolito, D. A., and J. R. Myra, 1985, Phys. Fluids **28**, 1895.

Drake, J. F., P. K. Kaw, Y. C. Lee, G. Schmidt, C. S. Liu, and M. N. Rosenbluth, 1974, Phys. Fluids **17**, 778.

Farina, D., and R. Pozzoli, 1988, in *Theory of Fusion Plasmas*, International School of Plasma Physics, Chexbres, Switzerland, edited by J. Vaclavik, F. Troyon, and E. Sindoni (Editrice Compositori, Bologna), p. 683.

Farina, D., and R. Pozzoli, 1991, Phys. Lett. A **156**, 84; Phys. Fluids B **3**, 1570.

Fisch, N. J., 1987, Rev. Mod. Phys. **59**, 175.

Fisch, N. J., and A. H. Boozer, 1980, Phys. Rev. Lett. **45**, 720.

Hafizi, B., and R. E. Aamodt, 1987, Phys. Fluids **30**, 3059.

Hafizi, B., and R. E. Aamodt, 1988, Nucl. Fusion **28**, 927.

Hanada, K., H. Tanaka, M. Iida, S. Ide, T. Minami, M. Nakamura, T. Maekawa, Y. Terumichi, S. Tanaka, M. Yamada, J. Manickam, and R. B. White, 1990, Phys. Rev. Lett. **66**, 1974.

Harvey, R. W., M. G. McCoy, and G. D. Kerbel, 1989, Phys. Rev. Lett. **62**, 426.

Heikinnen, J. A., S. J. Karttunen, and R. R. E. Salomaa, 1988, Nucl. Fusion **28**, 1845.

Hizanidis, K., 1989, Phys. Fluids B **1**, 675.

Hizanidis, K., L. Vlahos, and C. Polymilis, 1989, Phys. Fluids B **1**, 862.

Hockney, R. W., and J. W. Eastwood, 1981, *Computer Simulation Using Particles* (McGraw-Hill, New York).

Humphries, S., 1986, *Principles of Charged Particle Acceleration* (Wiley, New York).

Jong, R. A., D. P. Atkinson, J. A. Byers, F. E. Coffield, G. A. Deis, B. Felker, S. W. Ferguson, R. A. Fontaine, D. B. Hopkins, M. Makowski, T. J. Orzechowski, A. C. Paul, E. T. Scharlemann, R. D. Schlueter, B. W. Stallard, R. D. Stever, and A. L. Throop, 1989, Nucl. Instrum. Methods Phys. Res. A **285**, 379.

Karimabadi, H., K. Akimoto, N. Omidi, and C. R. Menyuk, 1990, Phys. Fluids B **2**, 606.

Karimabadi, H., and V. Angelopoulous, 1989, Phys. Rev. Lett. **62**, 2342.

Karney, C. F. F., and N. J. Fisch, 1986, Phys. Fluids **29**, 180.

Kaw, P. K., G. Schmidt, and T. W. Wilcox, 1973, Phys. Fluids **16**, 1522.

Keefe, D., 1986, Part. Accel. **19**, 1.

Kitsenko, A. B., and I. M. Pankratov, 1984, Sov. J. Plasma Phys. **10**, 250.

Kitsenko, A. B., I. M. Pankratov, and K. N. Stepanov, 1975, Sov. Phys. Tech. Phys. **20**, 575.

Kotel'nikov, I. A., and G. V. Stupakov, 1990, Phys. Fluids B **2**, 881.

Kotel'nikov, I. A., and G. V. Stupakov, 1991, J. Plasma Phys. **45**, 19.

Kroll, N. M., P. L. Morton, and M.N. Rosenbluth, 1981, IEEE J. Quantum Electron. **QE-17**, 1436.

Kruer, W. L, 1980, Phys. Fluids **23**, 1274.

Kruer, W. L, J. M. Dawson, and R. N. Sudan, 1969, Phys. Rev. Lett. **23**, 838.

Kuo, S. P., and G. Schmidt, 1985, J. Appl. Phys. **58**, 3646.

Kupfer, K., 1991, Ph.D. thesis (Massachusetts Institute of Technology).

Langdon, A. B., and B. F. Lasinski, 1976, Methods Comput. Phys. **16**, 327.

Lau, Y. Y., and K. R. Chu, 1983, Phys. Rev. Lett. **50**, 243.

Lichtenberg, A. J., and M. A. Lieberman, 1983, *Regular and Stochastic Motion* (Springer, New York).

Limpouch, J., G. Loncar, I. G. Lebo, and V. B. Rozanov, 1988, Laser Part. Beams **6**, 2905.

Lontano, M., A. M. Sergeev, and A. Cardinali, 1989, Phys.

Fluids B **1**, 901.

Matsuda, K., 1988, Bull. Am. Phys. Soc. **33**, 2014.

Matsuda, Y., and G. R. Smith, 1990, in *Proceedings of the 1990 International Sherwood Theory Conference,* Williamsburg, Virginia, edited by E. R. Tracy (College of William and Mary, Williamsburg), p. 3C30; 1991, J. Comput. Phys. (in press).

Max, C. E., 1976, Phys. Fluids **19**, 74.

McMillan, E. M., 1945, Phys. Rev. **68**, 143.

Mendonca, J. T., 1986, in *Proceedings of the 13th European Conference on Controlled Fusion and Plasma Physics,* Schliersee, Germany, Vol. 10C, Part II, edited by G. Brifford and M. Kaufmann (European Physical Society, Geneva), p. 413.

Mendonca, J. T., and R. M. O. Galvao, 1986, J. Plasma Phys. **35**, 483.

Menyuk, C. R., A. T. Drobot, K. Papadopoulous, and H. Karimabadi, 1987, Phys. Rev. Lett. **58**, 2071.

Menyuk, C. R., A. T. Drobot, K. Papadopoulous, and H. Karimabadi, 1988, Phys. Fluids **31**, 3660.

Nevins, W. M., 1987, Nucl. Fusion **27**, 951.

Nevins, W. M., T. D. Rognlien, and B. I. Cohen, 1987, Phys. Rev. Lett. **59**, 60.

Orzechowski, T. J., B. Anderson, W. M. Fawley, D. Porsnitz, E. T. Scharlemann, S. Yarema, D. Hopkins, A. C. Paul, A. M. Sessler, and J. Wurtele, 1985, Phys. Rev. Lett. **54**, 889.

Orzechowski, T. J., B. R. Anderson, J. R. Clark, W. M. Fawley, A. C. Paul, D. Porsnitz, E. T. Scharlemann, S. M. Yarema, D. B. Hopkins, A. M. Sessler, and J. S. Wurtele, 1986, Phys. Rev. Lett. **57**, 2172.

Otani, N. F., and B. I. Cohen, 1988, Phys. Fluids **31**, 158.

Ott, E., B. Hui, and K. R. Chu, 1980, Phys. Fluids **23**, 1031.

Perkins, F. W., 1988, private communication.

Porkolab, M., 1977, Phys. Fluids **20**, 2058.

Porkolab, M., 1978, Nucl. Fusion **18**, 367.

Porkolab, M., and B. I. Cohen, 1988, Nucl. Fusion **28**, 239.

Pozzoli, R., and D. Ronzio, 1989, in *16th European Conference on Controlled Fusion and Plasma Physics,* Venice, Italy, Vol. 13B, Part III, edited by S. Segre, H. Knoepfel and E. Sindoni (European Physical Society, Geneva), p. 1159.

Roberson, C. W., and P. Sprangle, 1989, Phys. Fluids B **1**, 3.

Roberts, C. S., and S. J. Buchsbaum, 1964, Phys. Rev. A **135**, 381.

Rogers, J. H., D. Q. Hwang, G. Dimonte, and B. Cohen, 1989, Bull. Am. Phys. Soc. **34**, 2132.

Rogers, J. H., D. Q. Hwang, K. Baker, G. Dimonte, and J. C. Thomas, 1990, Bull. Am. Phys. Soc. **35**, 1931.

Rognlien, T. D., 1983a, Nucl. Fusion **23**, 163.

Rognlien, T. D., 1983b, Phys. Fluids **26**, 1545.

Rognlien, T. D., and W. M. Nevins, 1987, Bull. Am. Phys. Soc. **32**, 1747.

Ruth, R. D., 1983, IEEE Trans. Nucl. Sci. **NS-30**, 2669.

Schmidt, G., and W. Horton, 1985, Comments Plasma Phys. Controlled Fusion **9**, 85.

Similon, P. L., and A. N. Kaufman, 1984, Phys. Rev. Lett. **53**, 1061.

Smith, G. R., J. A. Byers, and L. L. LoDestro, 1980, Phys. Fluids **23**, 278.

Smith, G. R., and B. I. Cohen, 1983, Phys. Fluids **26**, 238.

Smith, G. R., R. H. Cohen, and T. K. Mau, 1987, Phys. Fluids **30**, 3633.

Spitzer, L., 1967, *Physics of Fully Ionized Gases* (Interscience, New York).

Stallard, B. W., W. C. Turner, S. L. Allen, J. A. Byers, B. Felker, M. E. Fenstermacher, S. W. Ferguson, E. G. Hooper, M. A. Makowski, K. I. Thomassen, and A. L. Throop, 1990, in *Proceedings of the 16th Symposium on Fusion Technology,* London, edited by B. E. Keen, M. Huguet, and R. Hemsworth (North Holland, Amsterdam), p. 1050.

Start, D. F., J. D. Cordey, and T. Edlington, 1983, Plasma Phys. **25**, 447.

Stefan, V., and A. Bers, 1984, Phys. Fluids **27**, 175.

Stefan, V., B. I. Cohen, and C. Joshi, 1989, Science **27**, 494.

Stefan, V., and N. A. Krall, 1985, Phys. Fluids **28**, 2937.

Stefan, V., N. A. Krall, and J. B. McBride, 1987, Phys. Fluids **30**, 3703.

Stenflo, L., 1989, Radio Sci. **24**, 559.

Stix, T. H., 1962, *The Theory of Plasma Waves* (McGraw-Hill, New York).

Sudan, R. N., 1963, Phys. Fluids **6**, 57.

Suvorov, E. V., and M. D. Tokman, 1988, Fiz. Plazmy **14**, 950 [Sov. J. Plasma Phys. **14**, 557 (1988)].

Tajima, T., 1985, Laser Part. Beams **3**, 351.

Tajima, T., and J. M. Dawson, 1979, Phys. Rev. Lett. **43**, 267.

Taylor, A. W., R. A. Cairns, and M. R. O'Brien, 1988, Plasma Phys. Contr. Fusion **30**, 1039.

Thomassen, K. I., 1986, *Free-Electron-Laser Experiments in Alcator-C* (U.S. GPO, Washington, DC).

Timofeev, A. V., 1989, Rev. Plasma Phys. **14**, 63.

Tripathi, V. K., S. T. Tsai, and C. S. Liu, 1984, Phys. Fluids **27**, 170.

Villalon, E., and W. J. Burke, 1987, Phys. Fluids **30**, 3695.

Wesson, J., 1987, *Tokamaks* (Clarendon, Oxford).

Wu, C. S., and L. C. Lee, 1979, Astrophys. J. **230**, 621.

Yoshioka, H., and T. M. Antonsen, 1986, Nucl. Fusion **26**, 839.

Yoshioka, H., T. M. Antonsen, and E. Ott, 1986, Nucl. Fusion **26**, 438.

Zaslavskii, G. M., M. Ya. Natenzon, B. A. Petrovichev, R. Z. Sagdeev, and A. A. Chernikov, 1987, Zh. Eksp. Teor. Fiz. **93**, 881 [Sov. Phys. JETP **66**, 496 (1987)].

Zvonkov, A. V., and A. V Timofeev, 1986, Fiz. Plazmy **12**, 413 [Sov. J. Plasma Phys. **12**, 238 (1986)].